

# Precision Measurement of Ground State Transitions in Pionic Hydrogen

Inaugural-Dissertation  
zur  
Erlangung des Doktorgrades  
der Mathematisch-Naturwissenschaftlichen Fakultät  
der Universität zu Köln

vorgelegt von  
Maik Hennebach  
aus Hamburg

Forschungszentrum Jülich  
2003

Berichterstatter: Prof. Dr. H. Ströher  
Prof. Dr. H. Paetz gen. Schieck

Tag der mündlichen Prüfung: 8. Mai 2003

## Zusammenfassung

In einem Präzisionsexperiment am Paul-Scherrer-Institut werden die hadronische Verschiebung  $\epsilon_{1s}$  und Verbreiterung  $\Gamma_{1s}$  des Grundzustandes in pionischem Wasserstoff ( $\pi\text{H}$ ) neu vermessen. Im Rahmen der Chiralen Störungstheorie stehen  $\epsilon_{1s}$  und  $\Gamma_{1s}$  in direktem Zusammenhang mit den  $\pi N$ -Isospinstreulängen. Darüber hinaus ist  $\Gamma_{1s}$  mit der  $\pi N$ -Kopplungskonstanten  $f_{\pi N}$  verknüpft. Das Experiment liefert eine direkte Überprüfung der Chiralen Störungstheorie, der Niederenergieformulierung der Quantenchromodynamik.

Im Experiment werden die Energien der Röntgenübergänge  $\pi\text{H}_{np \rightarrow 1s}$  zum atomaren Grundzustand bestimmt. Diese Energien liegen im Bereich von 3 keV, wohingegen die hadronischen Effekte nur wenige eV ausmachen. Von daher ist die Verwendung eines hochauflösenden Kristallspektrometers der einzig mögliche Zugang zu einer präzisen Messung dieser Größen. Die Differenz der gemessenen Linienenergie und des rein elektromagnetischen Wertes führt auf  $\epsilon_{1s}$ .  $\Gamma_{1s}$  ergibt sich aus der Linienbreite nach Entfaltung von Auflösungsfunktion und Dopplerverbreiterung.

Der Pionenstrahl am PSI wird zu einer Gaszelle innerhalb der Zyklotronfalle geleitet, wo die pionischen Atome erzeugt werden. Von dort emittierte Röntgenstrahlung wird durch einen sphärisch gekrümmten Braggkristall auf einen großflächigen positionsempfindlichen Detektor reflektiert. Der Reflektionswinkel (und somit die Energie) der Strahlung aus  $\pi\text{H}$ -Atomen wird über den Vergleich mit einer Eichlinie bekannter Energie bestimmt. Zum ersten Mal wurde der Röntgenübergang eines anderen pionischen Atomes (pionischer Sauerstoff) zur Energieeichung verwendet.

Ein grundlegender Teil der Meßstrategie ist die Untersuchung der Abregungskaskade in  $\pi\text{H}$ . Röntgenemissionen aus Molekülzuständen, die in  $\pi\text{H}$ - $\text{H}_2$ -Kollisionen gebildet werden, hätten eine verringerte Energie. Des weiteren wird die Linie durch Coulombabregung, einen Kollisionsprozess, bei dem die Abregungsenergie in kinetische Energie der Stoßpartner umgewandelt wird, dopplerverbreitert.

In der abgeschlossenen ersten Stufe des Experiments wurde die Einwirkung dieser Kollisionsprozesse auf Linienenergie und -form durch Dichtevariationen des Wasserstoffgases bestimmt. Die Messung unterschiedlicher Grundzustandsübergänge  $\pi\text{H}_{np \rightarrow 1s}$  erlaubte einen Einblick in die durch die Coulombabregung bestimmte kinetische Energieverteilung.

Es wurde keine Dichteabhängigkeit der Linienenergie beobachtet. Man erhält  $\epsilon_{1s} = (7.120 \pm 0.012)$  eV, was einer dreifachen Steigerung der Meßgenauigkeit entspricht. Der momentane Wissensstand der Coulombabregung erlaubt nur die Bestimmung einer oberen Grenze von  $\Gamma_{1s} \leq 0.850$  meV. Die Präzisierung von  $\Gamma_{1s}$  auf 1%, der endgültig angestrebten Genauigkeit, erfordert eine detaillierte Auswertung der Kaskadeneffekte und weitere Messungen an müonischem Wasserstoff.



## Abstract

In a new high precision experiment at the Paul-Scherrer-Institut (PSI), the strong-interaction shift  $\epsilon_{1s}$  and broadening  $\Gamma_{1s}$  of the ground state in pionic hydrogen ( $\pi\text{H}$ ) are remeasured. From  $\epsilon_{1s}$  and  $\Gamma_{1s}$ , the  $\pi N$  isospin scattering lengths can be derived by the methods of Chiral Perturbation Theory. Furthermore, the  $\pi N$  coupling constant  $f_{\pi N}$  is related to  $\Gamma_{1s}$ . The measurement constitutes a direct experimental test of the low-energy approach of QCD.

In the experiment the energies of X-ray transitions  $\pi\text{H}_{np \rightarrow 1s}$  into the atomic ground state are determined. Transition energies are on the order of 3 keV, whereas the hadronic effects are in the few eV range. Hence, the only possibility for a precise determination is to use a high-resolution crystal spectrometer. The difference of the measured line energy to the calculated pure QED values for the transition gives  $\epsilon_{1s}$ , while  $\Gamma_{1s}$  follows from the line width after deconvolution of the spectrometer response and Doppler broadening.

The pion beam at PSI is decelerated into a gas cell inside the cyclotron trap where pionic atoms are formed. X-rays emitted there are reflected onto a large position-sensitive detector by a spherically bent Bragg crystal. The reflection angle (and hence the energy) of the  $\pi\text{H}$  X-rays is derived from comparison with a calibration line of known energy. For the first time, an X-ray transition from another pionic atom (pionic oxygen) was used for energy calibration.

A major part of the experimental strategy is the investigation of the de-excitation cascade in  $\pi\text{H}$ . First, for X-rays emitted from molecular states formed during collisions of  $\pi\text{H}$  atoms with  $\text{H}_2$  molecules, a decrease in transition energies would be observed. Second, the line width is increased by Doppler broadening from Coulomb deexcitation, a collision process where the deexcitation energy of the pionic atom is converted into kinetic energy of the collision partners.

In the first stage of the experiment, effects on line energy and shape from these collisional cascade processes were studied through variation of the hydrogen density. The changes to the  $\pi\text{H}$  kinetic energy distribution caused by Coulomb deexcitation were investigated by measuring different  $\pi\text{H}_{np \rightarrow 1s}$  transitions.

A density dependence of the line energy was not observed. A result of  $\epsilon_{1s} = (7.120 \pm 0.012) \text{ eV}$  is derived from the data, which constitutes an accuracy improvement by a factor of three. With the current knowledge about Coulomb deexcitation, only an upper limit of  $\Gamma_{1s} \leq 0.850 \text{ meV}$  can be given for the hadronic broadening. The information gained in the experiment will contribute to an improved theoretical understanding of the  $\pi\text{H}$  cascade, which is indispensable to reach the envisaged final accuracy of 1% for  $\Gamma_{1s}$ .



For every complex situation there is  
a solution which is simple, neat and wrong.

— H. L. MENCKEN





# Contents

<b>1</b>	<b>Introduction</b>	<b>1</b>
1.1	Pionic atoms . . . . .	1
1.2	Investigation of the $\pi N$ interaction . . . . .	2
1.3	History of $\pi H$ experiments . . . . .	3
<b>2</b>	<b>Theoretical background</b>	<b>5</b>
2.1	Motivation . . . . .	5
2.2	The $\pi N$ scattering lengths . . . . .	6
2.2.1	Derivation of $a^+$ and $a^-$ from $\epsilon_{1s}$ and $\Gamma_{1s}$ in $\pi H$ . . . . .	8
2.2.2	Derivation of $a^+$ and $a^-$ from $\epsilon_{1s}$ and $\Gamma_{1s}$ in $\pi D$ . . . . .	10
2.2.3	Existing data on $a^+$ and $a^-$ from $\pi H$ and $\pi D$ . . . . .	12
<b>3</b>	<b>The atomic cascade in pionic atoms</b>	<b>14</b>
3.1	Cascade processes in pionic hydrogen . . . . .	16
3.2	Investigation of cascade effects . . . . .	20
<b>4</b>	<b>Experimental setup and data analysis</b>	<b>21</b>
4.1	Experimental approach . . . . .	21
4.1.1	Pion production at the PSI accelerator . . . . .	22
4.1.2	Cyclotron trap . . . . .	24
4.1.3	Cryogenic target . . . . .	25
4.1.4	Crystal spectrometer . . . . .	26
4.1.5	The spectrometer setup at PSI . . . . .	30
4.1.6	CCD detectors . . . . .	32
4.1.7	Event rates and spectrometer efficiency . . . . .	34
4.2	Data acquisition and processing . . . . .	35
4.2.1	Data acquisition, transfer and storage . . . . .	35
4.2.2	The data processing software CSD . . . . .	36
4.2.3	Cluster analysis . . . . .	37
4.2.4	Position corrections . . . . .	40
4.2.5	The fit routine FITOS . . . . .	42

4.3	Energy calibration . . . . .	43
<b>5</b>	<b>Experimental results</b>	<b>47</b>
5.1	Measurement overview . . . . .	48
5.1.1	Strategy . . . . .	48
5.1.2	2000 . . . . .	48
5.1.3	2001 . . . . .	49
5.1.4	2002 . . . . .	50
5.2	Results for $\epsilon_{1s}$ . . . . .	52
5.2.1	2000 . . . . .	52
5.2.2	2001 . . . . .	55
5.2.3	2002 . . . . .	60
5.2.4	Summary of results . . . . .	63
5.3	Results for $\Gamma_{1s}$ . . . . .	64
5.3.1	Response function . . . . .	65
5.3.2	Fit of the $\pi H_{np \rightarrow 1s}$ line widths . . . . .	68
5.4	Experimental rates . . . . .	70
<b>6</b>	<b>Conclusions and outlook</b>	<b>71</b>
6.1	Results . . . . .	71
6.1.1	The hadronic shift and width . . . . .	71
6.1.2	$\pi N$ scattering lengths . . . . .	72
6.2	Outlook . . . . .	73
<b>A</b>	<b>CCD alignment</b>	<b>75</b>
<b>B</b>	<b>Plan of the spectrometer wiring</b>	<b>79</b>
<b>C</b>	<b>Run file lists</b>	<b>81</b>

# Chapter 1

## Introduction

### 1.1 Pionic atoms

Pionic hydrogen is an exotic atom, a term describing atoms where a negatively charged particle is captured into the Coulomb field of the nucleus and bound into an orbital state. Examples of particles that have been investigated in exotic atoms range from baryons (antiprotons and  $\Sigma$ -hyperons) over leptons (muons) to mesons like the kaon or the pion. All of them are heavier than the electron, which increases binding energies and decreases the orbital radii of the system: in leading order, which is already given by the Bohr atom model, the reduced mass  $m_{red}$  of the system ( $m_{red} = \frac{m_{nucl} \cdot m_x}{m_{nucl} + m_x}$ , with  $m_{nucl}$  as the mass of the nucleus and  $m_x$  as the mass of the captured particle) is directly related to the binding energies  $B_n$  and Bohr radii  $r_B$ :

$$B_n = -m_{red}c^2\alpha Z^2/2n^2$$

$$r_B = hc/(2\pi m_{red}c^2)\alpha Z$$

$$r_n = n^2 \cdot r_B$$

with the Planck constant  $h$ , the vacuum speed of light  $c$ , the fine structure constant  $\alpha$ , nuclear charge  $Z$  and principal quantum number  $n$ .

Assuming a heavy nucleus, the binding energies (and thus transition energies) for exotic atoms are increased by  $m_x/m_e$  (with  $m_e$  as the electron mass), and orbital radii are decreased accordingly. Even for relatively light particles like the muon or the pion, this ratio is higher than 200 – for low  $n$  states, the exotic atom dimensions are closer to the nuclear than to the atomic scale.

For the formation of a pionic atom, the pion is decelerated to very low kinetic energies (a few tens of eV) by collisions with the electron shell of the surrounding atoms. Once slowed down, it is captured by the Coulomb field

of the nucleus, usually into a highly excited state. Various quantum cascade mechanisms deexcite the system into the atomic ground state or levels from which nuclear absorption occurs (Fig. 1.1). In general, the upper levels of this cascade are dominated by non-radiative processes like Auger emission, where the pion deexcites through the ejection of a hull electron. In the intermediate part, radiative deexcitation starts to compete with non-radiative processes, and it dominates in the low lying states. Measuring the energy of the emitted photons allows the direct investigation of pionic atom properties.

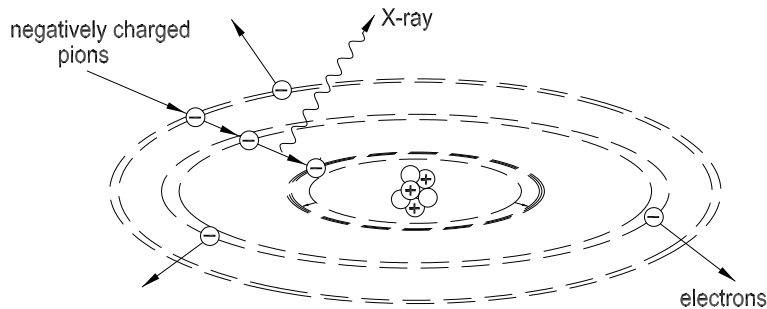


Figure 1.1: Schematical drawing of a pionic atom. The hull electrons are emitted by internal Auger effect as the pion deexcites to lower atomic states. In the final part of the quantum cascade, X-rays are emitted by radiative deexcitation.

## 1.2 Investigation of the $\pi N$ interaction

The properties of pionic atoms are not only governed by the Coulomb interaction – due to its hadronic nature, the pion will also be influenced by the strong force of the nucleons. This allows an experimental study of the low-energy pion-nucleon ( $\pi N$ ) interaction, an important testing ground of quantum chromodynamics (QCD), directly at threshold. A measurement at threshold eliminates the need for extrapolation to zero energy, which is the main difficulty when using results from low-energy scattering experiments.

Pionic hydrogen ( $\pi H$ ), consisting of a negatively charged pion and a proton, is an electromagnetically bound system. The binding energies owing to the Coulomb potential in this two-body system can be calculated very precisely by QED, which allows an unobstructed view on the hadronic effects. Due to its short range, the strong interaction will only have a noticeable effect for overlapping wave functions of pion and proton, a condition that, in  $\pi H$ , is only fulfilled by the states with angular momentum quantum number  $l = 0$ , i.e. the  $s$ -states. The hadronic influence is strongest in the  $1s$  ground

state of  $\pi\text{H}$ , because the overlap of the  $ns$  pion and proton wave functions scales with  $1/n^3$  [1].

Elastic scattering of pion and proton ( $\pi^-p \rightarrow \pi^-p$ ) increases the binding energy of the ground state by about 7 eV – a rather small effect compared with the electromagnetic binding energy of 3238 eV. The strong interaction shift  $\epsilon_{1s}$  is usually defined as the difference of the measured transition energy and the pure QED energy:  $\epsilon_{1s} \equiv E_{exp.} - E_{QED}$ . A positive sign then indicates an attractive interaction.

The decay channels of the  $s$  states, charge exchange and radiative capture of the pion ( $\pi^-p \rightarrow \pi^0n$  and  $\pi^-p \rightarrow \gamma n$ ), broaden the  $1s$  ground state by about 1 eV (strong interaction broadening  $\Gamma_{1s}$ ).

The hadronic scattering lengths of elastic scattering and charge exchange are related to the experimentally accessible quantities  $\epsilon_{1s}$  and  $\Gamma_{1s}$ :  $\epsilon_{1s} \leftrightarrow a_{\pi^-p \rightarrow \pi^-p}^h$  and  $\Gamma_{1s} \leftrightarrow a_{\pi^-p \rightarrow \pi^0n}^h$ . The exact form of this relation can be calculated within the framework of Chiral Perturbation Theory (ChPT), an effective field theory approach to QCD at low energies. A comparison of the results derived from exotic atom data with predictions from theory and other experimental results constitutes a direct test of the important theoretical method of ChPT.

### 1.3 History of $\pi\text{H}$ experiments

The unique chance of exploring the  $\pi N$  interaction directly at threshold that is offered by the  $\pi\text{H}$  system was used in several experiments before the one described in this work. As early as 1970, pionic X-rays from a hydrogen target were detected at CERN [2] with a gas proportional counter situated directly at the hydrogen gas target. Except for this pioneering measurement, all later experiments share the same basic setup: After pions have been slowed down into a gas target, the energy of X-rays from  $\pi\text{H}$  atoms formed in the target is determined by a Bragg spectrometer and a position sensitive detector. The high energy resolution of a crystal spectrometer is indispensable for accurate measurements of low-energy X-rays and identifying the rather small hadronic effects.

The next step was a measurement at Los Alamos in 1983, using a crystal spectrometer consisting of several thin graphite sheets and a position-sensitive proportional counter to measure the  $\pi\text{H}_{2p \rightarrow 1s}$  transition [3]. Due to the instrumental line width of 19 eV (a crystal with better resolution would have caused a corresponding decrease in efficiency, and low event rates were the main experimental challenge then), the hadronic broadening  $\Gamma_{1s}$  could not be investigated. Vanadium X-rays were used for energy calibration, and

the experimental result for the hadronic shift was  $\epsilon_{1s} = +3.9 \pm 1.7$  eV.

In 1985, a similar experiment with the same graphite spectrometer was installed at PSI, then called Schweizerisches Institut für Nuklearforschung (SIN) [4]. The increased pion flux from the proton accelerator there, compared with the SMC (Stopped Muon Channel) at Los Alamos, led to an increase in accuracy by almost an order of magnitude and without essential changes to the experimental setup:  $\epsilon_{1s} = +4.9 \pm 0.5$  eV.

The last step in the history of  $\pi$ H experiments so far was conducted by a collaboration of Paul-Scherrer-Institut (PSI) and the Eidgenössische Technische Hochschule Zürich (ETHZ) [5]. It started in 1985 and brought several experimental improvements. Instead of a simple degrader, the cyclotron trap (see Sec. 4.1.2) was used to decelerate the pions before they enter the gas target. The increase in rate allowed use of silicon and quartz instead of graphite crystals, which increased the resolution considerably. Using the electronic argon  $K\alpha$  line for energy calibration, this experiment culminated in a value of  $\epsilon_{1s} = +7.108 \pm 0.047$  eV for the hadronic shift and  $\Gamma_{1s} = 0.868 \pm 0.078$  eV for the hadronic width. This corresponds to an accuracy of 0.7% and 9%, respectively. Apart from the gain in accuracy for  $\epsilon_{1s}$ , the result also differs noticeably from earlier experiments.

The final aim of the experiment described herein is to measure the hadronic energy shift  $\epsilon_{1s}$  and the hadronic broadening  $\Gamma_{1s}$  with an accuracy of 0.2% and 1%, respectively. This involves several steps in a long range experimental program. The first of these steps is described in this work.

To determine X-ray energies with such high accuracy (compared with the energies of the measured transitions into the  $\pi$ H ground state, the experimental precision is on the order of a few ppm), one has to use crystals with the best resolution possible for the spectrometer. This is experimentally demanding because of the low rate efficiencies inherent in crystal diffractometers. Apart from optimisation of the spectrometer itself, the high pion flux produced at the proton accelerator of the Paul-Scherrer-Institut (PSI) and use of the cyclotron trap as a particle concentrator is instrumental in overcoming this experimental challenge.

To increase the experimental accuracy of  $\Gamma_{1s}$ , it is not enough to simply increase the statistics of the measurement. In addition to the hadronic broadening, the measured line width also contains contributions from Doppler broadening caused by Coulomb deexcitation, a process of the quantum cascade which accelerates the  $\pi$ H atom. An improved understanding of cascade processes is indispensable for a precise determination of their influence on the line width.

# Chapter 2

## Theoretical background

### 2.1 Motivation

The strong force between quarks, the constituents of both pion and proton, is described by quantum chromodynamics (QCD). The strong or hadronic interaction is transmitted by massless vector bosons, the gluons. Unlike photons as the carriers of the electromagnetic interaction, gluons carry (colour) charge themselves and are therefore able to couple to each other. As a result, the elementary processes of QCD do not just consist of emission/absorption and pair creation/annihilation, but additionally of three- and four-gluon-coupling vertices. Due to this, QCD in its basic form is incomputable at low energies, even when applied to simple systems.

A lot of effort went into finding tools that make QCD an actually usable theory. At high energies, asymptotic freedom of the quarks makes computations easier – unlike the coupling constant of the electromagnetic interaction (the fine structure constant  $\alpha$ ), the hadronic coupling constant decreases with increasing energies to the point where quarks can be treated as free particles. Here, in the realm of high energy particle physics, the particle characteristics and interactions can be described very precisely through perturbative QCD.

For energies significantly below 1 GeV (e.g. for the low-energy  $\pi N$  interaction), Chiral Perturbation Theory (ChPT) was the most important development. ChPT is based on the relatively simple world of *massless* QCD, applying the quark masses as a perturbation [6]. In the case of pions, the expansion variables of the perturbation calculation are the fine structure constant  $\alpha$ , momentum  $p$  and mass difference of up and down quarks ( $m_d - m_u$ ).

The best results of this approach can be expected for systems including pions, since these are the lightest particles composed of  $u$  and  $d$  quarks. For the pion-pion-system, an experimental test of the theoretical understanding is expected from the DIRAC experiment [7], which measures the lifetime of

pionium ( $\pi^+\pi^-$ ). The  $\pi$ H experiment described herein will allow a precise test of calculations for the hadronic properties of the pion-nucleon-system ( $\pi N$ ) at threshold. These calculations are performed in the framework of Heavy Baryon ChPT (HBChPT), an expansion of ChPT that allows the description of systems involving nucleons. Beyond pionic systems, the DEAR experiment [8] at the DAΦNE accelerator facility is set up to investigate kaonic hydrogen ( $KH$ ), which is especially interesting since it involves the strange quark  $s$ , but very challenging due to the low kaon flux available.

## 2.2 The $\pi N$ scattering lengths

Of the possible elementary reactions involving pions and nucleons, only three are directly experimentally accessible: the two elastic reactions  $\pi^-p \rightarrow \pi^-p$  and  $\pi^+p \rightarrow \pi^+p$  and charge exchange  $\pi^-p \rightarrow \pi^0n$ . Other channels are difficult to investigate due to the lack of free neutron targets and  $\pi^0$  beams. At energies close enough to threshold, the hadronic amplitudes of these three reaction channels consist solely of  $s$ -wave contributions. Assuming isospin conservation, i.e. vanishing differences of the up and down quark masses, these  $s$ -wave amplitudes can be expressed through the isospin scattering lengths  $a_I$ . The total isospin  $I$  of the  $\pi N$  system is either  $1/2$  or  $3/2$ , depending on whether the isospins  $I_\pi = 1$  of the pion and  $I_N = 1/2$  of the nucleon are parallel or antiparallel to each other.

$$\begin{aligned} a_{\pi^+p \rightarrow \pi^+p} &= a_{3/2} \\ a_{\pi^-p \rightarrow \pi^-p} &= (2a_{1/2} + a_{3/2})/3 \\ a_{\pi^-p \rightarrow \pi^0n} &= -\sqrt{2}(a_{1/2} - a_{3/2})/3 \end{aligned}$$

The characteristics of all other reaction channels at threshold can be derived from any two of these three reactions, which are related to each other by the ‘‘isospin triangle’’:

$$a_{\pi^-p \rightarrow \pi^-p} - a_{\pi^+p \rightarrow \pi^+p} = -\sqrt{2}a_{\pi^-p \rightarrow \pi^0n} \quad (2.1)$$

For these reactions, isospin breaking from  $m_d - m_u$  is expected to amount to about 1% [9], so within this accuracy, the strong interaction of pions and nucleons at low energies is completely described by two reaction amplitudes or any two combinations thereof. In this work, the isoscalar (or isospin-even) and isovector (or isospin-odd)  $\pi N$  scattering lengths  $a^+$  and  $a^-$  will be used. They are related to the elastic reaction channels by

$$a^\pm = \frac{1}{2}(a_{\pi^-p \rightarrow \pi^-p} \pm a_{\pi^+p \rightarrow \pi^+p}) \quad \text{or}$$



$$a_{\pi^- p \rightarrow \pi^- p} = a^+ + a^- \quad \text{and} \quad a_{\pi^- p \rightarrow \pi^0 n} = -\sqrt{2}a^-$$

In leading order at the limit of vanishing quark masses, the isoscalar scattering length  $a^+$  disappears due to the chiral structure of the pion – this result is already obtained in current algebra [10]. Both experimental results and more involved theoretical calculations do not deviate strongly from this basic approach (Fig. 2.1) – compared with the isovector scattering length  $a^-$ , the value of  $a^+$  is very small.

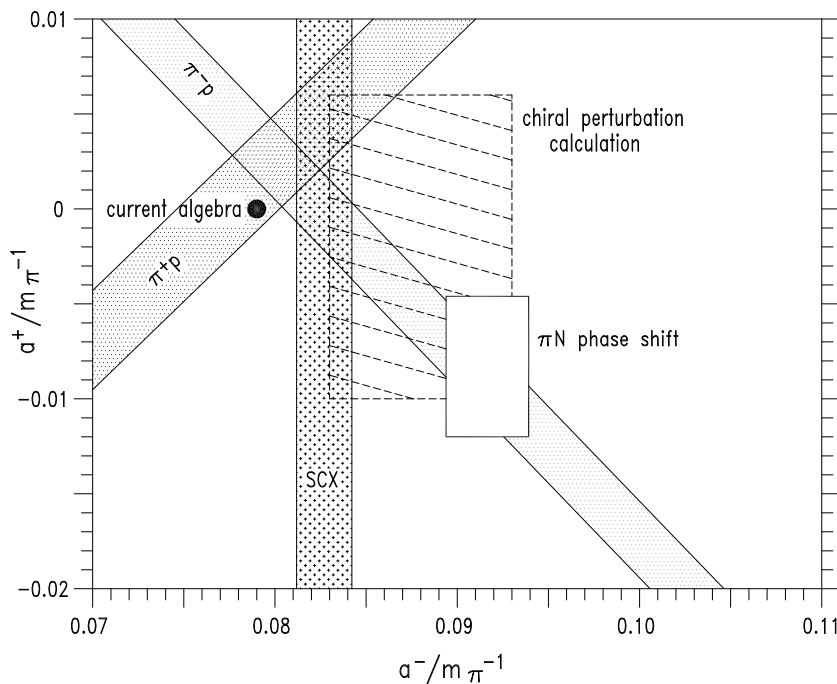


Figure 2.1: Results from theory and the analysis of low energy scattering experiments for  $a^+$  and  $a^-$ . The dot shows the leading order result of current algebra [10]. The isoscalar scattering length  $a^+$  vanishes as a consequence of the chiral structure. Diagonal and vertical bands are from analysis of low energy scattering experiments [14], but the validity of this analysis has been disputed [15]. The dashed rectangle is derived from the scattering data with a Heavy Baryon ChPT calculation to third order [16]. The small solid rectangle is based on  $\pi N$  phase shift analysis from the Karlsruhe-Helsinki group [17]; this approach to the problem is being revisited with additional information from recent data sets [18].

The  $\pi N$  coupling constant  $f_{\pi N}^2$ , which is fundamental to the understanding of the  $\pi N$  interaction, is related to the isovector scattering length  $a^-$  by the Goldberger-Miyazawa-Oehme (GMO) sum rule [11]

$$f_{\pi N}^2 = \frac{1}{2} \left( 1 - \left( \frac{m_\pi}{2m_N} \right)^2 \right) \left( \left( 1 + \frac{m_\pi}{m_N} \right) m_\pi (-a^-) - m_\pi^2 \cdot J \right),$$

with  $J$  as the difference in the total cross sections  $\sigma$  for  $\pi^+p$  and  $\pi^-p$  scattering, integrated over momentum  $q$ :

$$J = \frac{1}{4\pi^2} \int_0^\infty \frac{\sigma_{\pi^-p} - \sigma_{\pi^+p}}{\sqrt{q^2 + m_\pi^2}} dq.$$

A recent discussion on the value of the integral  $J$  is found in Ref. [12], the result is  $J = (-1.083 \pm 0.032)$  mb. At present, the largest uncertainty in the derivation of  $f_{\pi N}^2$  through the GMO sum rule stems from the isovector scattering length, so an improved accuracy for  $a^-$  would mean an improved accuracy for the determination of  $f_{\pi N}^2$  as well.

Determinations of the  $\pi N$  scattering lengths from low energy pion scattering, using ChPT calculations to 4<sup>th</sup> order [13], have reached an accuracy of a few %. An overview of this and other results from theory is given in Fig. 2.1.

### 2.2.1 Derivation of $a^+$ and $a^-$ from $\epsilon_{1s}$ and $\Gamma_{1s}$ in $\pi H$

The  $\pi N$  scattering lengths at threshold are related to the experimentally accessible quantities  $\epsilon_{1s}$  and  $\Gamma_{1s}$ , the hadronic shift and broadening of the  $\pi H$  ground state, by Deser-type formulae [1, 19]:

$$\frac{\epsilon_{1s}}{E_{1s}} = -4 \cdot \frac{1}{r_B} a_{\pi^-p \rightarrow \pi^-p}^h (1 + \delta_\epsilon) \quad (2.2)$$

$$\frac{\Gamma_{1s}}{E_{1s}} = 8 \frac{Q_0}{r_B} \left(1 + \frac{1}{P}\right) (a_{\pi^-p \rightarrow \pi^0 n}^h (1 + \delta_\Gamma))^2 \quad (2.3)$$

$E_{1s} = 3238$  eV is the electromagnetic binding energy of the ground state,  $r_B = 222.56$  fm is the Bohr radius in  $\pi H$ ,  $Q_0 = 0.142$  fm<sup>-1</sup> is the center of mass momentum of the  $\pi^0$  and  $P = 1.546 \pm 0.009$  is the Panofsky ratio [20] between the absorption processes  $\pi^-p \rightarrow \pi^0 n$  and  $\pi^-p \rightarrow \gamma n$ . In leading order, the relation between  $\epsilon_{1s}$ ,  $\Gamma_{1s}$  and the isoscalar and isovector scattering lengths  $a^+$  and  $a^-$  is very straightforward:

$$\epsilon_{1s} \propto (a^+ + a^-) \quad \text{and} \quad \Gamma_{1s} \propto 2(a^-)^2$$

However, at the level of accuracy projected for this experiment, higher order electromagnetic and isospin-breaking corrections have to be applied for a correct estimation of the  $\pi N$  scattering lengths. These corrections are encoded in the terms  $\delta_\epsilon$  and  $\delta_\Gamma$  found in the Deser-type formulae above (Eq. (2.2) and (2.3)).

**Determination of  $\delta_\epsilon$  and  $\delta_\Gamma$**  The  $\pi\text{H}$  experiment of the ETHZ-PSI collaboration [5], already introduced in Sec. 1.3, used a potential model framework [21] to determine the correction terms for  $\epsilon_{1s}$  and  $\Gamma_{1s}$ , with results of  $\delta_\epsilon = (-2.1 \pm 0.5) \cdot 10^{-2}$  and  $\delta_\Gamma = (-1.3 \pm 0.5) \cdot 10^{-2}$ . The validity of this potential model has been found to be insufficient, however.

Recent theoretical efforts based on effective field theory calculations result in  $\delta_\epsilon = (-7.2 \pm 2.9) \cdot 10^{-2}$  [22]. The large discrepancy is mainly due to the fact that the potential model does not take into account all effects from QCD and QED. To show what these effects are and how they enter into the correction factor  $\delta_\epsilon$ , a short overview of the results from ChPT calculations of  $\delta_\epsilon$  to leading [23] and next-to-leading order [22] follows.

The effective field theory calculation of the relation between the hadronic shift  $\epsilon_{1s}$  and the threshold  $\pi^-p$  scattering amplitude  $\mathcal{T}_{\pi N}$  as carried out in Ref. [23] results in

$$\epsilon_{1s} = -\frac{\alpha^3 m_{red}^3 \mathcal{T}_{\pi N}}{2\pi m_\pi} \left(1 - \frac{\alpha(\ln \alpha - 1) m_{red}^2 \mathcal{T}_{\pi N}}{2\pi m_\pi}\right) + \dots$$

with the charged pion mass  $m_\pi$ , the reduced mass of the  $\pi\text{H}$  atom  $m_{red} = \frac{m_p \cdot m_\pi}{m_p + m_\pi}$  and the fine structure constant  $\alpha$ . Corrections from distortions of the Coulomb field are encoded in the term containing  $\alpha(\ln \alpha - 1)$ . To take account of corrections from isospin breaking, the scattering amplitude  $\mathcal{T}_{\pi N}$  has to be investigated more thoroughly.

$\mathcal{T}_{\pi N}$  can be expressed as the isospin-symmetric part  $\mathcal{T}_{\pi N}^0 = a_{\pi^-p \rightarrow \pi^-p}^h$  and the isospin-breaking corrections  $\delta\mathcal{T}$ , which can again be determined by a chiral expansion:  $\mathcal{T}_{\pi N} = \mathcal{T}_{\pi N}^0 + \delta\mathcal{T}$ . When applied to the Deser-type relation between  $\epsilon_{1s}$  and the pure QCD scattering length  $a_{\pi^-p \rightarrow \pi^-p}^h$  (Eq. 2.2), the complete expression for  $\delta_\epsilon$  is:

$$\delta_\epsilon = \frac{\delta\mathcal{T}}{4\pi(1 + m_\pi/m_p)(a^+ + a^-)} - 2\alpha(\ln \alpha - 1)m_{red}(a^+ + a^-) + \delta_e^{vac}$$

Apart from  $\delta\mathcal{T}$ , the correction  $\delta_e^{vac}$  (caused by the interference of vacuum polarisation and strong interactions) has to be applied. This quantity was calculated within a non-relativistic effective Lagrangian approach in Ref. [24]: ( $\delta_e^{vac} = 0.48\%$ ). The chiral expansion  $\delta\mathcal{T} = \delta\mathcal{T}_2 + \delta\mathcal{T}_3 + \dots$  was performed to leading order ( $\delta\mathcal{T}_2$ ) in Ref. [23], giving a result of

$$\delta\mathcal{T}_2 = \frac{4(m_\pi^2 - m_{\pi^0}^2)}{F_\pi^2} c_1 - \frac{e^2}{2}(4f_1 + f_2)$$

with the physical pion decay constant  $F_\pi$ , the electron charge  $e$  and the low-energy constants (LECs)  $c_1$ ,  $f_1$  and  $f_2$ . The LECs are constants of the

efficient field theory that have to be determined from experimental data. The constant  $c_1$  is related to the dependence of the scattering amplitude on quark masses, and  $f_1$  and  $f_2$  express direct quark-photon interaction. Only two of the three LEC values are known with some accuracy:  $c_1$  was determined from  $\pi N$  phase shift data [17] and  $f_2$  is related to the electromagnetic part of the proton-neutron mass difference by  $-e^2 F^2 f_2 = (m_p - m_n)^{\text{em}}$  with  $F$  as the pion decay constant in the chiral limit. However, the LEC  $f_1$  is, at present moment, not accessible to experiment and its value can only be approximated as  $|f_1| \simeq 1.4 \text{ GeV}^{-1}$ .

Of the total contributions to the uncertainty  $\Delta\delta_\epsilon = \pm 2.9 \cdot 10^{-2}$  in the chiral perturbation calculation to next-to-leading order, an amount of  $\pm 2.8 \cdot 10^{-2}$  is solely due to the uncertainty of  $f_1$ . It remains that way when the next order ( $\delta\mathcal{T}_3$ ) is taken into account – more low-energy constants with imprecise or unknown values enter into the calculation, but they are suppressed by one power of the pion mass  $m_\pi$  compared with  $c_1$ ,  $f_1$  and  $f_2$  [22].

A similarly detailed chiral perturbation calculation for  $\delta_\Gamma$  is in the works [25], but it is already known that there is no dependence on the problematic LEC  $f_1$  in leading order, only contributions from  $c_1$  and  $f_2$  [26] –  $f_1$  is only contributing to the charge exchange channel  $\pi^- p \rightarrow \pi^0 n$  in next-to-leading order. This means that the uncertainty of the correction term  $\Delta_\Gamma$  can be expected to be far lower than for  $\delta_\epsilon$ .

## 2.2.2 Derivation of $a^+$ and $a^-$ from $\epsilon_{1s}$ and $\Gamma_{1s}$ in $\pi D$

Due to the large uncertainty of the measured value for  $\Gamma_{1s}$  from the ETHZ-PSI collaboration [5], the experimental constraints on the  $\pi N$  scattering lengths from  $\pi H$  are not very stringent. An alternative way to access  $a^+$  and  $a^-$  experimentally is available by measuring the hadronic shift of the ground state in pionic deuterium ( $\pi D$ ). Under the assumption of charge symmetry, the scattering length  $a_{\pi^- n \rightarrow \pi^- n}$  is equal to  $a_{\pi^+ p \rightarrow \pi^+ p}$ . Using Eq. (2.2),  $a^\pm$  can be derived directly from the sum and difference of the  $\pi^- p$  and  $\pi^- n$  elastic scattering lengths.

Analogical to  $\pi H$ , the relation between the measurable quantity  $\epsilon_{1s}$  and the real part of the scattering length in  $\pi D$   $\Re a_{\pi d}$  is given by a Deser-type formula [1, 19]:

$$\frac{\epsilon_{1s}}{E_{1s}} = -4 \cdot \frac{1}{r_B} \Re a_{\pi d}.$$

Correct interpretation of the experimental value in  $\pi D$  is, however, even more demanding than for  $\pi H$  due to the complications of a 3-body-problem [12, 27]: Up to second order,  $\Re a_{\pi d}$  is composed of the single-scattering term

$S$  and the double-scattering term  $D$ , which are related to  $a^+$  and  $a^-$  by

$$\Re a_{\pi d} = S + D = \frac{1 + m_\pi/M}{1 + m_\pi/M_d} a^+ + 2 \frac{(1 + m_\pi/M)^2}{1 + m_\pi/M_d} \left( \left( \frac{a^+}{2} \right)^2 - \left( \frac{a^-}{2} \right)^2 \right) < 1/r >$$

Deriving a value for  $a^+$  is challenging, because it is a very small number compared to the isovector scattering length  $a^-$  that enters the multiple-scattering correction terms.

The ETHZ-PSI collaboration has measured the  $\pi D_{3p \rightarrow 1s}$  transition [28], and a measurement of the  $\pi D_{2p \rightarrow 1s}$  transition was carried out with a direct predecessor [29] of the experimental apparatus described in this work. The results of both experiments agree within experimental errors (see Table 2.1) and the derived constraints on  $a^+$  and  $a^-$  are displayed in Fig. 2.2 along with the constraints from  $\pi H$ .

In addition to the difficulties of interpreting results from  $\pi D$ , there might be an influence on these measurements that is not accounted for – the effect from formation of molecular states (Sec. 3.1) is expected to be much stronger in  $\pi D$  than in  $\pi H$  [30] and might cause an additional energy shift.

### 2.2.3 Existing data on $a^+$ and $a^-$ from $\pi\text{H}$ and $\pi\text{D}$

Constraints on  $a^+$  and  $a^-$  from recent experiments with pionic atoms are shown in Fig. 2.2. The results for  $\epsilon_{1s}$  and  $\Gamma_{1s}$  on which these constraints are based are collected in Table 2.1.

For increased accuracy in the determination of  $a^+$  and  $a^-$  from  $\pi\text{H}$  data alone,  $\Gamma_{1s}$  is the most important angle. A precise value of the isovector scattering length  $a^-$  (which only depends on  $\Gamma_{1s}$ ), used as input for the GMO sum rule, would allow for a more precise determination of the  $\pi\text{N}$  coupling constant  $f_{\pi N}^2$ . Looking further ahead, it could also give a constraint for the low-energy constant  $f_1$  when combined with a reliable measurement and interpretation of  $\epsilon_{1s}$  in  $\pi\text{D}$ .

An unambiguous and accurate experimental result for all elastic scattering in both  $\pi\text{H}$  and  $\pi\text{D}$  and charge exchange in  $\pi\text{H}$  would even allow a test of isospin conservation through the isospin triangle (Eq. 2.1). The biggest challenge in an improved measurement of the hadronic broadening  $\Gamma_{1s}$  is to disentangle it from Doppler broadening caused by Coulomb deexcitation, a process of the  $\pi\text{H}$  cascade described in the next chapter.

In principle, the elusive  $f_1$  could be determined best from measurements of reaction channels with a significant effect from isospin breaking – one possible route, mentioned in Ref. [22], would involve a combination of the  $\pi p$  elastic scattering amplitudes to measure isospin breaking:

$$T_{\pi^+p \rightarrow \pi^+p} + T_{\pi^-p \rightarrow \pi^-p} - 2T_{\pi^0p \rightarrow \pi^0p}.$$

At present, however, there is no experimental information about the cross section  $\pi^0p \rightarrow \pi^0p$ , and it would be hard to come by. A possible access route would be neutral pion photoproduction off protons  $\gamma p \rightarrow p\pi^0$  [31].

Measurement	Reference	$\epsilon_{1s}$ [eV]	$\Gamma_{1s}$ [eV]	Density
$\pi\text{H}_{3p \rightarrow 1s}$	Schröder <i>et al.</i> [5]	$7.108 \pm 0.013 \pm 0.034$	$0.868 \pm 0.040 \pm 0.038$	15 bar
$\pi\text{D}_{3p \rightarrow 1s}$	Chatellard <i>et al.</i> [28]	$-2.430 \pm 0.050 \pm 0.050$	$1.020 \pm 0.170 \pm 0.040$	15 bar
$\pi\text{D}_{2p \rightarrow 1s}$	Hauser <i>et al.</i> [29]	$-2.469 \pm 0.035 \pm 0.042$	$1.093 \pm 0.103 \pm 0.013$	2.5 bar

Table 2.1: Results from recent experiments with  $\pi\text{H}$  and  $\pi\text{D}$ , given as *value*  $\pm \Delta_{stat} \pm \Delta_{sys}$ . Also noted is the density of the target gas (in equivalent pressure).

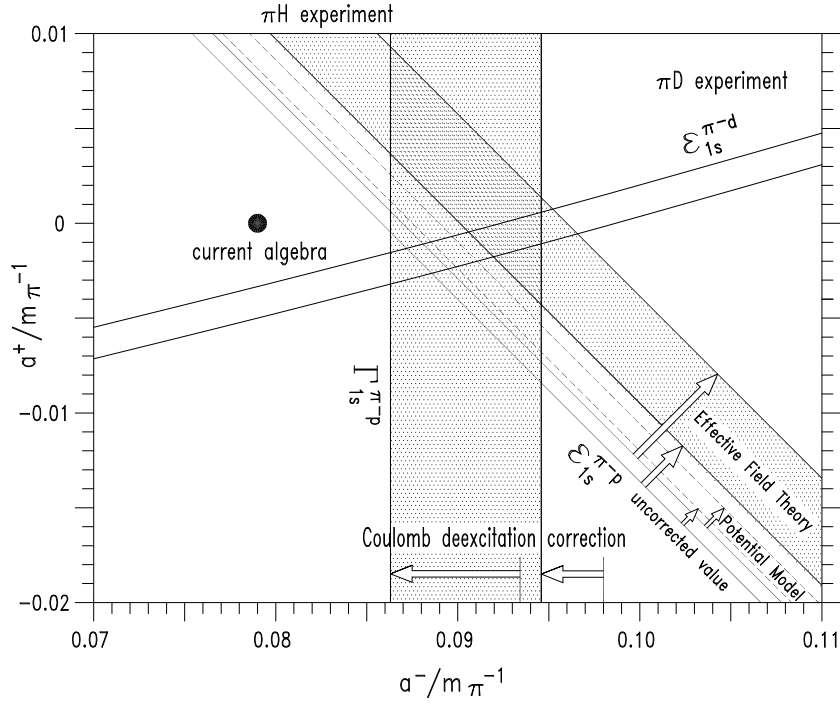


Figure 2.2: Experimental results from  $\pi\text{H}$  and  $\pi\text{D}$  for  $a^+$  and  $a^-$ , with the theoretical prediction from current algebra [10] included for orientation. The vertical band labeled  $\Gamma_{1s}$  shows the constraint on  $a^-$  from the ETHZ-PSI  $\pi\text{H}$  experiment [5], corrected for Coulomb deexcitation (see Sec. 3.1). The three diagonal bands labeled  $\epsilon_{1s}^{\pi^-p}$  show the result from Ref. [5] without the correction factor  $\delta_\epsilon$  (solid lines), with  $\delta_\epsilon$  derived from a potential model [21] (dashed lines) and from an effective field theory calculation [22] (filled band). The diagonal band labeled  $\epsilon_{1s}^{\pi^-d}$  is from the  $\pi\text{D}_{3p \rightarrow 1s}$  and  $\pi\text{D}_{2p \rightarrow 1s}$  measurements of the ETHZ-PSI collaboration [28] and the PSI measurement of the  $\pi\text{D}_{2p \rightarrow 1s}$  transition [29] corrected for 3-body effects [12].

# Chapter 3

## The atomic cascade in pionic atoms

Pions are captured into a hydrogen atom in a highly excited state, typically with a principal quantum number of  $n \sim \sqrt{\frac{m_\pi}{m_e}} = 16$  and high angular momentum quantum number  $l$ . Before the pions undergo radiative transitions into the ground state that can be observed by experiment, they will go through a number of different non-radiative processes. While these processes, called the atomic cascade, are not directly observable, their effect on the line yield and shape is very noticeable. Therefore, an understanding of the cascade is crucial to the success of the experiment. More detailed descriptions of pion capture and the atomic cascade can be found in Ref. [32] for hydrogen and Ref. [33] for hydrogen and other light atoms.

In the more general case of light pionic atoms, the most important de-excitation mechanism is the internal Auger effect, where the binding energy gained from the pion is converted into kinetic energy of an ejected electron. After the whole electron hull has been removed, radiative transitions are the only possible means of deexcitation and dominate the remainder of the cascade. This is not true for solid targets, where the electrons are promptly refilled from the surrounding electron gas.

Radiative transitions with  $\Delta l \neq \pm 1$  are strongly suppressed in light atoms, although they are important for heavy nuclei. The radiative transition width  $\Gamma_X$  is roughly proportional to the cube of the energy difference  $\Delta E$  [34]. This means that, from a given initial state, transitions with the largest  $\Delta n$  are favored and radiative lifetimes in the upper part of the cascade (with high  $n$  and high  $l$ ) are long compared with the collision rate. Radiative transitions from states with maximum  $l = n - 1$  are called circular transitions. Since they come from a hydrogen-like system consisting of the nucleus and a single pion, the energies of X-rays from these transitions can



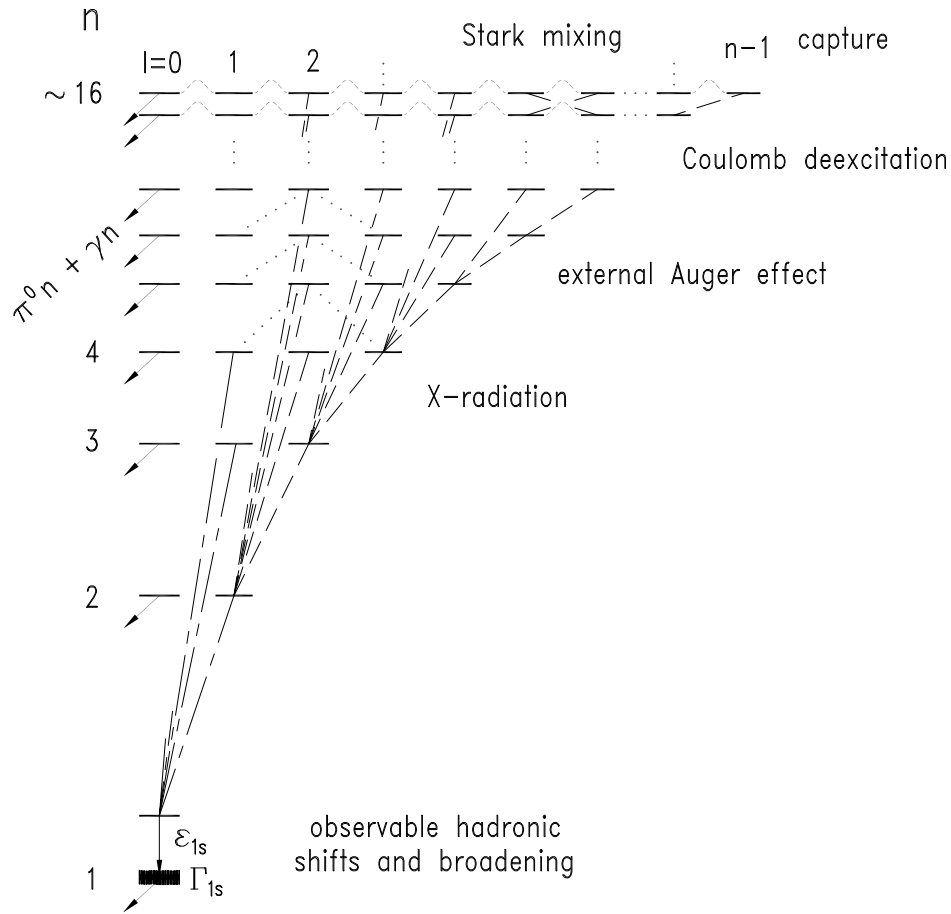


Figure 3.1: Cascade Processes in  $\pi\text{H}$  and the hadronic influence on the ground state  $1s$ . For details about the various cascade processes, see Sec. 3.1.

be calculated very precisely as long as the overlap of pion and nucleus wave functions can be neglected (i. e. for  $l \geq 2$ ).

The cascade in  $\pi\text{H}$  exhibits a very different behaviour. After the breakup of the  $\text{H}_2$  molecule and emission of the eventually remaining electron, the internal Auger effect is no longer available as a deexcitation mechanism. Of more consequence is the fact that the  $\pi\text{H}$  atom is an electronically neutral system that can easily penetrate into the Coulomb field of the surrounding  $\text{H}_2$  molecules: collisional cascade processes are far more important than for other pionic atoms. Due to this, the behaviour of the  $\pi\text{H}$  cascade is strongly dependent on density.

### 3.1 Cascade processes in pionic hydrogen

**Radiative deexcitation** Apart from nuclear reactions between pion and proton and weak decay of the pion ( $\pi^- \rightarrow \mu^- \bar{\nu}_\mu$ ), radiative deexcitation is the only non-collisional process. Regarding the latter, the pion lifetime  $\tau_{\pi^-} = 26$  ns is long compared with typical cascade times – for liquid hydrogen as an extremely fast example, experimental results give  $\tau_{exp} = 2.3 \pm 0.6$  ps [35].

**External Auger effect** This is a radiationless deexcitation of the  $\pi\text{H}$  system through the ionization of a target  $\text{H}_2$  molecule – the binding energy is mainly converted into kinetic energy of the emitted electron. Transitions with  $\Delta n = 1$  and  $\Delta l = -1$  with minimal possible energy difference are favored ( $\Gamma_{Aug.} \propto 1/\sqrt{\Delta E}$ ) [36], which means that the shape of the population distribution of the  $l$  sublevels is roughly preserved as long as only Auger transitions take place.

**Stark mixing** Since the  $\pi\text{H}$  atom is electrically neutral, it can penetrate into the Coulomb field of the surrounding  $\text{H}_2$ , which causes the substates with different angular momentum quantum number  $l$  to mix. This allows transitions  $nl_i \leftrightarrow nl_f$ , mixing the population of the various  $l$  levels. Since pions that reach  $ns$  states have a high probability of reacting with the nucleus before reaching the lower part of the cascade, this leads to a drastic reduction of X-ray yields with increasing density, the Day-Snow-Sucher effect [37].

**Nuclear reaction** With an overlap of the pion and proton wave functions (only significant for  $s$  states), the pion can undergo charge exchange  $\pi^- p \rightarrow \pi^0 n$  or radiative capture  $\pi^- p \rightarrow \gamma n$ . Apart from decreasing the yield of radiative  $K$ -transitions (absorbed pions are lost), this additional decay channel decreases the lifetime of the  $s$ -states. Accordingly, the width of X-ray transitions into these states is increased. The nuclear transition width decreases for higher  $n$  states ( $\Gamma_{ns} = \Gamma_{1s}/n^3$ ) according to the geometrical overlap [1].

**Elastic transitions** While elastic collisions do not effect the  $nl$  sublevel of the  $\pi\text{H}$ , they decelerate the collision partners and thus influence the kinetic energy distribution of  $\pi\text{H}$  atoms.

**Coulomb deexcitation** Similar to Stark transitions, but states with a different value of  $n$  are involved:  $\pi^- \text{H}_{(n)} + \text{H}_2 \rightarrow \pi^- \text{H}_{(n')} + \text{H}_2$ . Transitions

with  $\Delta n = 1$  dominate, and the width of this process grows with higher  $n$ . Since the transition energy is converted into kinetic energy of the collision partners, this process essentially determines the kinetic energy distribution of  $\pi\text{H}$  [38].

This is especially important in the final part of its cascade – although the width of Coulomb deexcitation is lower than that of Auger or radiative deexcitation at this stage, it will have a far more pronounced effect on the kinetic energy of the  $\pi\text{H}$  whenever it does occur, since there is more binding energy to convert. Peaks in the kinetic energy distribution that derive from Coulomb transitions at the end of the cascade will cause a specific Doppler broadening corresponding to the energy of the transition. In effect, the line shape of radiative transitions is folded with "Doppler-boxes" whose height depends upon the intensity of the peak in the kinetic energy distribution (Fig. 3.2).

These Doppler-boxes have been identified in time-of-flight measurements of neutrons created by the charge exchange reaction  $\pi^-p \rightarrow \pi^0n$  in  $\pi\text{H}$  [39]. Coulomb deexcitation has a similar influence on the measured width of radiative transitions into the  $\pi\text{H}$  ground state, but the kinetic energy distributions will probably be different: while charge exchange only occurs out of  $ns$  states, radiative deexcitation into the ground state occurs out of  $np$  states with a different cascade history. This is especially true for the circular  $\pi\text{H}_{2p \rightarrow 1s}$  transition. In addition, the kinetic energy distribution is changed by elastic collisions.

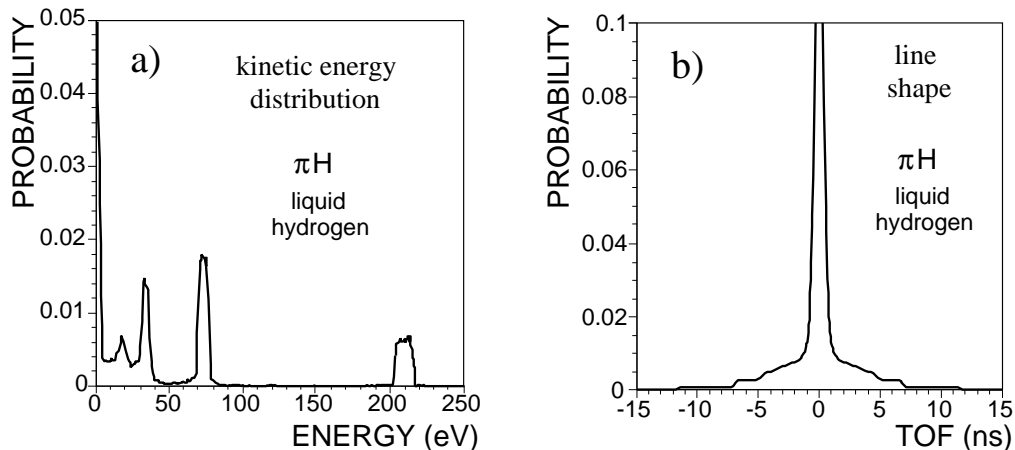


Figure 3.2: **a)** Calculated  $E_{kin}$  distribution of  $\pi\text{H}$  atoms. **b)** Calculated neutron time-of-flight spectrum for the reaction  $\pi^-p \rightarrow \pi^0n$  derived from the  $E_{kin}$  distribution in a).

**Molecular state formation** During collisions, a  $\pi\text{H}$  atom and an  $\text{H}_2$  molecule can form a hybrid molecular state in a reaction  $\pi p + \text{H}_2 \rightarrow (pp\pi)pee$ . Similar states have been observed in muon catalyzed fusion ( $\mu\text{CF}$ ) experiments [40, 41] and in a recent experiment at PSI measuring the proton radius with ground state transitions in muonic hydrogen [42].

The metastable molecular states deexcite or decay by several possible processes: they can decay through  $\pi N$  nuclear reactions, revert back to a separate  $\pi\text{H}$  and  $\text{H}_2$  or deexcite by emitting an electron (Auger decay), a photon (radiative decay) or one of the protons in a process called Coulomb decay.

Due to the different binding energies of these molecular states (which were calculated in Ref. [43]), a radiative transition from such a state would have a slightly lower energy compared with the same transition in an isolated  $\pi\text{H}$  atom.

Additionally, Coulomb decay causes an acceleration of the emitted proton and the  $\pi\text{H}$  atom, leading to Doppler broadening similar to the case of Coulomb deexcitation, but with considerably smaller kinetic energies. The lifetimes of both radiative and Coulomb decay from metastable molecular states are estimated to be higher than those of Auger decay by at least an order of magnitude, but there is no experimental data to verify this. Investigating the possible influence of this mechanism on the measured transition energies is an important part of the experiment.

As noted in Sec. 2.2.2, the radiative decay from molecular states is probably enhanced in  $\pi\text{D}$  compared with  $\pi\text{H}$  [30]. Accordingly, an influence on the measured transition energy could be more noticeable in a deuterium measurement. Within the experimental accuracy of previous measurements, no such effect was observed (see Table 2.1).

**Different levels of the cascade** The stages directly after pion capture were assumed to be dominated by the external Auger effect, but new theoretical calculations [44] indicate that Coulomb deexcitation is the main process in the upper part of the cascade (Fig. 3.1). Due to the small energy differences in this domain, this does not change the kinetic energy distribution appreciably.

For main quantum numbers  $n \sim 5 - 8$ , Auger deexcitation is the most important process. Transitions with  $\Delta l = -1$  dominate; the rarer  $\Delta l = 0$  and  $\Delta l = +1$  transitions fill up the circular transition states. In the final stages of the cascade ( $n = 1 - 5$ ), radiative transitions begin to take place along with the other processes. Circular transition rates are strengthened by radiative transitions with  $\Delta n > 1$ . Coulomb deexcitation in this stage has a marked effect on the kinetic energy distribution.

The density dependence of the  $\pi\text{H}$  X-ray yields from a recent cascade model incorporating the kinetic energy distribution of the  $\pi\text{H}$  atoms throughout the cascade [44] shows a general yield increase with decreasing density (Fig. 3.3). The reason for this is twofold; 1) a weakening of the collisional processes (Auger and Coulomb deexcitation) that compete with radiative deexcitation and 2) less pions get channeled into  $s$  states by Stark mixing, from where they can undergo nuclear reactions only.

Radiative transitions, which favor high transition energies  $\Delta E$ , increase the population of circular states. This is reflected in the development of relative yields for various  $\pi\text{H}_{np \rightarrow 1s}$  transitions ( $K\alpha$ ,  $K\beta$  and  $K\gamma$ ) at very low pressures, where radiative transitions dominate the cascade.

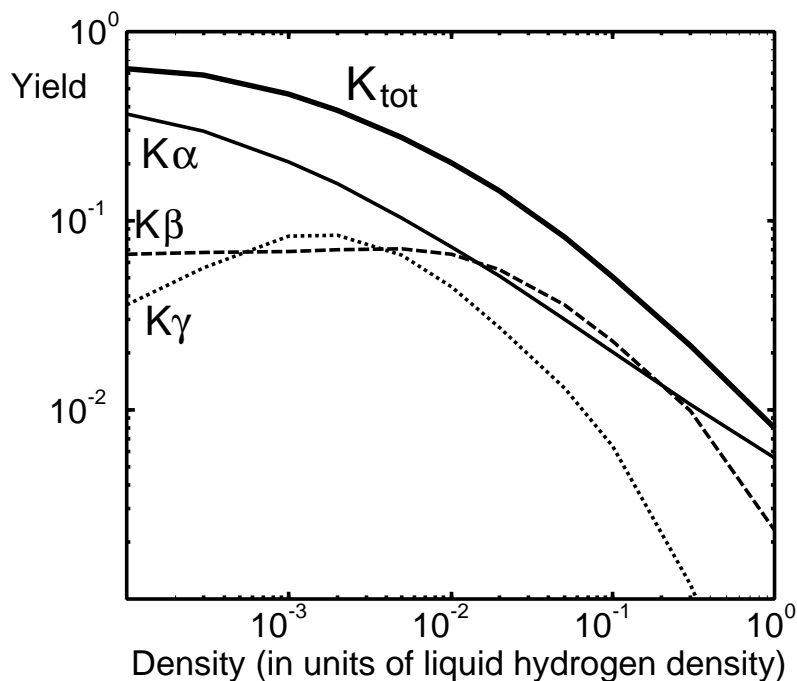


Figure 3.3: Density dependence of absolute X-ray yields in  $\pi\text{H}$  for the three K transitions from a recent cascade model calculation [44] ( $K\alpha \equiv \pi\text{H}_{2p \rightarrow 1s}$ ,  $K\beta \equiv \pi\text{H}_{3p \rightarrow 1s}$  and  $K\gamma \equiv \pi\text{H}_{4p \rightarrow 1s}$ ). Liquid hydrogen density is equivalent to a pressure of roughly 700 bar at room temperature.

## 3.2 Investigation of cascade effects

Unlike the other cascade processes whose influence is limited to the rate of radiative transitions, molecular formation and Coulomb deexcitation affect the observed properties of these transitions: the energy of the transition will be changed when the pion deexcites from a molecular state, whereas the increase in kinetic energy from Coulomb deexcitation increases the line width through Doppler broadening. Separation of these cascade influences from  $\epsilon_{1s}$  and  $\Gamma_{1s}$  is an important goal of the experiment.

Since both processes are collisional, their strength is dependent on the density of the target gas. Measurements at different target densities allow an investigation of this dependence. Neither the formation rate of molecular states, nor the ratio of radiative decay to non-radiative deexcitation processes from these states, are known well enough to ensure that they cause a detectable change of the measured transition energy. The contribution of Doppler broadening from Coulomb deexcitation to the width of the  $\pi\text{H}$  ground state, on the other hand, is very noticeable and the largest contribution to the systematical uncertainty of the experimental value for  $\Gamma_{1s}$  (Fig. 2.2).

Apart from measuring at different target pressures, another experimental handle to shed more light on Coulomb deexcitation is available by measuring different  $np \rightarrow 1s$  transitions, namely  $4p \rightarrow 1s$ ,  $3p \rightarrow 1s$  and  $2p \rightarrow 1s$  – yields of transitions from higher  $np$  states are too low in comparison. When comparing results from these three transitions, the additional high energy components in the kinetic energy distribution from the last steps of the cascade should be identifiable. For this, a good signal-to-noise ratio of the measurement is indispensable, since it is almost impossible to identify the peak tails from Doppler broadening in the presence of a high background.

# Chapter 4

## Experimental setup and data analysis

### 4.1 Experimental approach

The main components of the experimental setup (Fig. 4.1) and their tasks are as follows: pions from the beam are cyclotron trapped into a thin-walled gas target by a strong magnetic field (cyclotron trap) to form pionic atoms. X-rays from radiative transitions in these atoms are reflected onto a position-sensitive X-ray detector surface by a spherically bent crystal. The detector consists of a large array of Charge-Coupled Device (CCD) detectors. The energy of the resultant lines is tied to the line position on the detector through the Bragg reflection condition (see Eq. (4.1) in Sec. 4.1.4). To determine the energy of the  $\pi\text{H}$  transitions, pionic calibration lines with precisely known energies are used.

As has been noted in Sec. 3.2, a good signal to noise ratio is essential for a proper understanding of Coulomb deexcitation and its influence on the width of the measured lines. The two possible levers for this ratio are suppressing background and improving the event rate, both of which have to be optimised without compromising the resolution of the spectrometer. In the following descriptions of the experimental components, this optimisation process has been highlighted.

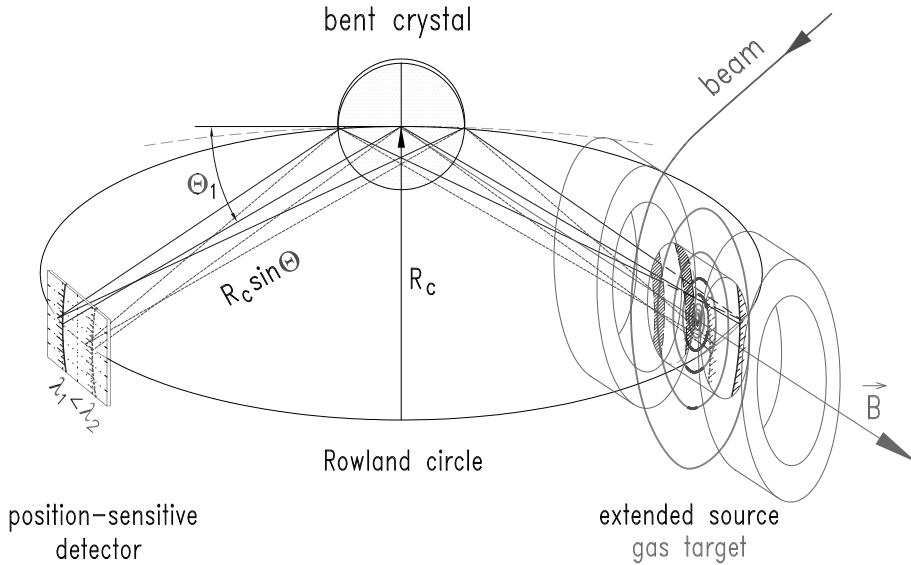


Figure 4.1: Basic measurement principle with the main components (see text).

### 4.1.1 Pion production at the PSI accelerator

The proton beam facility at PSI, shown in Fig. 4.2, is distinguished less by its energy (590 MeV) than by a proton current of up to 1.7 mA. It is thus ideally suited for the high rate production of pions, the lightest mesons. A high pion rate is essential to counteract the low efficiencies of high resolution crystal spectrometry. The secondary  $\pi$ E5 beam line, designated for high pion flux at low energies, channels pions created in the collision of the primary proton beam with the carbon production target E (length 40 mm or 60 mm) into the experimental area.

The pion momentum can be varied from 30-120 MeV/c with 10% momentum acceptance and 2% momentum resolution. The focal beam cross section is  $15 \times 20 \text{ mm}^2$  with an angular divergence of  $450 \times 120 \text{ mrad}^2$ . For the  $\pi$ H experiment, a pion momentum of 110 MeV/c is optimal for injection into the cyclotron trap (see Sec. 4.1.2). At this setting, the beam intensity is about  $4 \cdot 10^9 \pi^-/s$ . This strong pion flux causes a high neutron background in the area (roughly  $150 \text{ N}/(\text{mA s cm}^2)$ ) by the absorption of pions in matter. To prevent the secondary Compton background from reaching the CCD detector array, a concrete shielding is constructed around the spectrometer, as can be seen in the overhead view of the experimental setup (Fig. 4.3).



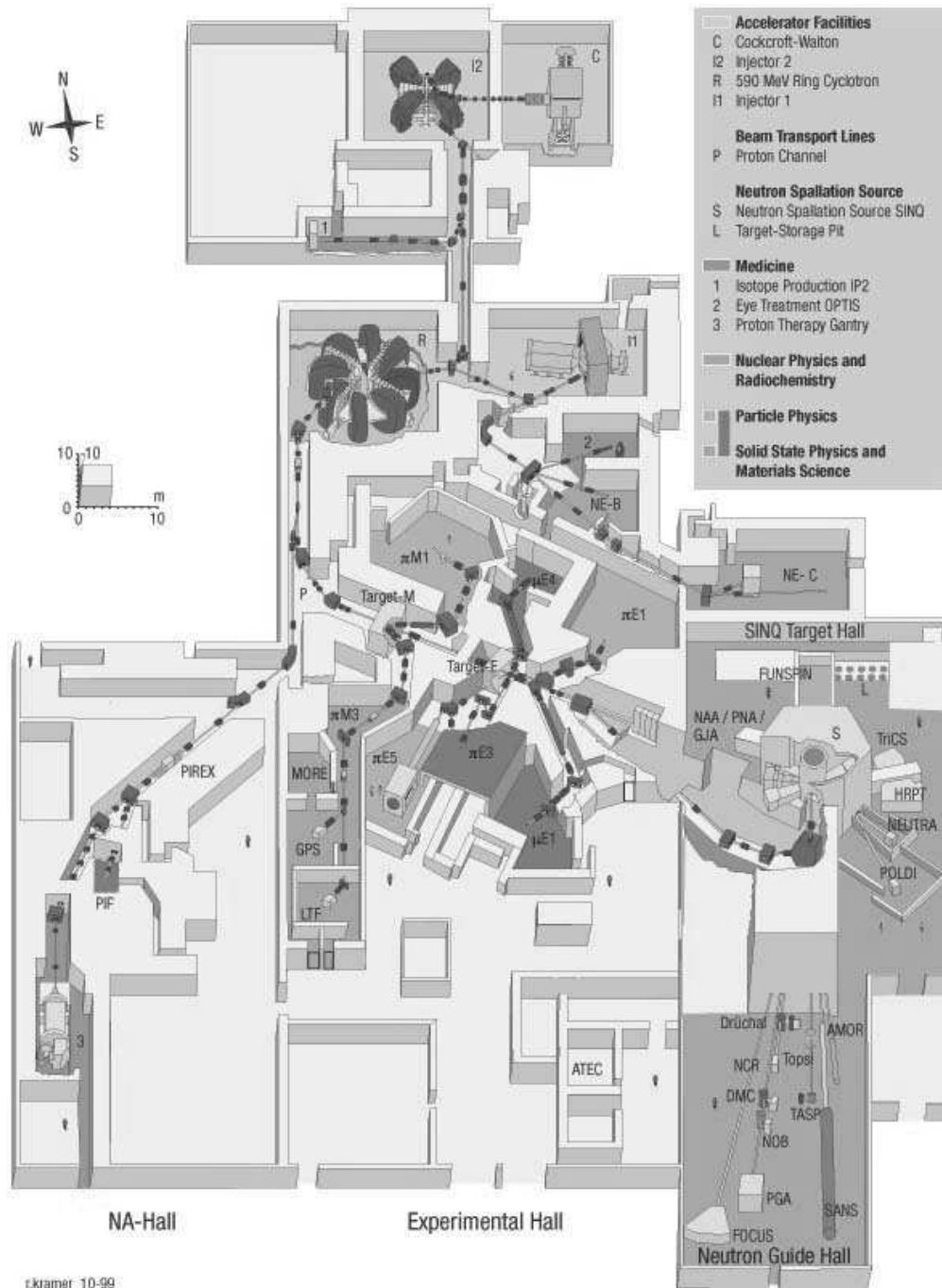


Figure 4.2: An overview of the accelerator facility at PSI. After extraction from the ring cyclotron R, the proton beam hits the production targets M and E. Pions created by the collision and muons from pion decay are focused and guided into the various experimental areas by individual beam lines. The pionic hydrogen experiment is situated in the  $\pi E5$  area at one of the five secondary beam lines coming from target E.

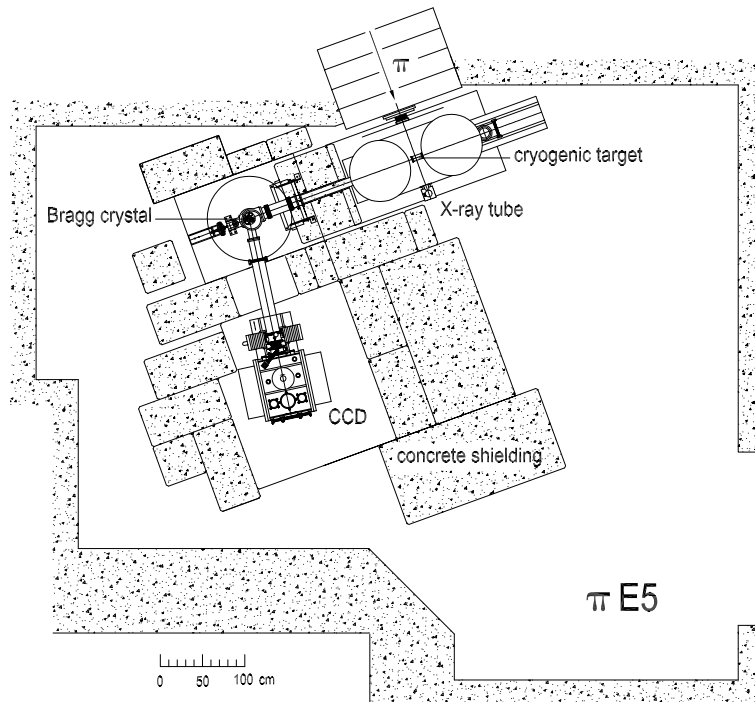


Figure 4.3: Setup of the experiment during the 2002 measurement. The pion beam (at the top of the picture) is decelerated into the cryogenic gas target inside the cyclotron trap. X-rays from pionic atoms are reflected onto the CCD detector array by the Bragg crystal.

#### 4.1.2 Cyclotron trap

For the formation of  $\pi\text{H}$  atoms, the pions from the beam have to be slowed down to kinetic energies of a few eV. Due to the short lifetime of  $\tau_{\pi^-} = 2.6 \cdot 10^{-8} \text{ s}$ , this deceleration has to be accomplished rather quickly. At the same time, a high stop density has to be achieved to allow precision spectroscopy. Both conditions are met by using the cyclotron trap[45], which is placed directly at the entrance of the pion beam line into the  $\pi\text{E}5$  areal.

A strong magnet field (created by two superconducting Helmholtz coils) perpendicular to the incoming pions forces them onto a circular path (Fig. 4.4). Several degraders on the path slow down the pions until they reach the target cell. The settings for beam line magnets and the degraders of the cyclotron trap were carefully optimised before beamtimes with X-rays from pionic neon, measured by shielded Ge detectors positioned on the axis of the magnet outside the bore hole, which have a far higher rate efficiency than a crystal spectrometer. At a gas pressure of 1 bar, about 1% of the pions from the beam are stopped in the Ne gas at optimal beam line settings.

### 4.1.3 Cryogenic target

Measurements at different densities are a central part of the experiment, as outlined in Sec. 3.2. Simply controlling the density by varying the target gas pressure is not a possibility – if the target walls were thick enough to withstand these pressures, they would completely block the low-energy X-rays from pionic atoms. Therefore, the density has to be increased by cooling down the target gas.

The cryogenic target (Fig. 4.5) is a cylinder with a diameter of 67 mm and a length of 160 mm, positioned on the axis of the magnetic field. The gas volume itself has a diameter of 59.2 mm and a length of 140.5 mm. To change the density of the target gas, it can be cooled down to a temperature of 20°K (liquefying the hydrogen). Expressed in equivalent pressure (at room temperature), this gives a range of up to  $\sim 700$  bar. Cooling is done through an external coldfinger so that the target stays at its position within the vacuum during temperature changes.

For stability tests with lines from pionic beryllium running simultaneously with the measurements, several beryllium foils are placed within the target. The axial target position can be changed without breaking the vacuum to move the beryllium foils into or out of the pion stop distribution, which has an axial extension of  $\approx 40$  mm (FWHM) and  $\approx 60$  mm (FWTM) .



Figure 4.4: Photograph of the cryogenic target within the cyclotron trap. The pion beam enters through the Kapton window in the upper left corner. The thick plastic degrader to the right of the target and the degrader foils above and to the left decelerate the pions into the target cell.

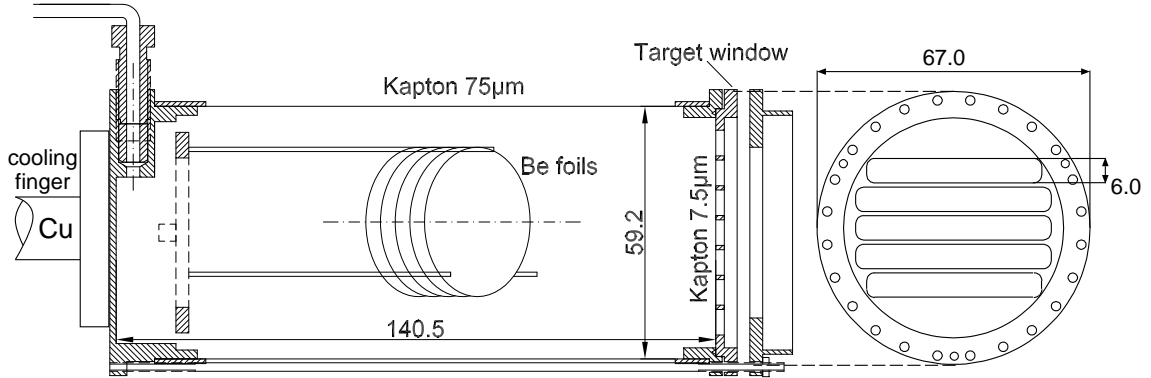


Figure 4.5: Side view of the cryogenic target cell and the target window. The beryllium foils, used for monitoring the spectrometer stability with pionic beryllium X-rays, were present only in the 2002 measurement.

The target window facing the crystal has to be thin enough to let pass enough pionic X-rays in spite of their low energy (3 keV and less). This is accomplished by reinforcing the very thin Kapton foil (7.5  $\mu\text{m}$  thickness) against pressure with a stabilising structure. The window structure consists of horizontal connections to prevent asymmetrical shading of the target stop density. For the test beamtime in 2000, a target window with a hexagonal grid structure was used. A more thorough description of the target can be found in Ref. [46].

#### 4.1.4 Crystal spectrometer

X-rays from the target region are reflected by the crystal spectrometer if they fulfill the Bragg reflection condition for constructive interference

$$n\lambda = 2d \cdot \sin \Theta_B, \quad (4.1)$$

where  $n$  is the order of reflection and  $\lambda$  is the wavelength of an incident X-ray scattering on a crystal lattice with a spacing  $d$  at the angle  $\Theta_B$  (Fig. 4.6). Inserting the photon energy  $E = hc/\lambda$  with the Planck constant  $h$  and the speed of light  $c$  gives a direct relation between the Bragg angle  $\Theta_B$  and the energy  $E$ .

For the experiment, a silicon and a quartz crystal were used due to their excellent resolution for X-rays in the few keV range ( $\Delta E/E \approx 10^{-4}$ ). Their diffraction patterns for plane crystals (rocking curve) are shown in Fig. 4.7.

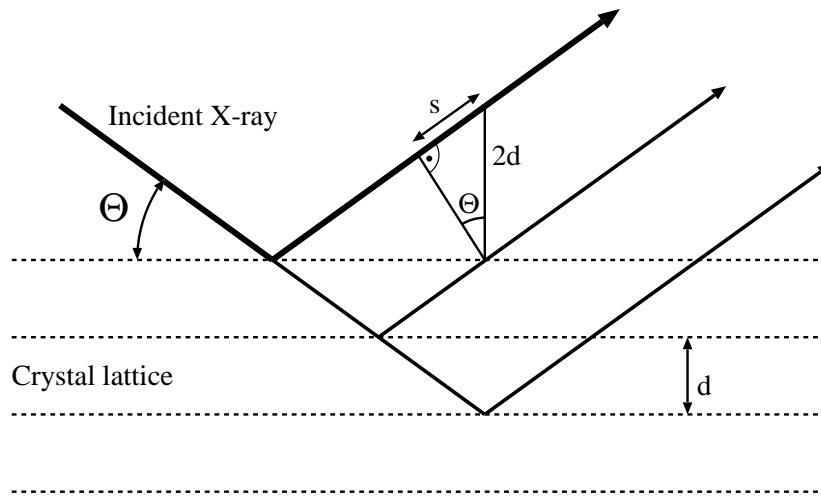


Figure 4.6: Bragg reflection with a plane crystal. Reflected X-rays interfere constructively if their optical retardation  $s = 2d \cdot \sin \Theta$  is equal to a multiple of their wave length  $\lambda$ . The primary extinction length (the distance after which the intensity of a coherently reflected beam has dropped to  $1/e$ ) for the crystals used in the experiment is  $5\text{-}6 \mu\text{m}$  at  $3 \text{ keV}$  [47].

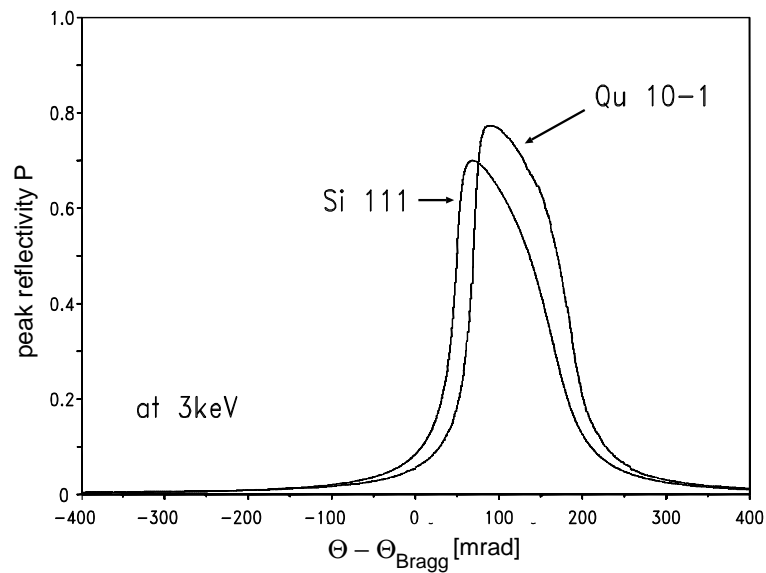


Figure 4.7: Rocking curves of the two crystals used in the experiment, derived from the XOP program written at ESRF [47]. The peak reflectivity  $P$  indicates the fraction of reflected intensity at a specific angle  $\Theta$ .

**Johann setup** The use of a horizontally bent crystal to increase the intensity of a Bragg spectrometer for an extended X-ray source is a rather old idea. Its early development was hindered for a while by a work of E. Wagner [48] that stated the impossibility of fulfilling both the Bragg condition and the normal law of reflection (emission angle = incidence angle) for a curved crystal surface. While this statement was correct, H. H. Johann discovered that in a practical application, the error incurred by this is rather small and can easily be quantified [49].

The bending radius of the crystal in a Johann spectrometer is twice the radius  $R$  of the Rowland circle, which is defined by the focusing condition  $R \cdot \sin \Theta_B$  (Fig. 4.8). Since the crystal only touches the Rowland circle in one point, X-rays reflected elsewhere on the crystal will appear to be shifted to higher energies. With  $b$  and  $R$  as horizontal width and bending radius of the crystal and  $\Theta_B$  as the Bragg angle, the maximal shift at the edge of the crystal (“Johann shift”) is  $\Delta\Theta_J = \frac{1}{8}(\frac{b}{R})^2 \cot^2 \Theta_B$ . When integrated over the whole crystal, the resultant shift of the line centroid is almost exactly  $C_{Johann} = \frac{1}{3}\Delta\Theta_J$  [50].

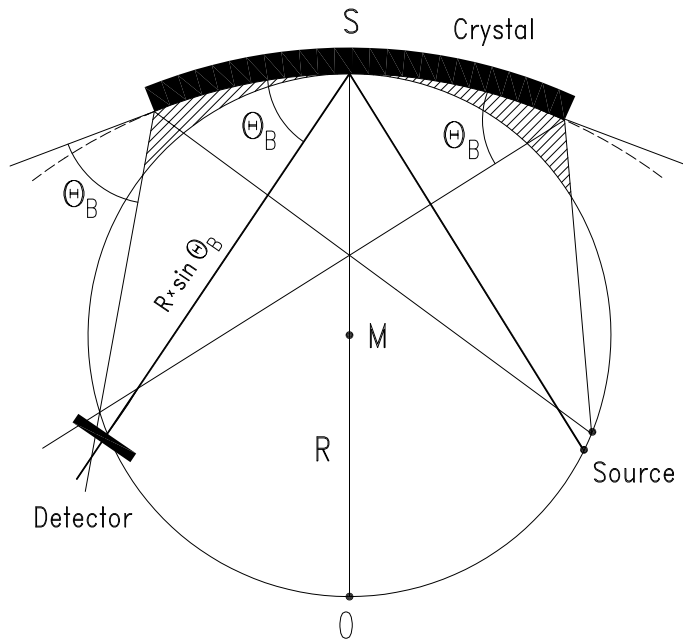


Figure 4.8: The Johann setup for Bragg spectroscopy. The crystal bending radius  $R = SO$  is the diameter of the Rowland circle (with the center at  $M$ ) on which the focusing condition  $R \cdot \sin \Theta_B$  is fulfilled.

For a symmetrical Johann setup, the positions of X-ray source and detector are interchangeable. This means that the line image on the detector is exactly mirrored within the target – only X-rays from within this mirror image can be reflected to the detector.

Johann spectrometers use cylindrically bent crystals, but the intensity is further enhanced by using spherically bent crystals for partial vertical focussing, as described by J. Eggs and K. Ulmer [51]. This helps to counteract the low efficiency that marks all crystal spectrometers. The bending process also leads to a small change  $C_{bend}$  to  $\Theta_B$ , explained in detail in Ref. [52].

The crystals used in the experiment have a diameter of 100 mm and a bending radius of 3 m, which is a compromise between count rate and resolution. They are attached to glass lenses with a diameter of 120 mm by adhesion forces between the thin crystals (thickness 0.3 mm) and the glass surface. Their manufacture is an involved process, done in collaboration with Carl Zeiss company [53]. Elliptically bent crystals would provide complete vertical focussing, but apart from the technical challenges, a different ratio of bending radii is necessary for each wavelength.

The size of the reflection surface can be changed by placing apertures in front of the crystal to decrease the influence of Johann broadening  $\Delta\Theta_J$  and other small geometrical corrections [50]. The optimal compromise between high rates and good resolution, determined in a set of measurements with different apertures, is a rectangular aperture with a width of 60 mm – since the leading contribution to the geometrical broadening of the crystal response is  $\Delta\Theta_J$ , the reflecting surface only needs to be limited horizontally. This crystal aperture is used throughout all beamtimes described herein.

**Corrections to the Bragg law** The corrections to the Bragg angle  $\Theta_B$  described above are specific to bent crystals, but there are some effects that have to be taken into account for all crystal spectrometers.

The refraction of photons upon entering the crystal changes the simple geometry of the Bragg condition for constructive interference by lengthening the path of the photon inside the crystal. This gives a correction  $C_{ref} \propto 1/\sin 2\Theta_B$  [54], which amounts to roughly 1% of the Bragg angles for silicon and quartz crystals at low X-ray energies.  $C_{depth}$  is a geometrical correction for the average penetration depth of X-rays into the crystal. The temperature dependence of the crystal lattice distance  $d$  is taken into account by the crystal temperature correction  $C_{Temp.}$ .

All corrections to the Bragg angle  $\Theta_B$  for the different experimental setups are collected in Sec. 5.1.1. The validity of these corrections has been tested with Monte Carlo simulations for X-ray tracking (details are found in Refs. [55, 56]).

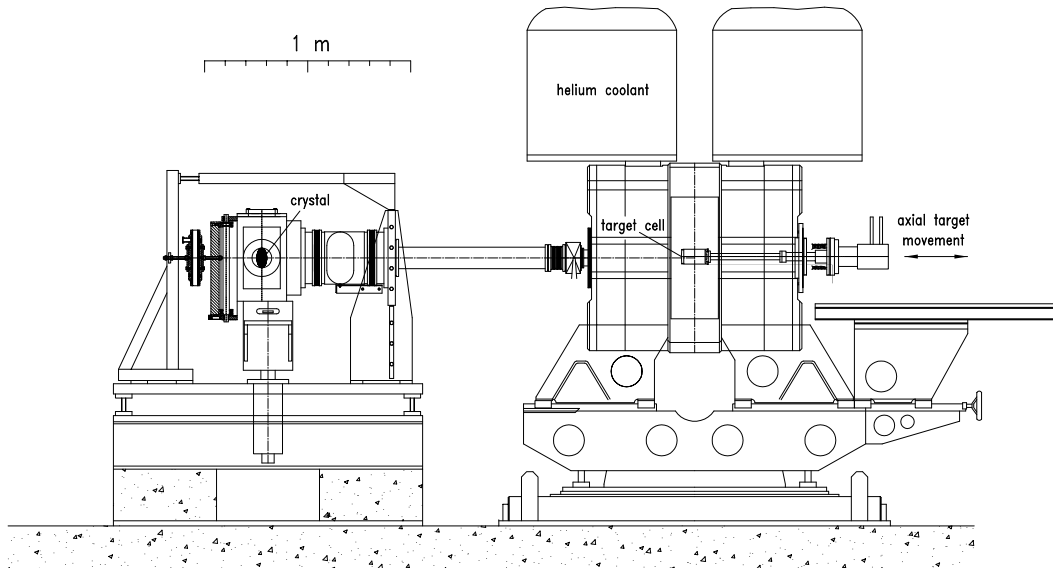


Figure 4.9: Side view of the target arm of the spectrometer. The setup shown is from the  $\pi\text{H}_{3p \rightarrow 1s}$  measurement in the 2002 beamtime.

Apart from these changes of the reflection angle that are important for a correct measurement of the hadronic shift  $\epsilon_{1s}$ , the crystal response function has to be well known to identify its contribution to the total measured line width, from which  $\Gamma_{1s}$  is derived. In addition to the rocking curve for a flat crystal, it also incorporates the changes to the line shape arising from the use of spherically bent crystals. The investigation of the crystal response function is part of the analysis process for the hadronic broadening  $\Gamma_{1s}$  and described there (Sec. 5.3.1).

#### 4.1.5 The spectrometer setup at PSI

The different parts of the spectrometer are seen in detail in Fig. 4.9 and Fig. 4.10. Adjustment of the spectrometer for different Bragg angles  $\Theta_B$  is done online with two stepping motors without the need to enter the experimental area. The crystal housing is connected to the detector arm, which is rotated around the crystal by a linear motor that controls the arm angle  $\Theta_{ARM}$ . Another linear motor is used for individual rotation of the crystal, controlling the angle  $\Theta_{CRY}$  (Fig. 4.11). Once  $\Theta_{CRY}$  is set, a ceramic piezo element controlled by the angular encoder is used to fix this angle with the intrinsic encoder accuracy of  $\pm 0.14$  seconds of arc. A detailed map of the spectrometer control is found in Appendix B.



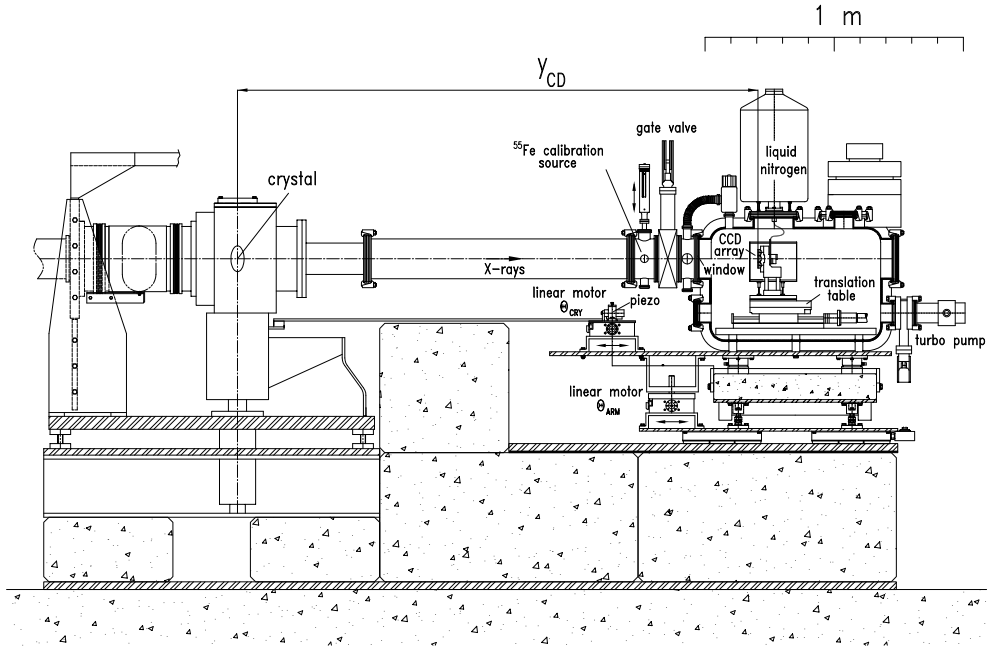


Figure 4.10: Side view of the detector arm of the spectrometer, also with the setup from the  $\pi\text{H}_{3p \rightarrow 1s}$  measurement in the 2002 beamtime. The distance  $y_{CD}$  is taken from the center of the crystal surface to the center of the detector surface.

To set up the apparatus for a certain X-ray energy (and corresponding Bragg angle  $\Theta_B$ ), both motors have to be used: by changing  $\Theta_{ARM}$ , a different target region is aimed at while the position of the reflection on the detector area remains fixed. By changing  $\Theta_{CRY}$ , both the target region and the reflection position are changed. Verification of the spectrometer position is done with X-rays from a fluorescence target, for example the  $\text{Zn } K\alpha_1$  line for measuring the  $\pi\text{H}_{3p \rightarrow 1s}$  transition. With typical fluorescent X-ray event rates of  $\sim 10000$  per hour (compared with pionic X-ray rates of 10-100 per hour), position checks can be done within minutes.

When the spectrometer is correctly positioned, a target scan is performed to determine the optimal position of the detector arm. By measuring the event rate with small increments of  $\Theta_{ARM}$ , the active target surface is mapped (Fig. 4.12). The fastest way to perform such a scan is to fill the gas cell of the target (Fig. 4.5) with argon (at room temperature and  $\approx 500$  mbar pressure) and irradiate it with an X-ray tube.

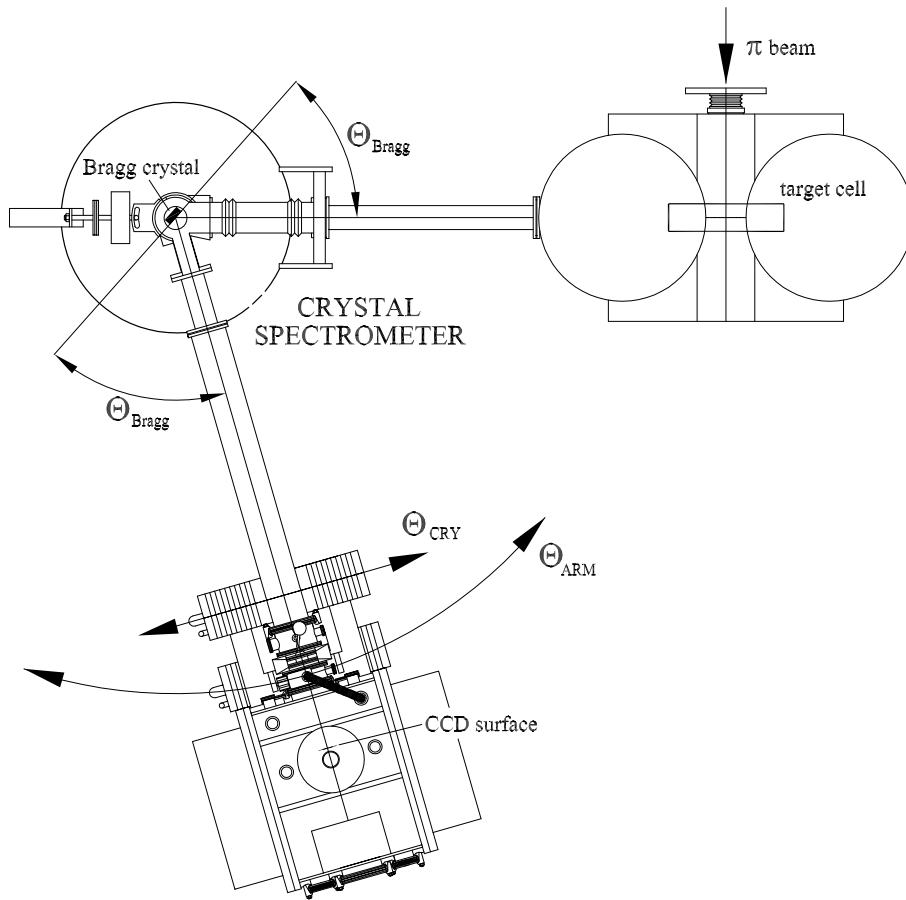


Figure 4.11: Top view of the spectrometer. The angles  $\Theta_{CRY}$  and  $\Theta_{ARM}$  define the spectrometer setting. The Bragg angle is taken between the crystal plane and the direction of incident and reflected X-rays.

#### 4.1.6 CCD detectors

For the position measurement of the reflected X-rays, an array of 6 CCD (Charge Coupled-Device) detectors is used. CCD detectors are semiconductors operating on the same basic principle as other semiconductor photon detectors: incident photons move electrons from the valence band into the conduction band, thereby creating charge in the form of electron-hole pairs. Their pixel structure, however, allows storage of a localised charge. CCDs are normally used in astronomy and, in everyday life, digital cameras.

The CCD detectors of the experiment are made from silicon of  $\sim 300 \mu\text{m}$  thickness, with a fully depleted region of about  $30 \mu\text{m}$ . This is optimal for photons in the few keV range with a penetration depth of a few  $\mu\text{m}$ . Charge

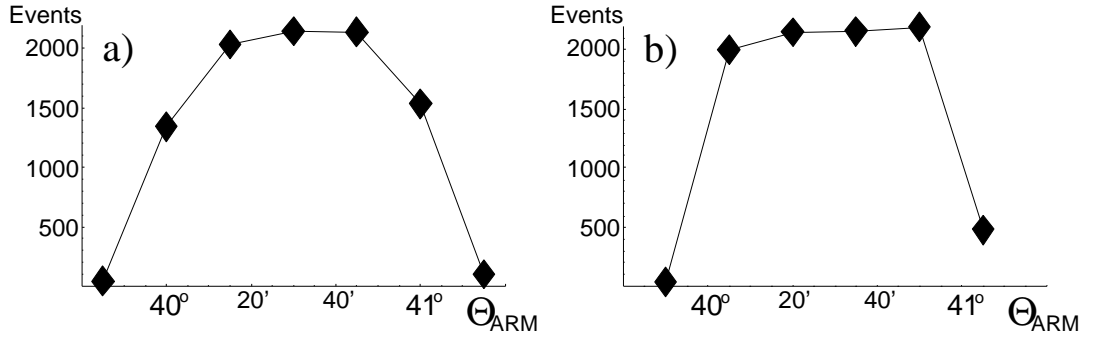


Figure 4.12: **a)** Scan of the target using a target support structure as shown in Fig. 4.5. **b)** Scan of the target with an additional rectangular aperture on the target window. The sharp edges of the event rate distribution provided by an aperture allow a quick determination of the optimal setting for  $\Theta_{ARM}$ .

created deeper within the silicon bulk material by high-energy photons will spread into adjacent pixels (charge splitting).

To read out the whole CCD, the stored charges are shifted into a line readout section. This section is then read out before the next pixel row is moved into the readout section. Through this process, a charge map of all pixels is created which can then be analysed or displayed as an image.

To allow continuation of data taking during the readout (which takes about 20 s), the CCDs have a storage area with the same number of pixels as the image area. For the read out, the stored charges are transferred from the image area into the storage area, which only takes 10 ms. While the data is read out from storage, the image area is immediately available for the measurement again.

The exposure time for a single CCD frame should not be too high to prevent the loss of too many events from pionic X-rays through double hits – at present, the cluster analysis (see Sec. 4.2.3) is not able to distinguish a pionic event if it lies within a background cluster. With the exposure time of 1 min that was used throughout the measurements, about 1% of the image area gets illuminated by background events.

The image area of each individual CCD has  $600 \times 600$  pixels of  $40 \times 40 \mu\text{m}^2$ , giving a total detector area of 48 mm width and 72 mm height with a  $2 \times 3$  CCD chip array (Fig. 4.13). The large area of the detector array allows the simultaneous measurement of lines with similar energies, a very important feature for the energy calibration of the apparatus described in Sec. 4.3.

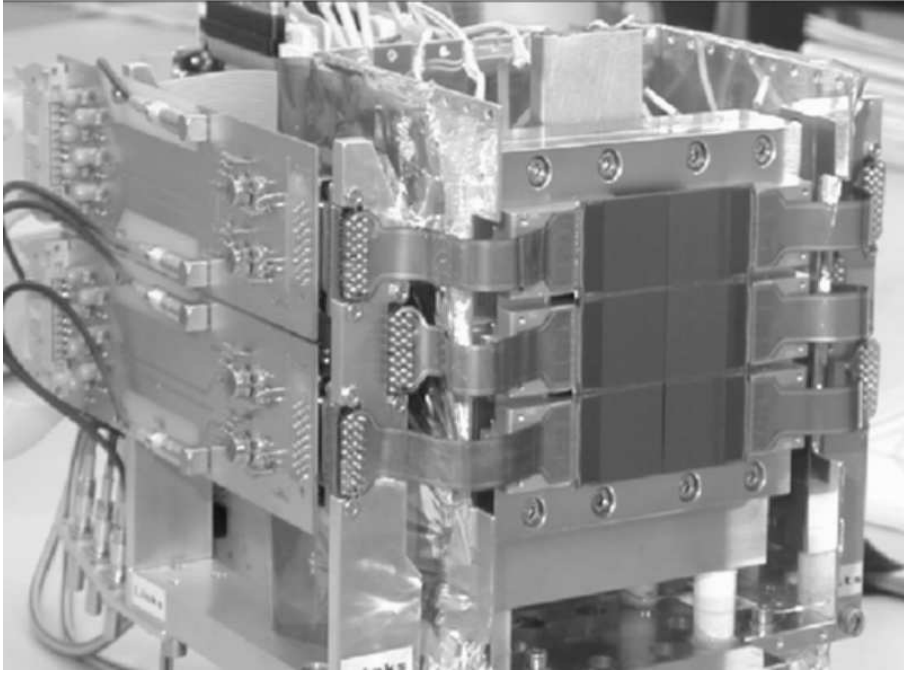


Figure 4.13: Photo of the CCD detector array.

Apart from the positional information, CCD detectors provide the excellent energy resolution (ca. 160 eV at 3 keV) of semiconductor detectors for each individual pixel, which is important for background reduction (see Sec. 4.2.3). In the energy range of the experiment (2-4 keV), the CCDs used in the experiment have a very high quantum efficiency  $\epsilon$  of 80-90%. A detailed description of the CCD detector array is found in Ref. [57].

#### 4.1.7 Event rates and spectrometer efficiency

While the experimental setup does not allow a measurement of absolute X-ray yields due to the lack of an absolute rate normalisation, relative event rates of the various measured transitions with different target densities can be compared. If the total activity  $A_X$  of the X-ray source is exactly known, the calculation of detected events  $n$  is quite straightforward:

$$n = A_X \cdot M \cdot \epsilon \cdot \eta \quad (4.2)$$

with the loss from absorption at target and detector windows  $M$ , the detector efficiency  $\epsilon$  and the spectrometer efficiency  $\eta$ , which is the product of the solid angle of the crystal, its peak reflectivity  $P$  (Fig. 4.7) and the fraction of the source accepted by the spectrometer:  $\eta = \Delta\Omega/4\pi \cdot P \cdot \Delta S/S \approx 10^{-8}$  [56].

In the case of pionic X-rays, however, determination of the source activity is rather difficult. The factors that enter into the calculation are the number of pions from the beam  $N_\pi$ , the stop efficiency (pions stopped in the target cell)  $T$  and the X-ray yield of the radiative transition  $Y$  (Fig. 3.3):

$$A_X = N_\pi \cdot T \cdot Y.$$

The number of pions entering the area cannot be determined absolutely, as the fraction of pions stopped in the target gas is not exactly known. Therefore, the normalisation for  $N_\pi$  has to come from the proton current of the primary accelerator beam. The beam at PSI is usually very stable and as long as this is the case, this is a reliable method. If the meson production target is not hit quite right, however, the relation between proton current and  $N_\pi$  degrades.

Nevertheless, a rough calculation of the expected  $\pi$ H X-ray rates can be performed: with  $N_\pi = 4 \cdot 10^9 s^{-1}$  (Sec. 4.1.1),  $T \approx 10^{-2}$  (Sec. 4.1.2) and  $Y \approx 5 \cdot 10^{-2}$  (Fig. 3.3), the source activity is  $A_X \approx 2 \cdot 10^6 s^{-1}$ . Entering this into Eq. 4.2 together with  $M \approx 3/4$ ,  $\epsilon \approx 4/5$  and  $\eta \approx 10^{-8}$  gives an event rate  $n$  of  $1.2 \cdot 10^{-2} s^{-1}$  or roughly 45 per hour.

## 4.2 Data acquisition and processing

The hardware and software that handles the storage and analysis of the raw CCD data has to be reliably stable and safe against data loss. Beyond that, it also has to be fast enough to allow realtime online analysis – any experiment that depends upon accelerator beamtime cannot afford "blind" measurements with a lot of time between data taking and feedback from analysis. In this section, an overview of the data acquisition network and the software analysis tools is given, with special emphasis on the conversion of the two-dimensional CCD data into position spectra.

### 4.2.1 Data acquisition, transfer and storage

The six CCD detectors are read out by a Virtual Basic program running on a Win95 PC. Their energy calibration is done with a  $^{55}\text{Fe}$  source inserted in front of the CCD array (Fig. 4.10). To get rid of the huge amount of data from thermal noise, only events above an ADC threshold set by the user are recorded after being corrected for the noise offset (Fig. 4.14). For all measurements of this experiment, the threshold was set at  $5\sigma$  above the noise peak, where  $\sigma$  is the rms value of the noise distribution.

One data file for each CCD is produced, consisting of a data header (with date, time, comments and general information) and the events themselves.

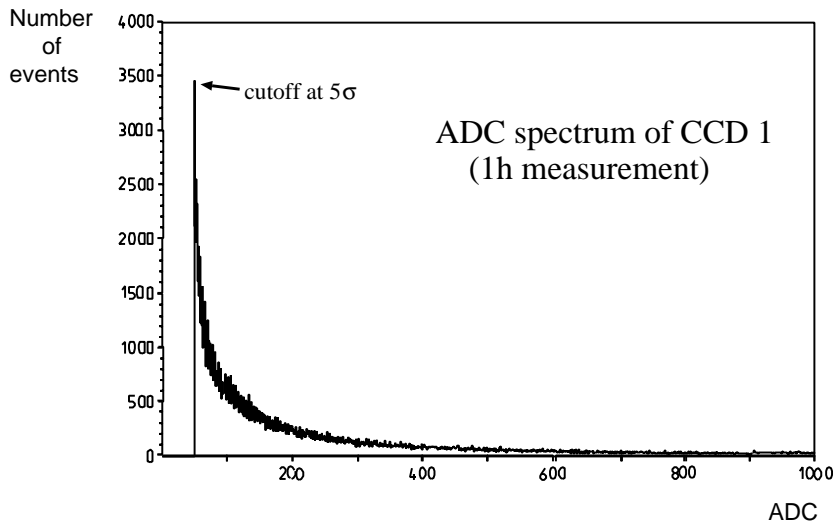


Figure 4.14: ADC plot of CCD data without cluster analysis. The tail of the thermal noise peak is clearly visible even after the cut at  $5\sigma$  performed during data read in. The ADC offset automatically centers the noise peak at channel 0.

Each event is encoded as a 5-byte number with 2 bytes for the ADC value and 3 bytes for the pixel position. Compared with the default data structure – a standard 4-byte integer for both ADC and position – this reduces the amount of data by another 37.5%.

Data files usually consist of 60 frames with 1 min exposure time each. While longer data taking without interruption is possible, the amount of lost data in the (very rare) case of an error during CCD readout would be increased. Additionally, 1 hour blocks of measurements were found to provide a good time schedule for monitoring of the experiment via online analysis and inspections of the spectrometer settings. When a data file is finished, it is transferred to a Linux PC for analysis via a Local Area Network (LAN) connection that is independent of the net at PSI. Copies of the data files are sent to another Linux PC at FZ Jülich at once. To be insured against all eventualities, data files are copied to magnetic tape after beamtimes.

## 4.2.2 The data processing software CSD

Once the data files are transferred and copied, the CSD program is used to produce spectra from the raw data. After reduction of background events above the noise peak through cluster analysis (see Sec. 4.2.3), energy spectra, position spectra or two-dimensional plots can be created. For a further

suppression of background, an ADC spectrum with events from the detector region around the line reflection is used to precisely determine the energy cuts for each CCD. With these energy cuts applied to the data, final spectra are produced.

The correct conversion of raw CCD data into position spectra is a non-trivial and integral part of the experiment – if these spectra are to provide accurate information, the data has to be correctly interpreted. In the following sections, the most important challenges of data processing are explained in detail.

### 4.2.3 Cluster analysis

As has been noted in 3.2, a good signal-to-noise ratio is of crucial importance to the success of the experiment, especially as regards  $\Gamma_{1s}$ . Cluster analysis makes use of the different structure of background events and X-ray events (Fig. 4.15). X-rays from pionic atoms with only a few keV energy will deposit charge within a few  $\mu\text{m}$  of the detector material. This will result in only one activated pixel of the CCD, or two adjacent pixels if the X-ray hit close to a pixel border.

The background in the experimental area consists of beam-induced Compton background – most of the negatively charged pions from the beam get absorbed in solid matter ( $\pi^- + A \rightarrow A' + nn$ ). Heavier nuclei will then deexcite by ejecting more neutrons in addition to  $\gamma$ -rays. The concrete around the spectrometer shields the detector from the high neutron background through moderation of neutrons by the water content of the concrete.

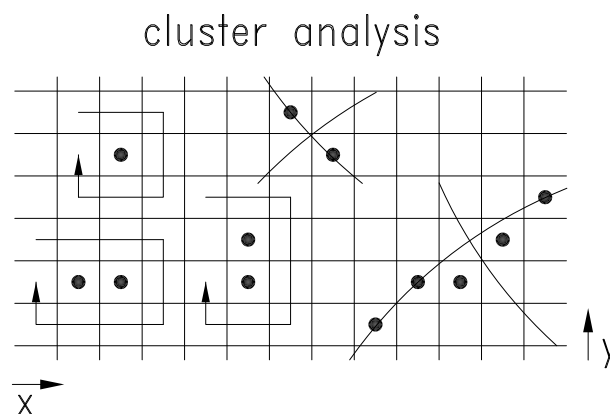


Figure 4.15: Background reduction with cluster analysis separates proper X-rays (isolated or paired events) from background events (clustered events or tracks).

What eventually reaches the detector is secondary background: neutron capture ( $n + A \rightarrow A^* \rightarrow A' + \gamma$ ) results in high energy photons. As noted in Sec. 4.1.6, these photons penetrate beyond the depleted region into the silicon bulk material of the CCDs, which leads to clusters of several pixels through charge splitting. By keeping only isolated events for further analysis, high-energy background events are sorted out. In addition, the Bremsstrahlung background built up by high energy electrons from  $\mu$ -decay has to be separated from pionic X-rays, which is accomplished by applying energy cuts to the cluster-analysed data. Figure 4.16 demonstrates the effectiveness of this method of background suppression.

The old algorithm for the cluster analysis (described in Ref. [58]) worked by pattern recognition: each activated pixel and the eight surrounding pixels were checked against fixed patterns. An isolated pixel was stored as a real (so-called type 1) event. In the case of exactly one other activated pixel, the vicinity of that pixel was checked – an isolated pair was stored as a type 2 event for adjacent pixels and type 2A for diagonally adjacent ones. All other cases (three or more activated pixels in the 3x3 pixel block or non-isolated pixel pairs) were discarded.

While this worked very well with X-rays from pionic atoms with energies up to 4 keV, it was not well suited for lines of higher energies (e.g. the Ga  $K\alpha_1$  line at 9.25 keV or the Zn  $K\alpha_1$  at 8.64 keV used to monitor the spectrometer stability in the 2002 beamtime), since photons from these sources also strike deep enough into the CCD bulk material to cause charge splitting. To allow a proper investigation of high energy X-ray spectra, a new algorithm for the cluster analysis was implemented.

A typical Zn  $K\alpha_1$  X-ray produces clusters of 5-15 pixels (Fig. 4.17). For clusters of this size, there are so many possible forms that pattern recognition is too involved to provide a workable solution.

The new algorithm works as follows: during the analysis, the pixels are checked for ADC charge row by row. If the charge of a pixel is above a certain threshold (set by the user), its position and charge are stored in a temporary buffer and it gets a tag. Then the four directly adjacent pixels are checked with the same procedure, except that an already tagged pixel will be ignored. In this way, a whole cluster of connected pixels is mapped out.

As soon as this search routine runs out of hit pixels not tagged yet, the center of the cluster (weighted by ADC charge) is calculated. The cluster is then stored as a single event positioned at the weighted center with an energy equal to the ADC charge sum. The number of pixels in the cluster is also stored – when producing spectra, this allows to display only events that have a certain number of activated pixels.

A direct comparison of Zn data subjected to the old and the new cluster



### raw data

### cluster-analysed data

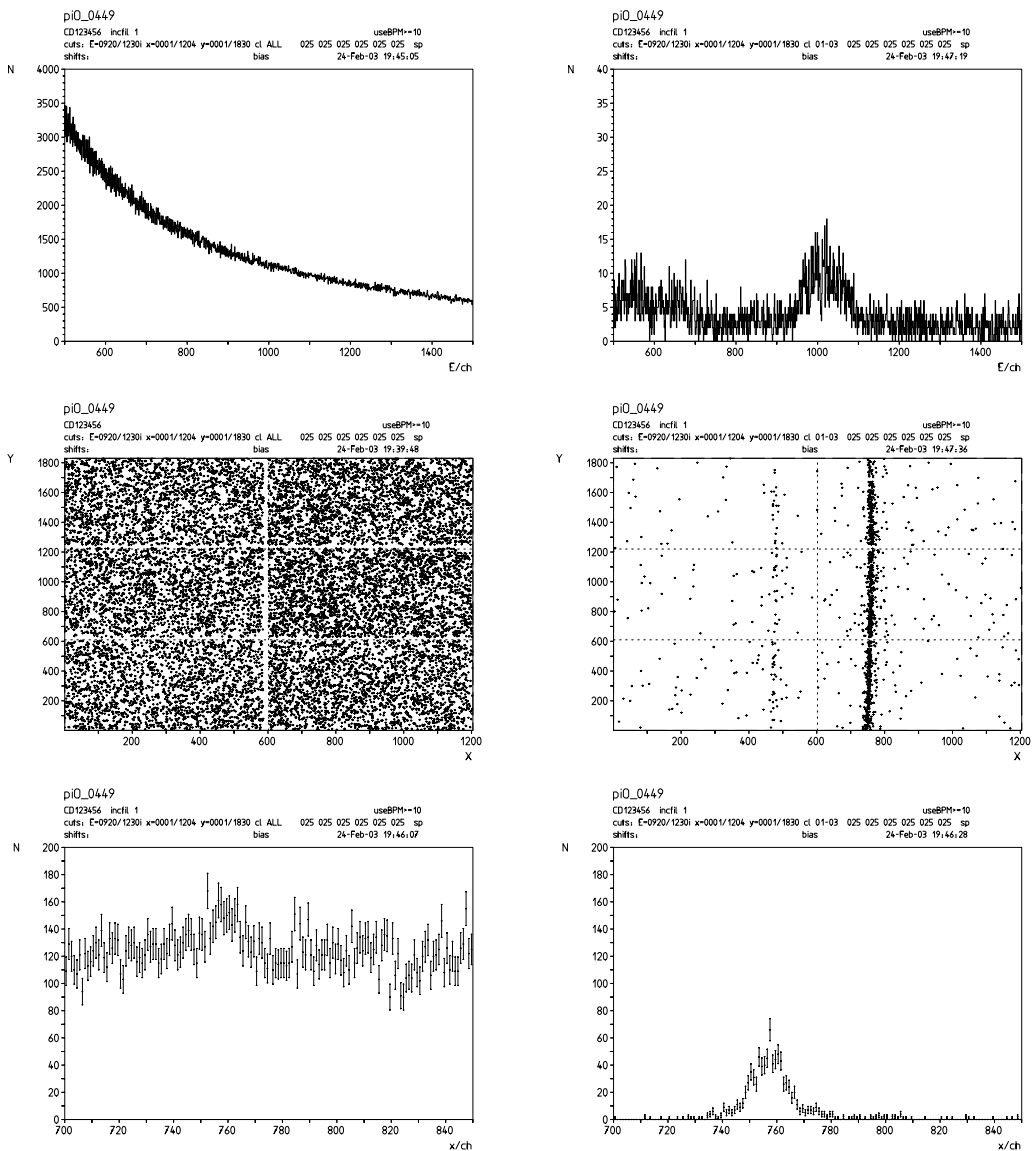


Figure 4.16: 10 hours worth of  $\pi^0$  data from 2002 shown without (left column) and with (right column) cluster analysis. The spectra are direct print-outs of the data analysis software.  $N$  is the number of events. Upper row : ADC spectra. Middle row : 2d-plots of the data (“scatter plots”). Lower row : x-position spectra. For the cluster analysed scatter plot and x-position spectrum, energy cuts are applied.

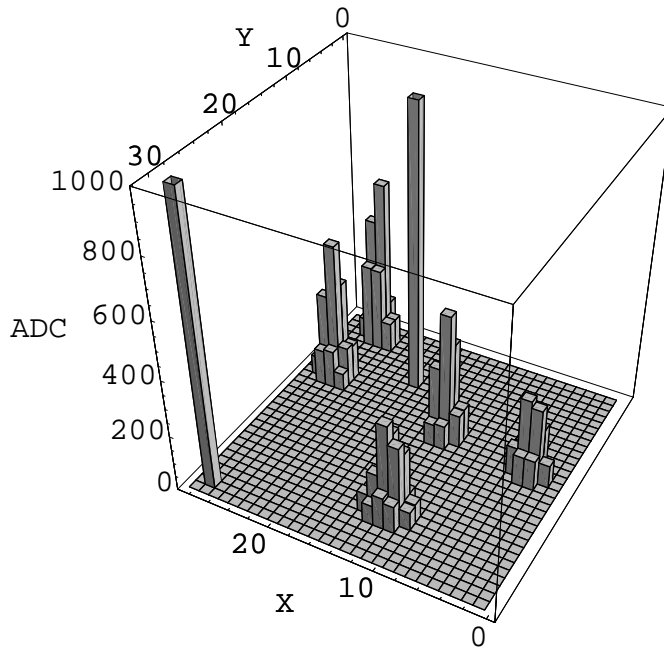


Figure 4.17: Unmodified data from 8 keV X-rays with ADC value as height. There are two events without charge splitting (high charge in a single pixel) and five events with charge splitting (clusters with a distinctive peak in the middle). By setting energy cuts on the charge sum of a cluster, Cu events can be separated from background events.

analysis shows that the old algorithm detected about 20% of the total events. In other words, roughly 80% of Zn X-rays will cause charge splitting that spreads their signature over more than 2 pixels. For pionic X-rays with energies from 2-3 keV, 3-pixel-events amount to less than 1% and there are practically no bigger clusters. A slight increase (3-5%) of 1- and 2-pixel events is due to the fact that isolated pixels lying diagonally adjacent to a bigger cluster were disregarded by the old algorithm and are correctly treated as individual events by the new one.

#### 4.2.4 Position corrections

After cluster analysis, the positions of the remaining events have to be corrected for the alignment of individual CCDs relative to each other and for the curvature of the reflection. Both corrections cause a rebinning of events into the pixel grid, a process wrought with some complications that are discussed in some detail below.

**CCD alignment** The position of events after read-in would only be correct if the individual CCDs were perfectly and seamlessly aligned with each other. In reality, however, there are gaps on the order of 0.3 mm between the CCDs and they are slightly askew, with relative rotations of 1-6 mrad. Events are rotated around the center of each CCD to keep the change in position for each event as small as possible. Then all events on a CCD are shifted to correct for the relative CCD position. A detailed account of how these parameters were measured is found in Appendix A.

**Curvature correction** As has been noted in 4.1.4, the reflection geometry of the spectrometer always leads to a curved rather than a straight reflex on the detector. To determine the real line width and position, this curvature is approximated by a parabolic function  $A + Bx + Cx^2$ . CSD gets the parameters A, B and C by dividing each CCD into several horizontal slices, calculating the centroid of each slice and performing a  $\chi^2$ -fit through these centroids. To reduce the influence of background events on the curvature fit, an iterative method is used: for subsequent fits, only events that lie close enough to the last fit performed are taken into account. The width of this fit interval is set by the user. After a certain number of fits, the result converges and gives the final parameters for the curvature correction. Fig. 4.18 shows the effect of curvature correction in 2d- and 1d-plots.

**Event redistribution** To be reasonably accurate, all three corrections of event positions – rotation, shift and curvature – have to be carried out with real numbers, i.e. with fractions of pixels. However, the position of an event is expressed with integers; a pixel is either activated or not, the detector does not provide any information about the event position within the pixel. To handle this, we assume an isotropic distribution of events and determine the exact position of a single event randomly (one roll for x- and y-coordinate). The corrections are then carried out with these real number coordinates; the new position of the event within the pixel grid is determined by the pixel it finally lands in. Since this process is redone every time a spectrum is produced, spectra from one and the same data set will differ slightly from each other.

An isotropic distribution of events is the easiest assumption to make, but it is not correct and some information is lost thereby. A more thorough method would take the position of the pixel into account – on the flank of a peak, there will obviously be a gradient in event density over the area of one pixel. Disregarding this information causes peaks to broaden a bit with each redistribution of events, but for the typical widths of  $\pi$ H lines, this does not cause a noticeable effect: A FWHM of 25 channels is increased by 0.1

channels after 5 redistributions. To reduce this inaccuracy as much as possible, all position corrections are carried out at once instead of consecutively, which means one random rebinning instead of three (for rotation, shift and curvature correction).

## 4.2.5 The fit routine FITOS

Spectra produced by CSD are numerically fitted by this program, which allows a fit of position, height and width for up to 30 peaks in a spectrum. The line model is a Voigt profile, a convolution of a Gaussian and a Lorentzian distribution. Either the Gauss or the Lorentz width (FWHM) is a free parameter, the other width has to be fixed. Peaks can be coupled together in any parameter – this is useful for the fit of lines with well-known energy

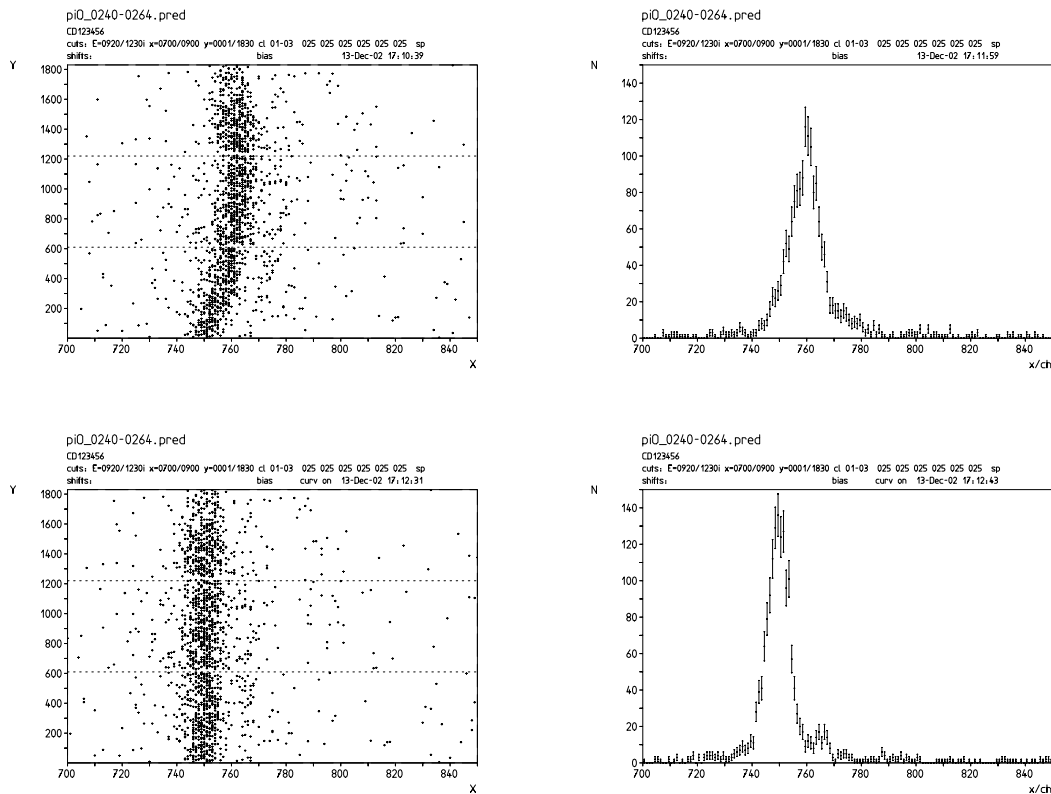


Figure 4.18:  $\pi O$  data from 2002 shown before (upper row) and after curvature correction (lower row). On the left side are 2d-plots (“Scatterplots”), on the right side are x-position spectra. The  $\pi O_{6g \rightarrow 5f}$  parallel transition is clearly visible after curvature correction has been applied.

differences or intensity ratios. The background, described by a flat, linear or parabolical function, can be fixed or used as another free parameter.

While a Voigt profile serves well enough as a description of line shapes in the determination of peak positions (for the measurement of  $\epsilon_{1s}$ ), it is not accurate enough for the extraction of the hadronic broadening  $\Gamma_{1s}$  from the measured line width. Another analysis approach also considering asymmetric line profiles is used for this, described in Sec. 5.3.

### 4.3 Energy calibration

In order to determine the energy of the measured  $\pi\text{H}$  transition, a calibration line of known energy is necessary. The position difference of both lines corresponds to an angular difference which, in turn, corresponds to an energy difference through the Bragg condition. It should be emphasised that the determination of the line energy depends upon the position of the measured line relative to the calibration line, not its absolute position. This reduces the influence of a large number of systematic effects, especially those related to the imaging properties of the spectrometer, since both lines are changed by almost the same amount.

In a new experimental approach taken in the measurement described here, the energy calibration comes from pionic oxygen ( $\pi\text{O}$ ) X-rays. The calibration transition  $\pi\text{O}_{6h \rightarrow 5g}$  is not subjected to the hadronic influence of the oxygen nucleus. Its energy, only dependent on electromagnetic interactions, can thus be calculated very precisely by the methods of QED.

This approach is markedly different from previous experiments, which used fluorescence lines (e.g. the Ar  $K\alpha_1$  for the ETHZ-PSI measurement [5]) for calibration. While electronic X-rays are provided with far higher rates, the achievable accuracy is limited due to their large natural width and the many satellite lines from multiple ionisation. Without knowing exactly which lines make up the spectrum, the energy information provided is not precise enough for the envisaged accuracy.

In addition, the uncertainty of 3 ppm in the mass of the charged pion fully enters into the  $\pi\text{H}$  measurement when fluorescence lines are used for calibration. With pionic calibration lines, this systematic effect is decreased by a factor of seven, since the pion mass is also factored into the energy of the calibration line. Fluorescent lines are, however, used for monitoring the stability of the apparatus, because in this case only the position shift of the line is relevant.

The calibration line has to be measured with the same spectrometer setting as for the  $\pi\text{H}$  transition. Lines from pionic atoms that are so close in energy (depending on the Bragg angle  $\Theta_B$ , the CCD array covers an energy range of about 70-100 eV) are hard to find in the low keV region. Since the transition energy for pionic atoms in solid targets is influenced by electron refilling, the calibration line has to come from a gaseous target, which increases the difficulty of the search. For this reason, there are no pionic calibration lines for other transitions ( $\pi\text{H}_{2p \rightarrow 1s}$  and  $\pi\text{H}_{4p \rightarrow 1s}$ ).

By filling the target cell with a mixture of  $\text{H}_2/\text{O}_2$ , a simultaneous measurement of  $\pi\text{H}$  and calibration line can be accomplished. Time dependent uncertainties that could arise from crystal temperature or mechanical instabilities of the spectrometer will affect both lines in the same way and cannot influence the result for the angular difference. A simultaneous measurement was only possible at a target density of 3.5 bar, since oxygen will freeze out at the temperatures necessary for measurements at higher densities.

**From position measurement to the hadronic shift  $\epsilon_{1s}$**  The steps from measuring the  $\pi\text{H}_{3p \rightarrow 1s}$  line and the  $\pi\text{O}_{6h \rightarrow 5g}$  calibration line to a determination of the hadronic shift  $\epsilon_{1s}$  are as follows:

- The position difference  $\Delta x$  between  $\pi\text{H}$  and  $\pi\text{O}$  lines is converted into the angular difference  $\Delta\Theta$ . This depends on the distance  $y_{CD}$  between the centers of the crystal and the detector surface. Simple geometry gives  $\Delta\Theta = 2 \cdot \arctan \frac{\Delta x}{2 \cdot y_{CD}}$ .
- By subtracting the angular difference  $\Delta\Theta$  from the Bragg angle  $\Theta_B$  of the  $\pi\text{O}$  transition as given by the Bragg law (Eq. refBragg) and correcting for systematical effects ( $C_{\Delta\Theta}$ ), the Bragg angle of the  $\pi\text{H}$  transition is derived.
- With  $\Theta_B$  for  $\pi\text{H}$  calculated, the  $\pi\text{H}_{3p \rightarrow 1s}$  transition energy follows from the Bragg law:

$$E = \frac{hc}{2d} \cdot \frac{1}{\sin\Theta_B}$$

- Subtraction of the pure electromagnetic transition energy  $E_{QED}$  gives the hadronic shift  $\epsilon_{1s}$ .

**Electromagnetic transition energies** To determine the transition energy of the calibration line  $\pi\text{O}_{6h \rightarrow 5g}$  and the electromagnetic transition energy of the  $\pi\text{H}_{np \rightarrow 1s}$  lines, QED corrections to the basic point Coulomb potential energies have to be included. These corrections and the total result for both lines are shown in Table 4.1.

Transition	$\pi\text{O}_{6h\rightarrow 5g}$	$\pi\text{H}_{3p\rightarrow 1s}$
Klein-Gordon + vac. pol. 11	2880.5011 eV	2878.8489 eV
vac. pol. (higher orders)	+ 0.0033 eV	+ 0.0293 eV
Recoil + Magnetic corr.	+ 0.0015 eV	- 0.0510 eV
Self-energy		- 0.0121 eV
Vertex		- 0.0070 eV
<b>total energy <math>E_{\text{QED}}</math></b>	<b>2880.5059 eV</b>	<b>2878.8081 eV</b>

Table 4.1: Electromagnetic transition energies and QED corrections for  $\pi\text{O}_{6h\rightarrow 5g}$  and  $\pi\text{H}_{np\rightarrow 1s}$ . The uncertainty of the  $\pi\text{O}$  value is  $\sim 1$  meV and that of the  $\pi\text{H}$  value is  $\sim 6$  eV [61].

**Bragg angles  $\Theta_B$  and corrections  $C_{\Theta_B}$**  The energies of all relevant measured transitions are given in Table 4.3, along with the important Bragg angles  $\Theta_B$  and the refraction correction  $C_{ref}$ . As the largest correction to  $\Theta_B$ ,  $C_{ref}$  has to be taken into account during the spectrometer setup and not only in the analysis.

Other corrections to the Bragg angle  $\Theta_B$  that have to be applied to both the  $\pi\text{H}$  and the  $\pi\text{O}$  line are collected in Table 4.2. Only the differences of

### Si 111

Corrections to $\Theta_B$	$\pi\text{O}_{6h\rightarrow 5g}$	$\pi\text{H}_{3p\rightarrow 1s}$	Change of $\Delta\Theta$
$C_{Johann}$	- 11.58''/3	- 11.66''/3	- 0.03''
$C_{bend.}$	+ 6.27''	+ 6.25''	- 0.02''
$C_{depth}$	- 0.36''	- 0.37''	- 0.01''
$C_{Temp.}$	- 0.498'' · 2	- 0.497'' · 2	+ 0.00''
$C_{ref.}$	- 24.28''	- 24.20''	+ 0.08''
Total correction $C_{\Delta\Theta}$			+ 0.02''

### Qu 10 $\bar{1}$

Corrections to $\Theta_B$	$\pi\text{O}_{6h\rightarrow 5g}$	$\pi\text{H}_{3p\rightarrow 1s}$	Change of $\Delta\Theta$
$C_{Johann}$	- 14.57''/3	- 14.67''/3	- 0.03''
$C_{bend.}$	+ 5.59''	+ 5.57''	- 0.02''
$C_{depth}$	- 0.32''	- 0.33''	- 0.01''
$C_{Temp.}$	- 2.704'' · 2	- 2.699'' · 2	+ 0.01''
$C_{ref.}$	- 28.28''	- 28.19''	+ 0.09''
Total correction $C_{\Delta\Theta}$			+ 0.04''

Table 4.2: Corrections to the Bragg angle  $\Theta_B$  from the spectrometer imaging properties for the Si111 crystal used in the 2000 and 2002 beamtimes and the Qu 10 $\bar{1}$  crystal used in the 2001 beamtime. An explanation of these corrections is found in Sec. 4.1.4.

these corrections, explained in Sec. 4.1.4, have to be taken into account for the measured angular distance  $\Delta\Theta$ . They are summed up in the angular distance correction  $C_{\Delta\Theta}$ .

For the lattice distance of the Si111 crystal  $2d = 6.2712016(1) \text{ \AA}$  at  $T = 25^\circ\text{C}$  is used [59]. For the Qu  $10\bar{1}$  crystal,  $2d = 6.686277 \text{ \AA}$  [60] is used. As a natural material, quartz has a lattice distance that may vary quite a bit. This systematic uncertainty can be neglected, however, due to the calibration with a nearby line of known energy.

### Si 111

Transition	Energy [eV]	$\Theta_B$	$\Theta_B + C_{ref.}$	$C_{ref.}$
$\pi\text{H}_{3p \rightarrow 1s}(QED)$	2878.808			
$\pi\text{H}_{3p \rightarrow 1s}(QED) + \epsilon_{1s}$	2885.916	43°14'26.74"	43°14'50.94"	24.20"
$\pi^{16}\text{O}_{6h \rightarrow 5g}$	2880.506	43°20'31.37"	43°20'55.65"	24.28"
Ar $\text{K}\alpha_1$	2957.685	41°56'49.05"	41°57'12.24"	23.19"
$\pi\text{Be}_{4f \rightarrow 3d}(1e)$	2844.116	44°2'16.44"	44°2'41.28"	24.84"
Zn $\text{K}\alpha_1$ (Si 333)	8638.860	43°21'31.27"	43°21'34.00"	2.73"
$\pi\text{H}_{2p \rightarrow 1s}(QED)$	2429.506			
$\pi\text{H}_{2p \rightarrow 1s}(QED) + \epsilon_{1s}$	2436.614	54°13'54.78"	54°14'29.28"	34.50"
Ge $\text{K}\alpha_1$ (Si 444)	9886.420	53°7'14.70"	53°7'16.87"	2.17"
$\pi\text{H}_{4p \rightarrow 1s}(QED)$	3036.094			
$\pi\text{H}_{4p \rightarrow 1s}(QED) + \epsilon_{1s}$	3043.202	40°30'57.09"	40°31'19.21"	22.12"
Ga $\text{K}\alpha_1$ (Si 333)	9251.679	39°52'22.37"	39°52'24.78"	2.41"
$\pi\text{C}_{5g \rightarrow 4f}$	2973.826	41°40'5.05"	41°40'28.03"	22.95"

### Qu $10\bar{1}$

Transition	Energy [eV]	$\Theta_B$	$\Theta_B + C_{ref.}$	$C_{ref.}$
$\pi\text{H}_{3p \rightarrow 1s}(QED)$	2878.808			
$\pi\text{H}_{3p \rightarrow 1s}(exp.)$	2885.916	39°58'52.59"	39°59'20.79"	28.20"
$\pi^{16}\text{O}_{6h \rightarrow 5g}$	2880.506	40°4'17.68"	40°4'45.96"	28.28"
$\pi^{18}\text{O}_{6h \rightarrow 5g}$	2883.488	40°1'18.29"	40°1'46.52"	28.23"
Ar $\text{K}\alpha_1$	2957.685	38°49'30.58"	38°49'57.67"	27.08"
$\pi\text{C}_{5g \rightarrow 4f}$	2973.826	38°34'31.20"	38°34'58.04"	26.84"

Table 4.3: Energies and Bragg angles  $\Theta_B$  with the Si111 crystal used in the 2000 and 2002 beamtimes and the Qu  $10\bar{1}$  crystal used in the 2001 beamtime for the  $\pi\text{H}_{np \rightarrow 1s}$  transitions and the calibration line  $\pi^{16}\text{O}_{6h \rightarrow 5g}$ . The  $\pi\text{H}$  transition energies are given as the pure electromagnetic energy  $E_{QED}$  and total energy with the experimental result for  $\epsilon_{1s}$  from the ETHZ-PSI experiment [5]. Also displayed is the Ar  $\text{K}\alpha_1$  fluorescence line, necessary for the spectrometer setup of the  $\pi\text{H}_{3p \rightarrow 1s}$  measurement, and the Zn  $\text{K}\alpha_1$ ,  $\pi\text{Be}_{4f \rightarrow 3d}$  (with 1 electron in the  $K$  shell), Ge  $\text{K}\alpha_1$  and Ga  $\text{K}\alpha_1$  lines used to monitor the spectrometer stability.  $C_{ref.}$  is the index of refraction correction (see Sec. 4.1.4).



# Chapter 5

## Experimental results

Deriving values for the hadronic shift  $\epsilon_{1s}$  from the experimental data is, in principle, a rather straightforward procedure. The two-dimensional image of the reflection on the CCD detector array is converted into a one-dimensional spectrum, which is then numerically fitted. Comparison of the fitted line position with that of a calibration line of known energy gives the total energy of the transition, from which  $\epsilon_{1s}$  can be derived through subtraction of the QED value of transition energy. There are, however, numerous complications throughout this procedure, some of them tied to uncertainties of the measurement process itself, some of them tied to the physical interpretation of the measured parameters.

These various systematic errors are explained in detail throughout the presentation of the experimental results. For the calculation of the hadronic shift  $\epsilon_{1s}$ , the result from the test beamtime of 2000 is used as a thorough example of the various steps from measured data to final result. The descriptions of the two production beamtimes in 2001 and 2002 will build upon this and provide additional explanations of the systematic uncertainties specific to these measurements.

Derivation of the hadronic broadening  $\Gamma_{1s}$  is a more involved process: the contribution of  $\Gamma_{1s}$  to the measured line width has to be separated from the response width of the crystal and Doppler broadening from Coulomb deexcitation. An outline of the analysis approach is given, along with preliminary results.

Before the analysis of data from the three  $\pi\text{H}$  beamtimes conducted so far in the years 2000, 2001 and 2002 is described in detail, an overview of the general measurement strategy and the physics goal for each beamtime is given.

## 5.1 Measurement overview

### 5.1.1 Strategy

As noted in Sec. 3.2, the influence of cascade processes on transitions into the  $\pi\text{H}$  ground state can be investigated by using two experimental parameters: the density of the hydrogen target and the initial  $np$  state from which the transition into the ground state occurs.

The cryogenic target (Sec. 4.1.3) allows measurements with densities up to liquid hydrogen ( $\text{LH}_2$ ). At pressures significantly lower than 3.5 bar, the stop rate of pions – approximately proportional to the target density – is too low to permit an efficient measurement. Given in equivalent pressures, the  $\pi\text{H}_{3p \rightarrow 1s}$  line was measured at 3.5 bar, 28.5 bar (a median value with high expected rate) and  $\sim 700$  bar (liquid hydrogen), providing a range of densities over more than two orders of magnitude.

The study of the three transitions  $\pi\text{H}_{4p \rightarrow 1s}$  (2.9 eV),  $\pi\text{H}_{3p \rightarrow 1s}$  (2.8 eV) and  $\pi\text{H}_{2p \rightarrow 1s}$  (2.4 eV) was conducted at an equivalent target pressure of 10 bar where maximal rates could be expected (Fig. 3.3). As explained in Sec. 3.1, different Doppler contributions to the line shapes allow to test models of the  $\pi\text{H}$  cascade with a very reliable consistency check: if the line width contribution from Coulomb deexcitation is properly understood, the value for  $\Gamma_{1s}$  has to be the same for all  $np \rightarrow 1s$  transitions, since the hadronic influence on the  $np$  states is negligible.

Measurements	target density			
	3.5 bar	10 bar	28.5 bar	$\text{LH}_2$
$2p \rightarrow 1s$		•		
$3p \rightarrow 1s$	•	•	•	•
$4p \rightarrow 1s$		•		

### 5.1.2 2000

Four weeks of preparatory beamtime were used to test the apparatus and to determine event rates of pionic X-rays for the experiment. This was necessary to plan for the production runs that were to come later. The response function of the Si 111 crystal was measured with a pionic carbon line ( $\pi^{12}\text{C}_{5g \rightarrow 4f}$ ) from  $\text{CH}_4$  target gas.

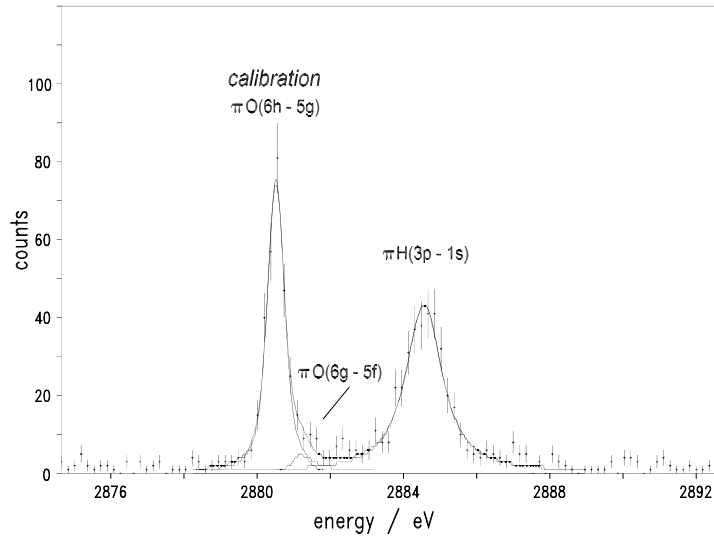


Figure 5.1:  $\pi\text{H}_{3p \rightarrow 1s}$  transition and  $\pi\text{O}$  calibration line from the 2000 beamtime, measured with a Si 111 crystal at a target pressure equivalent to 3.5 bar. The count rate was 10 events/h, the Peak-to-background ratio of the  $\pi\text{H}$  line is 20 to 1.

The same transition ( $\pi\text{H}_{3p \rightarrow 1s}$ ) as in the previous  $\pi\text{H}$  experiment [5] was investigated. By filling the target cell with a mixture of  $\text{H}_2/\text{O}_2$  at 3.5 bar, the calibration line ( $\pi^{16}\text{O}_{6h \rightarrow 5g}$ ) could be measured simultaneously with the  $\pi\text{H}$  line (Fig. 5.1). Due to this, slight mechanical instabilities of the spectrometer affected both lines in the same way and did not influence the result. The gathered statistics were enough to allow a first calculation of  $\epsilon_{1s}$  with roughly the same accuracy as in [5].

### 5.1.3 2001

The first production run of 8 weeks was devoted to the investigation of the density dependence of the  $\pi\text{H}_{3p \rightarrow 1s}$  transition. Given in equivalent pressures, the  $\pi\text{H}$  line was measured at 3.5 bar (same as for the 2000 beamtime), 28.5 bar (a median value with high expected rate) and  $\sim 700$  bar (liquid hydrogen). At 3.5 bar, the  $\pi\text{O}$  calibration line was again measured simultaneously with the  $\pi\text{H}$  line; for higher densities,  $\pi\text{O}$  measurements were conducted in between the  $\pi\text{H}$  blocks. In the latter case, a roughly equal mixture of  $^{16}\text{O}$  and  $^{18}\text{O}$  was used instead of natural oxygen to provide two calibration points instead of just one.

A  $\text{Qu } 10\bar{1}$  crystal was used throughout this beamtime, since the theoretical resolution is a bit better than for Si 111. There was, however, no visible

improvement in the response function measurement, which was again done with the  $\pi^{12}\text{C}_{5g\rightarrow 4f}$  transition, measured from  $\text{CH}_4$  and  $\text{C}_2\text{H}_2$  target gases to identify Coulomb explosion effects (see Sec. 5.3.1).

Mechanical stability was problematic during the 2001 run – during the setup of the experiment, spectrometer and detector were not in mechanical equilibrium, so the connecting vacuum tube was bent a little by the weight of the detector housing. This tension gradually discharged during the beam-time, triggered by, for example, the closing of pressurised vacuum valves or the vibrations of the experimental hall caused by crane driving.

As documented in Fig. 5.2, this discharge process was observable as a change of line positions on the detector. The calibration of the  $\pi\text{H}$  line with  $\pi\text{O}$  has to be corrected for these “jumps” of the spectrometer by fitting a curve to the plotted position development over time. Based on this curve, the fitted positions of  $\pi\text{H}$  and  $\pi\text{O}$  lines are shifted before the distance between them is calculated. To put things into perspective, it should be kept in mind that the accumulated position shift of ca. 5 pixels amounts to only 0.2 mm.

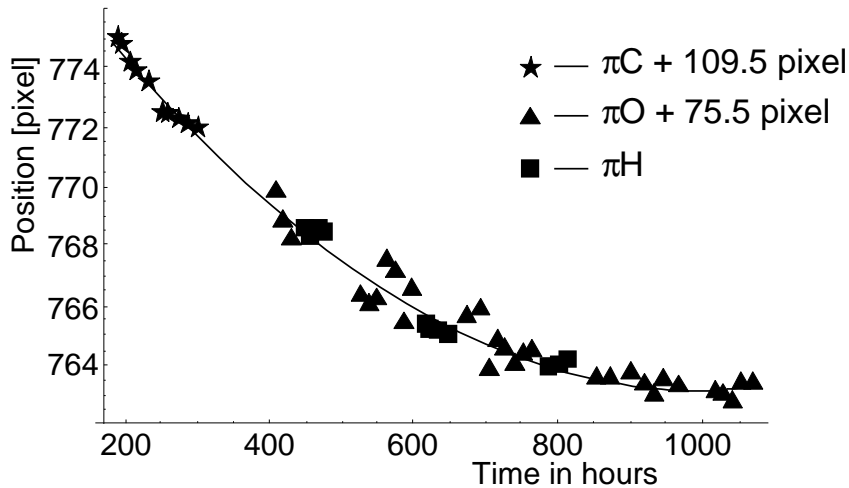


Figure 5.2: Peak positions of  $\pi\text{C}$ ,  $\pi\text{O}$  and  $\pi\text{H}$  measurements in 2001. The time development is approximated by a parabolic fit  $x(t) = A + Bt + Ct^2$ .

#### 5.1.4 2002

The production run of 2002 had its emphasis on the investigation of Coulomb deexcitation through measurement of different  $\pi\text{H}_{np\rightarrow 1s}$  transitions. Since there are no nearby pionic lines to calibrate the energy of the  $\pi\text{H}_{4p\rightarrow 1s}$  and  $\pi\text{H}_{2p\rightarrow 1s}$ , only the  $\pi\text{H}_{3p\rightarrow 1s}$  provides data on  $\epsilon_{1s}$ .

The crystal was the same as used in the 2000 beamtime (Si111). The response function was not measured again, mainly due to time constraints. Prompted by the mechanical problems of 2001, an air cushion system was installed at the detector chamber, with the idea that frictionless movement would make it easier to set up the spectrometer without creating mechanical strain on the components. While principally sound, this did not completely remove the stability issues. Sheer inertia of the heavy ( $\sim 300$  kg) detector housing still bends the vacuum connection between crystal and detector, causing slight (ca. 1 pixel) jumps of line positions.

To monitor such position shifts, two methods were used. For the first  $\pi\text{H}/\pi\text{O}$  block, the beryllium foils placed in the target cell were used, so that the  $\pi\text{Be}_{4f\rightarrow 3d}$  line at 2844 eV could be measured simultaneously with  $\pi\text{O}$  and  $\pi\text{H}$  (Fig. 5.3. While the  $\pi\text{Be}$  transition would be sharp enough to calibrate the energy of the  $\pi\text{H}$  line, but its larger energy distance compared with the  $\pi\text{O}$  line would increase the systematical error arising from asymmetrical defocusing. Additionally, the transition energies of pionic X-rays from solid targets are modified by the unknown electron shell configuration – while electrons are emitted by internal Auger effect, they get replenished immediately from the electron gas around the pionic atom. Similar to fluorescence X-rays, the energy of the line is not exactly known, even if its position can be determined very precisely. In a consecutive measurement of  $\pi\text{H}$  and the  $\pi\text{O}$  calibration, however, the simultaneously measured  $\pi\text{Be}$  line can be used to correct for shifts of the spectrometer position.

For the remainder of the  $\pi\text{H}_{3p\rightarrow 1s}$  data, only the zinc  $K\alpha$  line was used as a stability monitor. Zinc measurements were performed every morning and

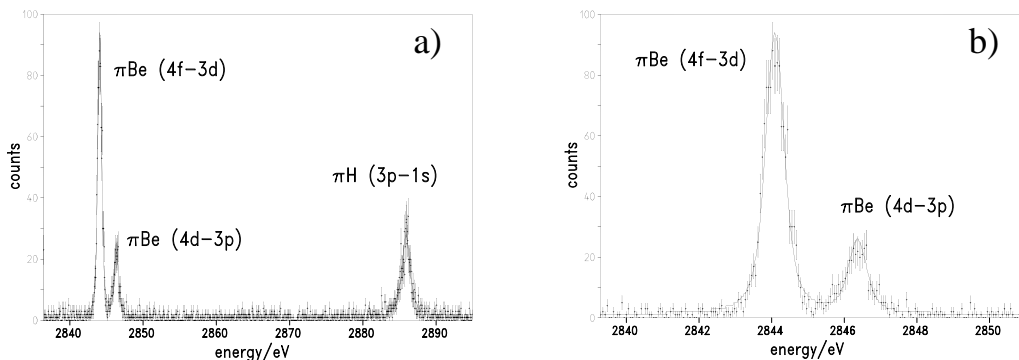


Figure 5.3: **a)** Simultaneous measurement of the  $\pi\text{Be}_{4f\rightarrow 3d}$  with the  $\pi\text{H}_{3p\rightarrow 1s}$  transition; **b)** shows the  $\pi\text{Be}$  line (used to monitor the spectrometer stability) in detail. The parallel transition  $\pi\text{Be}_{4d\rightarrow 3p}$  is clearly visible.

evening during both  $\pi\text{H}$  and  $\pi\text{O}$  measurements, and as for  $\pi\text{Be}$ , the idea was to use the zinc  $\text{K}\alpha$  line as a bridge between  $\pi\text{H}$  and the  $\pi\text{O}$  calibration line. This is described in more detail in Sec. 5.2.3.

Each of the three  $\pi\text{H}$  transitions measured in this beamtime ( $\pi\text{H}_{3p \rightarrow 1s}$  in blocks 2002-1&2,  $\pi\text{H}_{4p \rightarrow 1s}$  in 2002-3 and  $\pi\text{H}_{2p \rightarrow 1s}$  in 2002-4) required a different mechanical spectrometer setup. Gallium and germanium fluorescence X-rays were used to check the spectrometer stability for the  $\pi\text{H}_{4p \rightarrow 1s}$  and  $\pi\text{H}_{2p \rightarrow 1s}$  transitions, respectively.

## 5.2 Results for $\epsilon_{1s}$

### 5.2.1 2000

Several short measurements of  $\pi\text{H}$  were conducted during this test beamtime. Since the  $3p \rightarrow 1s$  transition was taken simultaneously with the  $\pi\text{O}$  calibration line, small jumps of the line positions due to mechanical instabilities did not influence the position difference between them. This means that the different blocks of measurements can be added together for analysis. The data files used for spectrum creation are given in Table 5.1, which is explained in the following two paragraphs.

**Fit of the peak positions** The position spectrum from the second data block is shown in Fig. 5.1. Apart from the statistical error of the numerical fit  $\Delta_{fit}$  of the  $\pi\text{O}$  and the  $\pi\text{H}$  peak, the influence of the various processes of spectrum creation as described in Sec. 4.2.4 has to be taken into account: for the conversion of the two-dimensional hit pattern on the CCD array into a position spectrum, the data has to be corrected for the image curvature caused by the spectrometer geometry ( $C_{curve}$  and  $\Delta_{curve}$ ) and for the slight offsets of the individual CCDs from a perfect rectangular grid (no discernible effect on line position).

The curvature fit is always determined from the  $\pi\text{O}$  line with an interval of  $\pm 3$  pixels aligned to the curvature (see Sec. 4.2.4). To test the sensitivity of the position distance  $\Delta x$  on the curvature parameters, another spectrum with a curvature correction based on an interval of 4 pixels is produced. The change to the position difference when fitting these spectra gives the correction  $C_{curve}$  and the error  $\Delta_{curve}$ .

The corrections for curvature and CCD alignment require a random rebinning of all events into the two-dimensional pixel grid. To determine the effect of this rebinning on the line position, 1000 spectra are created and numerically fitted for each measurement. The distribution of fitted positions

Measurement:	2000 (3.5 bar)	
Data files	107-113 + 133-161 + 231-256	
Transition	$\pi\text{O}$	$\pi\text{H}$
Position [pixel]	732.549	822.388
$\Delta_{fit}$	$\pm 0.258$	$\pm 0.685$
$\Delta_{redist.}$	$\pm 0.029$	$\pm 0.032$
$C_{curve}$ and $\Delta_{curve}$	$-0.029 \pm 0.029$	
$\Delta_{fitregion}$	$\pm 0.010$	
$\Delta x$ [pixel]	$89.810 \pm 0.733 \pm 0.034$	

Table 5.1: Result from 2000 for the position difference  $\Delta x$  of the  $\pi\text{H}_{3p \rightarrow 1s}$  and the  $\pi\text{O}_{6h \rightarrow 5g}$  transition, given as  $value \pm \Delta_{stat} \pm \Delta_{sys}$ .

is a Gaussian and can be evaluated itself by FITOS. Its center gives the position result used for further analysis, its standard deviation  $\sigma$  gives the error  $\Delta_{redist.}$ .

There are very few systematic errors involved in the fitting process itself. A wrong model of the crystal response function will shift both calibration and  $\pi\text{H}$  line, and  $\Delta_{fitregion}$ , the effect of the chosen fit region on the position is miniscule. Both of these effects are far more important for determination of the line width.

In addition to the  $\pi^{16}\text{O}_{6h \rightarrow 5g}$  transition used for calibration, two of the parallel transitions are also strong enough to be noticeable. In the fit routine, their position is fixed relative to the circular  $6h \rightarrow 5g$  transition, whereas their relative intensities are free – their energies are well known, but there is too little information about the cascade mechanisms that determine the populations of the  $l$  substates to provide accurate intensity ratios of parallel transitions.

The target gas was a mixture of hydrogen and natural oxygen, so there is also an isotope line from  $^{18}\text{O}$ . Apart from its position relative to the calibration line  $\pi\text{O}_{6g \rightarrow 5f}$ , the relative intensity of this line is also fixed by the natural  $^{18}\text{O}$  abundance of 0.2%.

**Position distance**  $\Delta x$  is determined by subtracting the  $\pi\text{O}$  peak position from the  $\pi\text{H}$  position and correcting with  $C_{curve}$ . Since  $\Delta_{redist.}$  is dependent on the number of events, it is part of the statistical error  $\Delta_{stat}$ :

$$\Delta_{stat} \equiv \sqrt{\Delta_{fit}^2 + \Delta_{redist.}^2}$$

All remaining effects are systematic and summed up in  $\Delta_{sys}$ . In the following, all results are given as

$$value \pm \Delta_{stat} \pm \Delta_{sys}$$

<b>2000 (3.5 bar)</b>	<i>value</i>	$\Delta_{stat}$	$\Delta_{sys}$
$\Delta x$ [pixel]	89.810	$\pm 0.733$	$\pm 0.034$
$\Delta x$ [mm]	3.5924	$\pm 0.0293$	$\pm 0.0014$
$\Delta\Theta$ (uncorrected)	6'2.11"	$\pm 2.95''$	$\pm 0.14''$
$C_{\Delta\Theta}$	+ 0.02"		
$\Delta_{y_{CD}}$			$\pm 0.18''$
$C_{foc.}$ and $\Delta_{foc.}$	- 0.10"		$\pm 0.02''$
$\Delta\Theta$ (corrected)	6'2.03"	$\pm 2.95''$	$\pm 0.23''$
$\Theta_B(\pi H)$	43°14'29.34"	$\pm 2.95''$	$\pm 0.23''$
<b>Measured energy [eV]</b>	<b>2885.876</b>	<b><math>\pm 0.044</math></b>	<b><math>\pm 0.003</math></b>

Table 5.2: Corrected Bragg angle  $\Theta_B$  and transition energy of the  $\pi H_{3p \rightarrow 1s}$  transition measured in 2000 with a Si111 crystal. For an explanation, see text.

**$\pi H$  Bragg angle and transition energy** The steps from  $\Delta x$  to the measured energy of the  $\pi H_{3p \rightarrow 1s}$  transition are summarised in Table 5.2.

To convert  $\Delta x$  from pixel to mm, it is simply multiplied by the pixel width of  $40 \mu m$ . The uncertainty of the pixel size will affect all measurements in the same way and is dealt with in the summary of results (Sec. 5.2.4). The angular distance  $\Delta\Theta$  follows from the crystal-detector distance  $y_{CD} = (2046.3 \pm 1.0)$  mm. The uncertainty of 1 mm leads to  $\Delta_{y_{CD}}$ .

Most corrections from the spectrometer imaging properties are encoded in  $C_{\Delta\Theta}$ , the sum of all corrections that have to be applied to both lines simultaneously (summarised in Table 4.2 in Sec. 5.1.1).

There is another systematic error and correction from defocussing. It is not possible to fulfill the focal condition ( $y_{CD} = R \cdot \sin \Theta_B$ ) for both the  $\pi H$  and the  $\pi O$  line at once due to their differing Bragg angles  $\Theta_B$ . Since the exact line shape of the  $\pi H$  line is important for determining the hadronic broadening  $\Gamma_{1s}$ , it is put in focus. Accordingly, the slight distortion and position shift of the  $\pi O$  line from defocussing has to be corrected for. This correction  $C_{foc.}$  and the error  $\Delta_{foc.}$  are derived from Monte Carlo studies that have been tested with experimental data from pionic neon.

Another possible source of error would be a wrong facing of the CCD array – if the detector surface is not perpendicular to  $y_{CD}$ , this will lengthen  $\Delta x$  for a given  $\Delta\Theta$ . Like the uncertainty of the pixel size, this systematic effect would influence all measurements and is handled in Sec. 5.2.4.

With the corrected value for  $\Delta\Theta$ , the Bragg angle  $\Theta_B$  for  $\pi H$  is determined from the  $\pi O$  Bragg angle (Table 4.3). The transition energy is calculated from Bragg's law (see Sec. 4.3). The result for the  $\pi H_{3p \rightarrow 1s}$  transition energy, shown in Table 5.2, is on the same order of accuracy as the result of the ETHZ-PSI experiment ( $E_{meas.} = (2885.916 \pm 0.013 \pm 0.033)$  eV [5]).



It is readily apparent that the experimental uncertainty is dominated by  $\Delta_{stat}$  – a longer measurement under these conditions would have improved the result noticeably. The test beamtime of 2000 demonstrated that the accuracy goal of 0.2% total uncertainty for  $\epsilon_{1s}$  with a simultaneous energy calibration from the  $\pi\text{O}_{6h \rightarrow 5g}$  transition is achievable using this experimental setup.

## 5.2.2 2001

In 2001, five blocks of  $\pi\text{H}$  data were measured: three measurements with an equivalent target pressure of 28.5 bar, a measurement with liquid hydrogen ( $\sim 700$  bar) and finally a simultaneous measurement of  $\pi\text{H}$  and  $\pi\text{O}$  with the same target conditions as in 2000 (3.5 bar).

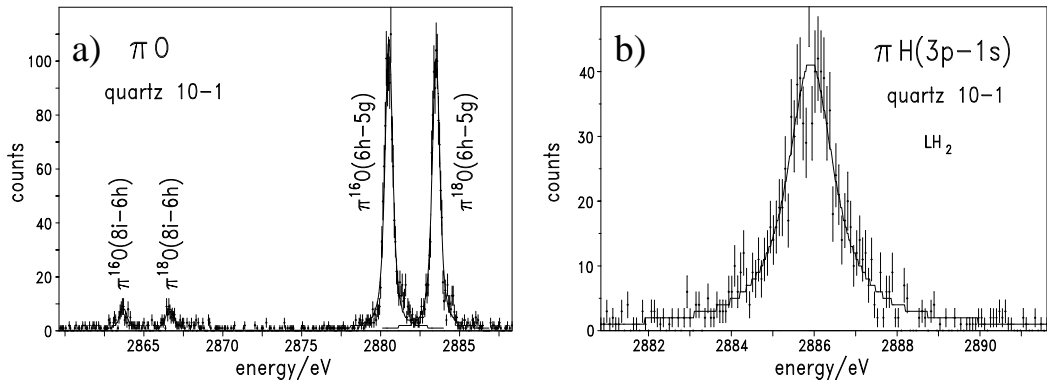


Figure 5.4: **a)**  $\pi^{16}\text{O}_{3p \rightarrow 1s}$  and  $\pi^{18}\text{O}_{3p \rightarrow 1s}$  calibration lines and **b)** the  $\pi\text{H}_{3p \rightarrow 1s}$  transition with a liquid hydrogen target. Both spectra are from the 2001 beamtime, measured with a Qu 10 $\bar{1}$  crystal.

**Measurements at 28.5 bar** For higher target densities, simultaneous measurement of  $\pi\text{H}$  transition and  $\pi\text{O}$  calibration line is not possible, since the oxygen in the target would freeze out. This means that data blocks of  $\pi\text{H}$  have to be interspersed with calibration measurements of the  $\pi\text{O}$  line. Too long periods of measurement will amplify the influence of long term systematic errors due to temperature changes or mechanical effects. On the other hand, a change of the target gas takes at least 8 hours during which no data can be taken, so measurement periods should not be too short, either. A good compromise was found by measuring  $\pi\text{H}$  from Wednesday nights to Sunday mornings and  $\pi\text{O}$  from Sunday evenings to Wednesday mornings. With this schedule, the target gas change coincided nicely with accelerator maintenance

on Wednesdays and refilling of the helium coolant for the cyclotron trap on Sundays and Wednesdays.

As noted in the beamtime overview (see Sec. 5.1.3), a mixture of  $^{16}\text{O}/^{18}\text{O}$  was used for the  $\pi\text{O}$  measurements. In addition to the various  $\pi\text{O}_{6\rightarrow 5}$  transitions, a spectrum of the  $\pi\text{O}$  calibration lines in Fig. 5.4 shows two peaks of lower energy – these are from the  $\pi\text{O}_{8i\rightarrow 6h}$  transitions in  $^{16}\text{O}$  and  $^{18}\text{O}$  at 2880.506 eV and 2883.488 eV. While these transitions are not strong enough to provide an accurate dispersion measurement, their relative intensities give information about the populations of the  $l$  substates in the  $\pi\text{O}$  cascade.

**Corrections for mechanical instabilities** In addition to the systematic errors that have already been described for the 2000 beamtime in Sec. 5.2.1, the stability of the spectrometer – not an issue for simultaneous measurements of  $\pi\text{H}$  and  $\pi\text{O}$  – has to be investigated. From a numerical fit to the line positions plotted against time, a correction  $C_{jump}$  to the average result of one data block is calculated.

The time development of the fitted peak positions is described by a parabolic fit ( $x(t) = A + Bt + Ct^2$ ), with the positions of  $\pi\text{O}$  and  $\pi\text{C}$  lines adjusted by 75.5 pixel and 109.5 pixel, respectively. This model describes the data very well, as can be seen in Fig. 5.2. Position corrections to the fitted peak positions of  $\pi\text{H}$  and  $\pi\text{O}$  spectra were derived by calculating the value of the parabolic fit at the central time of a measurement block:

$$C_{jump} = x(\bar{t}_{\pi\text{O}}) - x(\bar{t}_{\pi\text{H}}) = B \cdot (\bar{t}_{\pi\text{O}} - \bar{t}_{\pi\text{H}}) + C \cdot (\bar{t}_{\pi\text{O}}^2 - \bar{t}_{\pi\text{H}}^2).$$

Corrections $C_{jump}$	12 h increments		whole blocks
	Files	$\pi\text{C}$ , $\pi\text{O}$ & $\pi\text{H}$	$\pi\text{O}$ & $\pi\text{H}$
$\pi\text{H}$ 197-224 and $\pi\text{O}$ 225-261	-0.818(62)	-0.795	-0.811
$\pi\text{H}$ 262-329 and $\pi\text{O}$ 330-365	-1.339(129)	-1.313	-1.330
$\pi\text{H}$ 366-450 and $\pi\text{O}$ 451-485	-0.668(95)	-0.666	-0.665
$\pi\text{H}$ 495-600 and $\pi\text{O}$ 601-661	-0.100(144)	-0.141	-0.107

Table 5.3: Results for the correction  $C_{jump}$  with different data bases. For the first two columns, the peak positions used for the parabolic fit are from spectra of 12 h measurement increments; in the second column, the data points from  $\pi\text{C}$  are not taken into account. For the third column, the peak positions are from sum spectra of whole measurement blocks – the same positions that were used in the final analysis. Compared to the uncertainties  $\Delta_{jump}$  (only given for the first column), the results do not diverge.

<b>Measurement:</b>	2001-1 (28.5) bar		2001-2 (28.5) bar		2001-3 (28.5) bar	
Data files	225-261	197-224	330-365	262-329	451-485	366-450
Transition	$\pi\text{O}$	$\pi\text{H}$	$\pi\text{O}$	$\pi\text{H}$	$\pi\text{O}$	$\pi\text{H}$
Position [pixel]	694.315	770.291	691.387	768.243	689.976	766.106
$\Delta_{fit}$	$\pm 0.081$	$\pm 0.363$	$\pm 0.093$	$\pm 0.229$	$\pm 0.093$	$\pm 0.224$
$\Delta_{redist.}$	$\pm 0.012$	$\pm 0.020$	$\pm 0.013$	$\pm 0.013$	$\pm 0.013$	$\pm 0.013$
$C_{curve}$ and $\Delta_{curve}$	$+ 0.020 \pm 0.020$		$+ 0.020 \pm 0.020$		$+ 0.029 \pm 0.029$	
$C_{jump}$ and $\Delta_{jump}$	$- 0.818 \pm 0.062$		$- 1.339 \pm 0.129$		$- 0.668 \pm 0.095$	
$\Delta_{fitregion}$	$\pm 0.010$					
$\Delta x$ [pixel]	$75.358 \pm 0.373 \pm 0.066$		$75.537 \pm 0.248 \pm 0.131$		$75.491 \pm 0.243 \pm 0.100$	
average $\Delta x$ [pixel]	$75.481 \pm 0.159 \pm 0.062$					

Table 5.4: Results from 2001 for the position difference  $\Delta x$  of the  $\pi\text{H}_{3p \rightarrow 1s}$  and the  $\pi^{16}\text{O}_{6h \rightarrow 5g}$  transition, given as  $value \pm \Delta_{stat} \pm \Delta_{sys}$ . All three measurements were conducted with an equivalent target pressure of 28.5 bar.

For the uncertainty  $\Delta_{jump}$  of this correction, the vertex of the parabola (at  $t = 1010$ ) is taken as the point of greatest stability:

$$\Delta_{jump} = \sqrt{(\Delta B \cdot (\bar{t}_{\pi\text{O}} - \bar{t}_{\pi\text{H}}))^2 + (\Delta C \cdot ((1010 - \bar{t}_{\pi\text{O}})^2 - (1010 - \bar{t}_{\pi\text{H}})^2))^2}.$$

The validity of the parabolic model for this correction was tested by fitting only part of the available data ( $\pi\text{H}$  and  $\pi\text{O}$  positions) and by fitting the parabola to the peak positions in spectra from whole data blocks instead of small time increments (12 hours). As can be seen in Table 5.3, the results for the corrections  $C_{jump}$  in the different data blocks agree very well with each other. For the final analysis, the result from the whole period ( $\pi\text{C}$ ,  $\pi\text{O}$  and  $\pi\text{H}$ ) with 12 h increments was used.

**Derivation of the transition energy** With the corrections for curvature fit and spectrometer instabilities applied, the results for the position difference  $\Delta x$  from the three 28.5 bar measurement blocks are in good agreement with each other (see Table 5.4). For further analysis the weighted average of  $\Delta x$  is used. Since the systematic effects  $\Delta_{sys}$  are largely independent of each other for each of the three results (the sole exception is  $\Delta_{fitregion}$ , which does not contribute noticeably), the systematic error  $\Delta_{sys}$  of the weighted average is also reduced.

The steps from  $\Delta x$  to the measured transition energy  $E$ , summarised in Table 5.5, are the same as for the 2000 measurement, but with a crystal-detector distance of  $y_{CD} = (1915.6 \pm 1.0)$  mm – the focal distance changes according to the different Bragg angles  $\Theta_B$  with the  $\text{Qu } 10\bar{1}$  crystal.

<b>2001 (28.5 bar)</b>	<i>value</i>	$\Delta_{stat}$	$\Delta_{sys}$
$\Delta x$ [pixel]	75.481	$\pm 0.159$	$\pm 0.062$
$\Delta x$ [mm]	3.0192	$\pm 0.0064$	$\pm 0.0025$
$\Delta\Theta$ (uncorrected)	5'25.10"	$\pm 0.69''$	$\pm 0.27''$
$C_{\Delta\Theta}$	+ 0.04"		
$\Delta_{y_{CD}} = 1$ mm			$\pm 0.17''$
$C_{foc.}$ and $\Delta_{foc.}$	- 0.10"		$\pm 0.02''$
$\Delta\Theta$ (corrected)	5'25.04"	$\pm 0.69''$	$\pm 0.32''$
$\Theta_B$ ( $\pi\text{H}$ )	39°58'52.58"	$\pm 0.69''$	$\pm 0.32''$
<b>Measured energy [eV]</b>	<b>2885.919</b>	<b><math>\pm 0.012</math></b>	<b><math>\pm 0.005</math></b>

Table 5.5: Corrected Bragg angle  $\Theta_B$  and transition energy of the  $\pi\text{H}_{3p \rightarrow 1s}$  transition measured in 2001 at 28.5 bar with a Qu 10 $\bar{1}$  crystal. For an explanation, see text.

**Measurements at 3.5 bar and with liquid hydrogen** Since the  $\pi\text{O}$  line from the simultaneous measurement at 3.5 bar is also used as the energy calibration of the liquid hydrogen ( $\text{LH}_2$ ) measurement which was measured immediately before, the results from both are listed together. Only the peak position distance of the  $\text{LH}_2$  measurement needs to be corrected for the gradual position change of the spectrometer. The results are collected in Tables 5.6 and 5.7 – apart from  $\Delta_{stat}$ ,  $C_{curve}$  and  $C_{jump}$ , all corrections and uncertainties are the same as for the measurement at 28.5 bar.

<b>Measurement:</b>	2001-4 ( $\text{LH}_2$ )		2001-5 (3.5 bar)	
Data files	601-661	495-600	600-661	
Transition	$\pi\text{O}$	$\pi\text{H}$	$\pi\text{O}$	$\pi\text{H}$
Position [pixel]	688.358	764.035	688.358	763.728
$\Delta_{fit}$	$\pm 0.136$	$\pm 0.310$	$\pm 0.136$	$\pm 0.400$
$\Delta_{redist.}$	$\pm 0.023$	$\pm 0.018$	$\pm 0.023$	$\pm 0.025$
$C_{curve}$ and $\Delta_{curve}$	- 0.007 $\pm$ 0.007		+ 0.016 $\pm$ 0.016	
$C_{jump}$ and $\Delta_{jump}$	- 0.100 $\pm$ 0.144		none	
$\Delta_{fitregion}$	$\pm 0.010$			
$\Delta x$ [pixel]	75.570 $\pm$ 0.340 $\pm$ 0.145		75.386 $\pm$ 0.424 $\pm$ 0.018	

Table 5.6: Results from 2001 for the position difference  $\Delta x$  of the  $\pi\text{H}_{3p \rightarrow 1s}$  and the  $\pi\text{O}_{6h \rightarrow 5g}$  transition, given as *value*  $\pm \Delta_{stat} \pm \Delta_{sys}$ . Measurements were conducted with liquid hydrogen and with an equivalent target pressure of 3.5 bar.

<b>2001 (LH<sub>2</sub>)</b>	<i>value</i>	$\Delta_{stat}$	$\Delta_{sys}$
$\Delta x$ [pixel]	75.570	$\pm 0.340$	$\pm 0.145$
$\Delta x$ [mm]	3.0228	$\pm 0.0136$	$\pm 0.0058$
$\Delta\Theta$ (uncorrected)	5'25.48"	$\pm 1.46''$	$\pm 0.62''$
$C_{\Delta\Theta}$	+ 0.04"		
$\Delta_{y_{CD}} = 1$ mm			$\pm 0.17''$
$C_{foc.}$ and $\Delta_{foc.}$	- 0.10"		$\pm 0.02''$
$\Delta\Theta$ (corrected)	5'25.42"	$\pm 1.46''$	$\pm 0.64''$
$\Theta_B$ ( $\pi H$ )	39°58'52.26"	$\pm 1.46''$	$\pm 0.64''$
<b>Measured energy [eV]</b>	<b>2885.924</b>	<b><math>\pm 0.024</math></b>	<b><math>\pm 0.011</math></b>

Table 5.7: Corrected Bragg angle  $\Theta_B$  and transition energy of the  $\pi H_{3p \rightarrow 1s}$  transition measured in 2001 with liquid hydrogen and a Qu 10 $\bar{1}$  crystal. For an explanation, see text.

<b>2001 (3.5 bar)</b>	<i>value</i>	$\Delta_{stat}$	$\Delta_{sys}$
$\Delta x$ [pixel]	75.386	$\pm 0.424$	$\pm 0.018$
$\Delta x$ [mm]	3.0154	$\pm 0.0170$	$\pm 0.0007$
$\Delta\Theta$ (uncorrected)	5'24.69"	$\pm 1.83''$	$\pm 0.08''$
$C_{\Delta\Theta}$	+ 0.04"		
$\Delta_{y_{CD}} = 1$ mm			$\pm 0.17''$
$C_{foc.}$ and $\Delta_{foc.}$	- 0.10"		$\pm 0.02''$
$\Delta\Theta$ (corrected)	5'24.63"	$\pm 1.83''$	$\pm 0.18''$
$\Theta_B$ ( $\pi H$ )	39°58'53.05"	$\pm 1.83''$	$\pm 0.18''$
<b>Measured energy [eV]</b>	<b>2885.911</b>	<b><math>\pm 0.031</math></b>	<b><math>\pm 0.003</math></b>

Table 5.8: Corrected Bragg angle  $\Theta_B$  and transition energy of the  $\pi H_{3p \rightarrow 1s}$  transition measured in 2001 at 3.5 bar with a Qu 10 $\bar{1}$  crystal. For an explanation, see text.

### 5.2.3 2002

The beamtime of 2002 was mainly devoted to the improvement on the accuracy of  $\Gamma_{1s}$ , but it also provided new data for  $\epsilon_{1s}$  from the measurement of the  $\pi\text{H}_{3p\rightarrow 1s}$  transition. The target pressure of 10 bar provided very high rates, but it precluded a simultaneous measurement of  $\pi\text{H}$  and the  $\pi\text{O}$  calibration line. To control the influence of mechanical instabilities, two lines were used to monitor the line positions: simultaneous measurement of the  $\pi\text{Be}_{4f\rightarrow 3d}$  line for the first data block (2002-1), intermittent measurements of the Zn  $\text{K}\alpha$  line for the second (2002-2).

**Position correction  $\Delta_{jump}$  with  $\pi\text{Be}$**  As noted in Sec. 5.1.4, slight positional changes of the spectrometer between  $\pi\text{H}$  and  $\pi\text{O}$  measurements can be corrected with the  $\pi\text{Be}_{4f\rightarrow 3d}$  line. In the 2002-1 measurement, the fit results for the  $\pi\text{Be}$  position were  $(130.350 \pm 0.318 \pm 0.065)$  pixel during the  $\pi\text{O}$  measurement and  $(132.057 \pm 0.167 \pm 0.037)$  pixel during the  $\pi\text{H}$  measurement. From this, a correction of  $C_{jump} = -1.707$  pixel with an uncertainty of  $\Delta_{jump} = 0.367$  pixel to the position difference is derived.

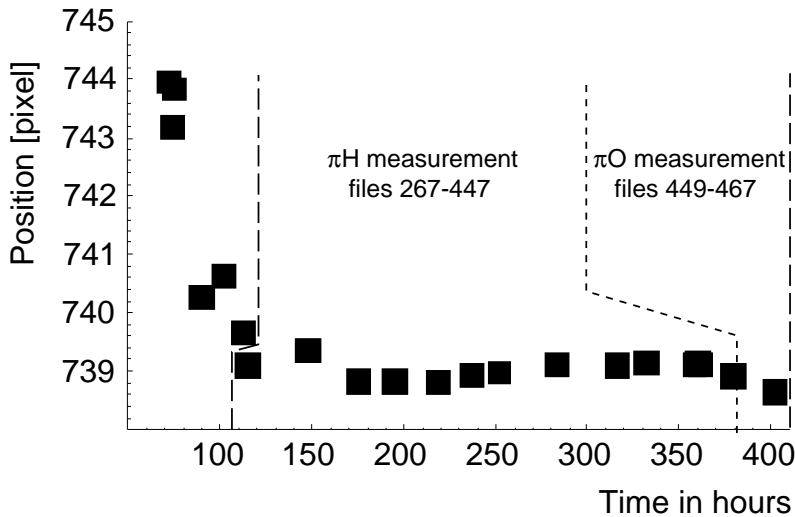


Figure 5.5: Zinc  $\text{K}\alpha_1$  peak positions in 2002. Changes of the spectrometer angle  $\Theta_{ARM}$  before the  $\pi\text{H}$  and  $\pi\text{O}$  blocks caused a jump of more than 4 pixel, but the zinc position did not vary more than  $\pm 0.5$  pixel during the measurements.

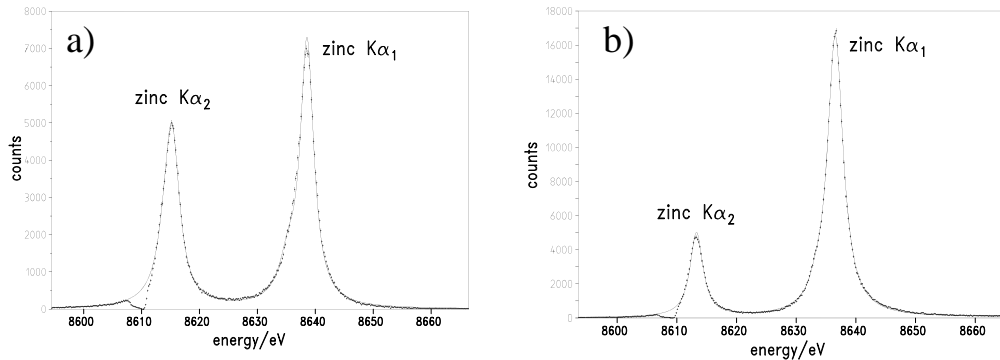


Figure 5.6: Spectra of zinc fluorescence X-rays from before **a)** and after **b)** the 2002-2  $\pi$ H measurement. The difference in relative intensities of the  $K\alpha_1$  and the  $K\alpha_2$  transition is probably caused by the small size of the zinc target.

**Position correction  $\Delta_{jump}$  with Zn  $K\alpha$**  For the 2002-2 data block, measurements with a zinc target placed close to the target cell and irradiated by an X-ray tube were performed twice a day to check the spectrometer stability. The target was so small, however, that the line shape of the Zn spectrum varied strongly, especially regarding the relative line intensities of the  $K\alpha_1$  and  $K\alpha_2$  transitions (Fig. 5.6). In effect, a slight positional change of the spectrometer causes a different change of the fitted peak position because part of the spectrum is not present. Even with this limitation, the development of the Zn  $K\alpha$  position over time (Fig. 5.5), shows that the spectrometer was rather stable throughout the  $\pi$ H/ $\pi$ O data taking.

Analogical to the measurement with  $\pi$ Be, the position distance between  $\pi$ H and  $\pi$ O is corrected by the positional change of the zinc peak. The average position of all zinc measurements conducted during the  $\pi$ H block is 738.953 pixel (the statistical error of the fit is negligible due to the high statistics). For the  $\pi$ O block the result is 738.715 pixel, which gives a correction  $C_{jump}$  of -0.238 pixel. Due to the zinc target problems, the uncertainty of the correction has to be assumed to be roughly as large as the correction itself:  $\Delta_{jump} = 0.25$  pixel.

In spite of this large estimation for the systematic error, the corrected position distances for the 2002-1 and the 2002-2 measurements are not fully consistent with each other. While the calibration with zinc is obviously problematic with a small target, an analysis of the 2002-1 data with the correction  $C_{jump}$  based on the *zinc* measurements conducted during that time gives a corrected  $\Delta x$  of  $(90.19 \pm 0.56 \pm 0.25)$  pixel, which is in perfect agreement with the result based on a correction with  $\pi$ Be. While this is only

<b>Measurement:</b>	2002-1 ( $\pi\text{H}_{3p \rightarrow 1s}$ )		2002-2 ( $\pi\text{H}_{3p \rightarrow 1s}$ )	
Data files	135-167	186-227	449-467	267-447
Transition	$\pi\text{O}$	$\pi\text{H}$	$\pi\text{O}$	$\pi\text{H}$
Position [pixel]	752.776	844.626	747.803	839.501
$\Delta_{fit}$	0.153	0.537	0.130	0.177
$\Delta_{redist.}$	0.017	0.023	0.016	0.008
$C_{curve}$ and $\Delta_{curve}$	+ 0.005 $\pm$ 0.005		- 0.011 $\pm$ 0.011	
$C_{jump}$ and $\Delta_{jump}$	- 1.707 $\pm$ 0.367		- 0.238 $\pm$ 0.250	
$\Delta_{fitregion}$	$\pm$ 0.010			
$\Delta x$ [pixel]	90.148 $\pm$ 0.559 $\pm$ 0.367		91.449 $\pm$ 0.220 $\pm$ 0.250	
average $\Delta x$ [pixel]	91.206 $\pm$ 0.225 $\pm$ 0.196			

Table 5.9: Results from 2002 for the position difference  $\Delta x$  of the  $\pi\text{H}_{3p \rightarrow 1s}$  and the  $\pi\text{O}_{6h \rightarrow 5g}$  transition, given as  $value \pm \Delta_{stat} \pm \Delta_{sys}$ . Measurements were conducted with an equivalent target pressure of 10 bar.

<b>2002 (10 bar)</b>	<i>value</i>	$\Delta_{stat}$	$\Delta_{sys}$
$\Delta x$ [pixel]	91.206	$\pm$ 0.225	$\pm$ 0.196
$\Delta x$ [mm]	3.6482	$\pm$ 0.0090	$\pm$ 0.0078
$\Delta\Theta$ (uncorrected)	6'8.06"	$\pm$ 0.91"	$\pm$ 0.79"
$C_{\Delta\Theta}$	+ 0.02"		
$\Delta_{y_{CD}} = 1$ mm			$\pm$ 0.18"
$C_{foc.}$ and $\Delta_{foc.}$	- 0.10"		$\pm$ 0.02"
<b><math>\Delta\Theta</math> (corrected)</b>	6'7.98"	$\pm$ 0.91"	$\pm$ 0.81"
$\Theta_B(\pi\text{H})$	43°14'23.39"	$\pm$ 0.91"	$\pm$ 0.81"
<b>Measured energy [eV]</b>	<b>2885.964</b>	<b><math>\pm</math> 0.014</b>	<b><math>\pm</math> 0.012</b>

Table 5.10: Corrected Bragg angle  $\Theta_B$  of the  $\pi\text{H}_{3p \rightarrow 1s}$  transition at 10 bar measured in 2002 with a Si111 crystal. The result is given as  $value \pm \Delta_{stat} \pm \Delta_{sys}$ .

data from a single measurement, it indicates that the zinc correction method is principally sound. The source of the problem might be a vacuum break immediately before the 2002-2 measurement, which might have had an effect on the spectrometer setup. At the current stage of the analysis, however, this inconsistency remains unresolved.

The corrections to the Bragg angles  $\Theta_B$  of  $\pi\text{H}$  and  $\pi\text{O}$  are the same as for the 2000 beamtime and can be found in Table 4.2. Other systematic corrections, collected in Table 5.10, are also essentially the same as for that setup, but the crystal-detector distance was (2044.5  $\pm$  1.0) mm instead of (2046.3  $\pm$  1.0) mm.



## 5.2.4 Summary of results

The experimental results for the  $\pi\text{H}_{3p\rightarrow 1s}$  transition energy from all three beamtimes are shown in Fig. 5.7 and collected in Table 5.11. One important experimental outcome is that no density dependence could be detected – no extrapolation to density zero is necessary, and the values from all three beamtimes can be averaged for the final result.

It is also remarkable that all results are in good agreement with each other and with the result of the ETHZ-PSI experiment [5], in spite of a different energy calibration method. This strongly indicates that use of a pionic calibration line is a valid method for improving the attainable experimental accuracy.

Two systematic uncertainties that apply equally to all measurements,  $\Delta_{pixel}$  and  $\Delta_{facing}$ , have to be taken into account for the final result. While the nominal size of the CCD pixels is  $40 \times 40 \mu\text{m}^2$  with no error indicated by the manufacturer, an estimate of the actual uncertainty after an optical test measurement is 0.1% [62]. This is reflected in  $\Delta_{pixel}$ , which constitutes a large part of the total systematic error – a forthcoming precision measurement of the pixel size will improve the accuracy of this result considerably.

Measured energy $E_{\text{meas.}} (\pi\text{H}_{3p\rightarrow 1s}) [\text{eV}]$				
Measurement	density	<i>value</i>	$\Delta_{stat}$	$\Delta_{sys}$
2000	3.5 bar	2885.876	$\pm 0.044$	$\pm 0.003$
2001-(1-3)	28.5 bar	2885.919	$\pm 0.012$	$\pm 0.005$
2001-4	liquid hydrogen	2885.924	$\pm 0.024$	$\pm 0.011$
2001-5	3.5 bar	2885.911	$\pm 0.031$	$\pm 0.003$
2002	10 bar	2885.964	$\pm 0.014$	$\pm 0.012$
<b>average <math>E_{\text{meas.}} [\text{eV}]</math></b>		2885.928	$\pm 0.008$	$\pm 0.004$
$\Delta_{pixel}$				$\pm 0.005$
$\Delta_{CCDfacing}$				+0.000 -0.003
<b>Final result <math>E_{\text{meas.}} [\text{eV}]</math></b>		<b>2885.928</b>	<b><math>\pm 0.008</math></b>	<b>+0.006 -0.007</b>
1994 [5]	15 bar	2885.916	$\pm 0.013$	$\pm 0.033$

Table 5.11: Results for the measured energy of the  $\pi\text{H}_{3p\rightarrow 1s}$  transition from the 2000, 2001 and 2002 beamtimes, given as  $value \pm \Delta_{stat} \pm \Delta_{sys}$ . The systematic uncertainties  $\Delta_{facing}$  and  $\Delta_{pixel}$  are applied to the weighted average of all measured values. The result of the ETHZ-PSI collaboration [5] is included for comparison.

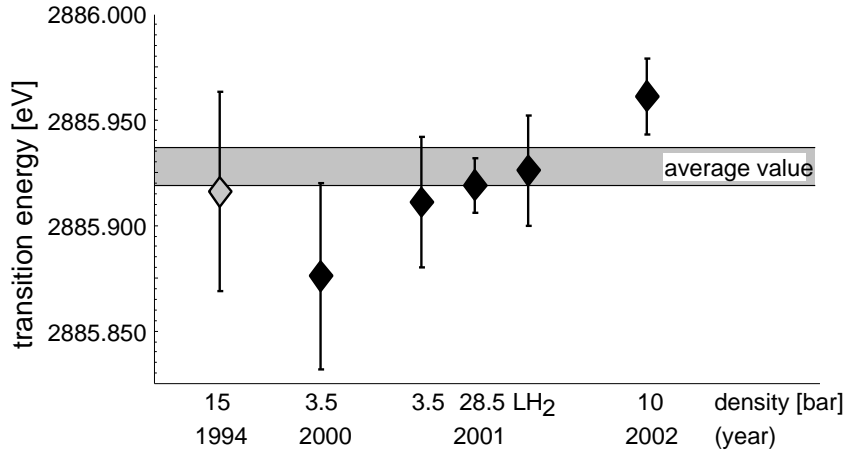


Figure 5.7: Measured energy of the  $\pi H_{3p \rightarrow 1s}$  transition from all three beamtimes (2000, 2001 and 2002) with the weighted average indicated by the horizontal band. The result from Ref. [5] (1994) is included for comparison.

If the CCD array surface is not perpendicular to the crystal-detector distance  $y_{CD}$ , the position distance  $\Delta x$  is increased. The resultant systematic uncertainty  $\Delta_{facing}$  is an asymmetric effect – no matter whether the detector is misaligned to the left or to the right,  $\Delta x$  is always increased. The value of  $\Delta_{facing}$  used here is based on a very generous estimate of  $2^\circ$  maximal misalignment. Again, this uncertainty will be resolved by a precise measurement in the near future.

The experimental value of  $\epsilon_{1s}$  is derived by subtracting the pure QED energy of the  $\pi H_{3p \rightarrow 1s}$  transition  $E_{QED} = 2878.808 \pm 0.006$  meV from the weighted average of all three beamtimes:

$$\epsilon_{1s} = (7.120 \pm 0.008 \begin{smallmatrix} +0.008 \\ -0.009 \end{smallmatrix}) \text{ eV.}$$

### 5.3 Results for $\Gamma_{1s}$

Derivation of the hadronic broadening  $\Gamma_{1s}$  from the data is both easier and harder than for the shift  $\epsilon_{1s}$ . On the one hand, the measured line width is far less sensitive to most of the systematic influences, but on the other hand, there are at least three contributions to this width. The challenge in the analysis lies in disentangling  $\Gamma_{1s}$  from Doppler broadening caused by Coulomb deexcitation and the crystal spectrometer response.

### 5.3.1 Response function

In addition to the width of the  $\pi$ H line itself (caused by hadronic and Doppler broadening), the image reflected to the detector is broadened by the response function of the crystal spectrometer. Mathematically, this is a convolution of the original line profile with the spectrometer response. The influence of the crystal bending process on the well known response function of flat crystals has to be determined with a narrow line of comparable energy. During the first beamtimes, the response function was measured with X-rays from pionic carbon (the  $\pi C_{5g \rightarrow 4f}$  transition).

The investigation of crystal properties with pionic lines is dependent on accelerator beamtimes and hindered by low event rates. For a thorough study of response functions, defocussing and other parameters of the spectrometer, an electron cyclotron resonance ion trap (ECRIT) was installed within the cyclotron trap at PSI [63]. By trapping plasma created by a high-frequency wave in a magnetic bottle field, helium- and hydrogen-like argon atoms have been produced. In such a trap, the ions have very low kinetic energy (a few eV), so Doppler broadening is negligible [64]. This allows the production of narrow X-ray lines with high rates and independent of the accelerator.

The first ECRIT measurements were carried out in 2002, profiling the two crystals that were used in 2000, 2001 and 2002 for the  $\pi$ H experiment (Si 111 and Qu 10 $\bar{1}$ ). For this, the M1 transition  $2^3S_1 \rightarrow 1^1S_0$  in helium-like argon ( $Ar^{16+}$ ) at 3104 eV was used (Fig 5.8), because it is a single line of very small natural width.

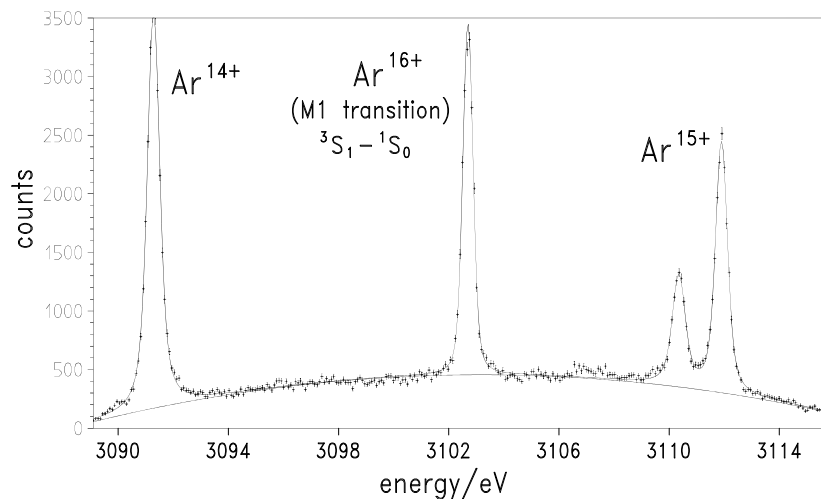


Figure 5.8: Measurement of  $Ar^{14+}$ ,  $Ar^{16+}$  (M1 transition) and  $Ar^{15+}$  from the first trial run of the ECRIT source in 2002.

For the first analysis of the spectra from the ECRIT measurement and all fits to the  $\pi\text{C}$  spectra up to 2002, the response function was characterised as the Gauss portion of a Voigt profile (a convolution of a gaussian and a lorentzian distribution). By optimising the  $\chi^2$  of the numerical fit, a value for the Gauss width was determined which was then kept fixed in the fits of other spectra. This method gave a total response width of  $(545 \pm 31)$  meV for the Si 111 and  $(499 \pm 13)$  meV for the Qu 10 $\bar{1}$  crystal.

With this approach, the experimentally determined widths already show a strong dependence on the measured  $\pi\text{H}_{np \rightarrow 1s}$  transition and a possible hint of density dependence (see Table 5.12 and Fig. 5.9).

To gain a more thorough understanding of the crystal response function, a new approach to the analysis has been taken. An X-ray tracking program for spherically bent crystals with a response function based on the rocking curve of a flat crystal (obtained from the XOP program package [47]) is used to create spectra for different settings of the spectrometer (crystal apertures, focal length, ...). These simulated spectra are compared with the results of the ECRIT measurements at these spectrometer settings.

It was found that all ECRIT spectra could be reproduced very precisely when an additional Gaussian width of about 47 microrad for the Si 111 and 30 microrad for the Qu 10 $\bar{1}$  crystal was incorporated into the simulated spectra (see Fig. 5.10 for examples).

**Coulomb explosion in CH<sub>4</sub>** With the new analysis method, it was also possible to resolve a discrepancy between the FITOS results for the response

**Measured  $\pi\text{H}$  line widths in eV (response width subtracted)**

Measurement	transition	density	<i>value</i>	$\Delta_{stat}$	$\Delta_{sys}$
2000	$\pi\text{H}_{3p \rightarrow 1s}$	3.5 bar	1.039	$\pm 0.085$	$\pm 0.022$
2001-(1-3)	$\pi\text{H}_{3p \rightarrow 1s}$	28.5 bar	1.020	$\pm 0.029$	$\pm 0.022$
2001-4	$\pi\text{H}_{3p \rightarrow 1s}$	liquid hydrogen	1.086	$\pm 0.063$	$\pm 0.022$
2001-5	$\pi\text{H}_{3p \rightarrow 1s}$	3.5 bar	1.039	$\pm 0.085$	$\pm 0.022$
2002-(1-2)	$\pi\text{H}_{3p \rightarrow 1s}$	10 bar	1.053	$\pm 0.027$	$\pm 0.022$
2002-3	$\pi\text{H}_{4p \rightarrow 1s}$	10 bar	0.899	$\pm 0.045$	$\pm 0.010$
2002-4	$\pi\text{H}_{2p \rightarrow 1s}$	10 bar	1.170	$\pm 0.032$	$\pm 0.035$
1994 [5]	$\pi\text{H}_{3p \rightarrow 1s}$	15 bar	0.969	$\pm 0.045$	$\pm 0.010$

Table 5.12: Results for the measured width of  $\pi\text{H}_{np \rightarrow 1s}$  transitions from the 2000, 2001 and 2002 beamtimes after subtraction of the response width. Results are given as  $value \pm \Delta_{stat} \pm \Delta_{sys}$ . The result of the ETHZ-PSI collaboration [5] is included for comparison.

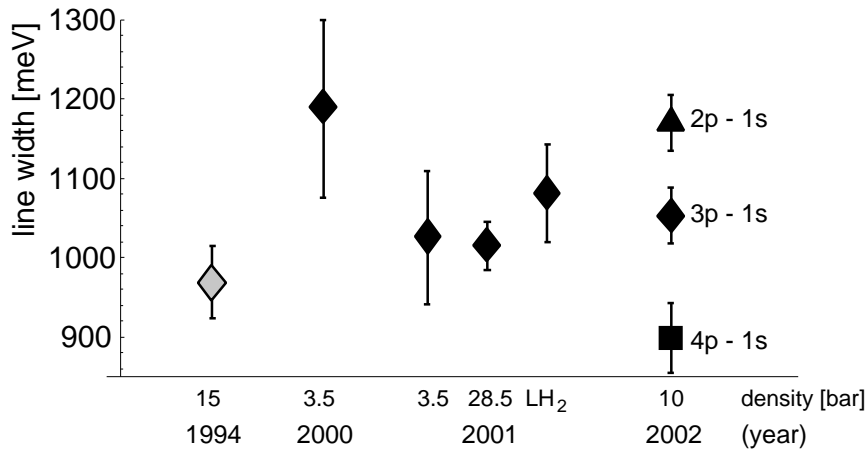


Figure 5.9: Measured line widths after subtraction of the crystal response function, but without a correction for Doppler broadening. The result from Ref. [5] is included for comparison.

function widths measured with the ECRIT and with  $\pi$ C: for both crystals, the fitted line width of the response function was larger with the pionic lines.

The difference can be explained by introducing an additional width from Doppler broadening, which is caused by a cascade process called Coulomb explosion. In this non-collisional cascade process (not to be confused with Coulomb deexcitation) only possible in molecular targets, the fast removal of the binding electrons through Auger deexcitation leads to a strong Coulomb acceleration of the positively charged molecule fragments. Coulomb explosion in exotic atoms was directly observed for the first time from a line broadening in pionic nitrogen [65] – in such diatomic molecules, the gain in kinetic energy can be expected to be especially high.

The  $\pi$ C measurements were conducted with a  $\text{CH}_4$  target gas where no Doppler contribution from Coulomb explosion was expected due to the symmetrical structure of the molecule. However, the additional width of the measured  $\pi$ C spectra compared with the  $\text{Ar}^{16+}$  spectra is in perfect agreement with Doppler broadening from a kinetic energy of 15 eV for the  $\pi$ C atom (Fig. 5.11). This corresponds to a velocity of  $1.5 \cdot 10^6$  cm/s. Earlier measurements of carbon atom fragments after heavy ion impact indicated a lower fragment velocity of  $(0.18 \pm 0.07) \cdot 10^6$  cm/s [66], but higher kinetic energies from the dissociation of the pionic  $\text{CH}_4$  could originate from an asymmetrical explosion: If one or more of the hydrogen atoms would break off before the others, the breakup of the remaining pionic  $\text{CH}_n$  molecule could provide the necessary acceleration.

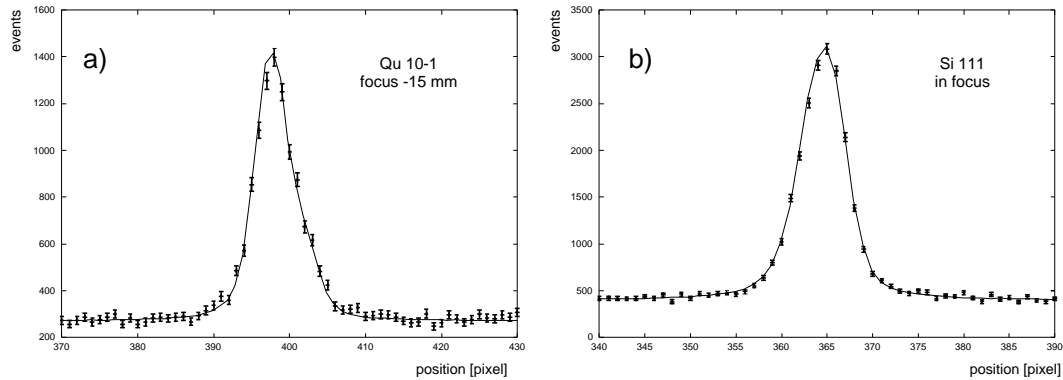


Figure 5.10: Spectra of the 3104 eV line from helium-like argon. **a)** is measured with the Qu 10 $\bar{1}$  crystal and the detector 15 mm out of focus (towards the crystal). **b)** is measured with the Si 111 crystal, a rectangular aperture (width 60 mm) and the detector in focus. The superimposed curve is derived from simulation and reproduces the data in detail.

### 5.3.2 Fit of the $\pi\text{H}_{np\rightarrow 1s}$ line widths

With the crystal response functions derived from the ECRIT measurements, investigation of the Doppler broadening from Coulomb deexcitation has begun. For this task, a convolution of the response function with a line profile based on kinetic energy ( $E_{kin}$ ) distributions at the moment of radiative transition is used to provide the line shape *without* hadronic broadening. The  $E_{kin}$  distributions were calculated with the new cascade code [44], fitted to data from neutron time-of-flight (nTOF) measurements [39]. In these calculations, the cross section for Coulomb deexcitation is scaled with a factor  $k_c$ . The best agreement with the nTOF data is achieved with  $k_c = 0.5$ .

To fit a measured  $\pi\text{H}_{np\rightarrow 1s}$  spectrum, a line shape derived by the method described above is convoluted with a Lorentz width  $\Gamma_L$  – since the crystal response function and the Doppler broadening from Coulomb explosion are already processed into the line shape,  $\Gamma_L$  corresponds to the hadronic broadening  $\Gamma_{1s}$ . For a given  $k_c$ ,  $\Gamma_L$  is varied from 500 meV – 1100 meV in steps of 10 meV and the resultant line is compared to the measured spectrum.

By repeating this process for several values of  $k_c$  and minimising the  $\chi^2$  of the fit, results for  $\Gamma_L$  and  $k_c$  are obtained. If the cascade model behind the  $E_{kin}$  distributions is perfectly correct, this procedure has to result in the same  $\Gamma_L$  and the same  $k_c$  for every  $\pi\text{H}$  transition measured so far. This is not the case; at the current (early) stage of the analysis, values for both the width  $\Gamma_L$  and the cascade factor  $k_c$  diverge strongly for **both** the different  $\pi\text{H}_{np\rightarrow 1s}$  transitions measured in 2002 **and** different target densities measured in 2001.

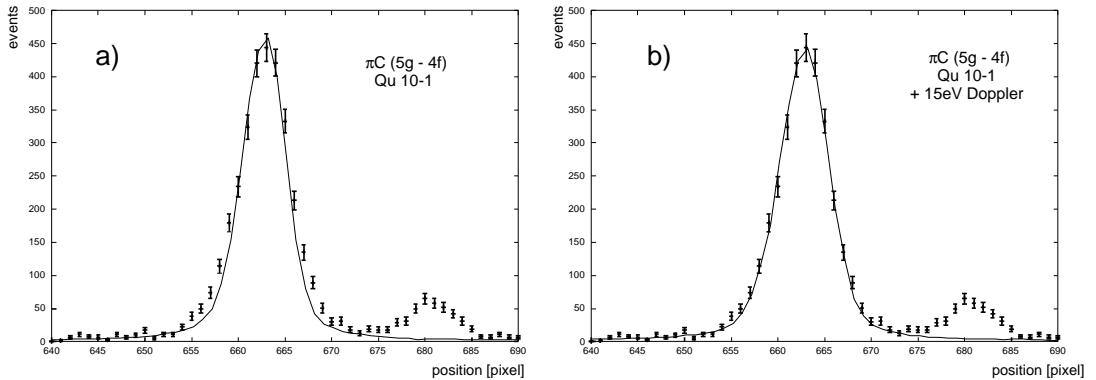


Figure 5.11: Spectra of the  $\pi C_{5g \rightarrow 4f}$  transition measured with the  $Qu 10\bar{1}$  crystal. The superimposed curves are from simulation: In **a)**, just the spectrometer response function derived from the ECRIT measurements is used for the simulation, in **b)** an additional Dopplerbroadening from Coulomb explosion is included.

While it precludes a decisive improvement in the experimental accuracy of  $\Gamma_{1s}$ , this disagreement strongly validates the experimental strategy laid out in Sec. 3.2. The variation of target densities and  $\pi H_{np \rightarrow 1s}$  transitions simultaneously shows the need for further improvement of the cascade models and provides important information towards this end – the  $E_{kin}$  distribution used here originates from nTOF measurements which provide information about the  $ns$  states. The  $np$  states, especially the circular state  $2p$ , have a different cascade history, which obviously results in a quite different distribution of  $E_{kin}$ .

Even so, a constraint on  $\Gamma_{1s}$  from the experiment can be attained at this point: the results from the  $\pi H_{3p \rightarrow 1s}$  and  $\pi H_{4p \rightarrow 1s}$  transitions provide a good estimate on the upper limit of the hadronic width, since Coulomb deexcitations above  $n = 3$  contribute less kinetic energy than the deexcitations into the  $2p$ -state that influence the  $\pi H_{2p \rightarrow 1s}$  transition.

The fit method described above results in a limit of  $\Gamma_{1s} \leq 0.850$  eV. This is in good agreement with the result of the ETHZ-PSI experiment, which gave  $\Gamma_{1s} = (0.868 \pm 0.040 \pm 0.038)$  eV.

## 5.4 Experimental rates

Apart from  $\epsilon_{1s}$  and  $\Gamma_{1s}$ , the relative intensities for different target densities and  $\pi H_{np \rightarrow 1s}$  transitions can also provide data points for the understanding of the  $\pi H$  cascade. To allow a comparison of the results, they have to be corrected for the absorption of X-rays in the target and detector windows and normalised with the collected beam current in Cb (see Table 5.13). As noted in Sec. 4.1.7, however, this normalisation method is not entirely reliable, so these values have rather large uncertainties.

Furthermore, the decreasing rates over time for some of the measurements suggest that residual water in the target chamber vacuum froze over the target window, gradually reducing the number of pionic X-rays that could reach the crystal. These effects would have to be investigated in detail before the rates of the experiment could be compared with results from cascade model calculations.

Data set	Target	Transition	Rate [1/Cb]	$Q_p$ [Cb]	N. events
2000	H <sub>2</sub> /O <sub>2</sub> (1.9%), 3.5 bar	$\pi H_{3p \rightarrow 1s}$	$1.6 \pm 0.1$	438	$688 \pm 34$
		$\pi O_{6h \rightarrow 5g}$	$1.1 \pm 0.2$		$461 \pm 93$
2000-resp.	CH <sub>4</sub> , 1.1 bar	$\pi C_{5g \rightarrow 4f}$	$23.1 \pm 0.6$	64	$1479 \pm 40$
2001-1	H <sub>2</sub> , 28.5 bar He/ <sup>16,18</sup> O <sub>2</sub> (20%), 7.5 bar	$\pi H_{3p \rightarrow 1s}$	$7.3 \pm 0.2$	166	$1218 \pm 39$
		$\pi O_{6h \rightarrow 5g}$	$11.8 \pm 0.4$	223	$2624 \pm 80$
2001-2	H <sub>2</sub> , 28.5 bar He/ <sup>16,18</sup> O <sub>2</sub> (20%), 7.5 bar	$\pi H_{3p \rightarrow 1s}$	$6.9 \pm 1.5$	407	$2820 \pm 59$
		$\pi O_{6h \rightarrow 5g}$	$10.3 \pm 0.3$	211	$2165 \pm 73$
2001-3	H <sub>2</sub> , 28.5 bar He/ <sup>16,18</sup> O <sub>2</sub> (20%), 7.5 bar	$\pi H_{3p \rightarrow 1s}$	$5.9 \pm 0.1$	531	$3152 \pm 63$
		$\pi O_{6h \rightarrow 5g}$	$6.3 \pm 0.2$	342	$2151 \pm 72$
2001-4	H <sub>2</sub> , liquid	$\pi H_{3p \rightarrow 1s}$	$2.9 \pm 0.1$	611	$1770 \pm 50$
2001-5	H <sub>2</sub> /O <sub>2</sub> (1.9%), 3.5 bar	$\pi H_{3p \rightarrow 1s}$	$3.1 \pm 0.1$	348	$1063 \pm 40$
		$\pi O_{6h \rightarrow 5g}$	$2.1 \pm 0.1$		$729 \pm 30$
2001-resp.	CH <sub>4</sub> , 1.5 bar	$\pi C_{5g \rightarrow 4f}$	$13.8 \pm 0.2$	253	$3484 \pm 63$
2002-1	H <sub>2</sub> , 10 bar He/ <sup>16</sup> O <sub>2</sub> (20%), 7.5 bar	$\pi H_{3p \rightarrow 1s}$	$3.6 \pm 0.1$	262	$942 \pm 37$
		$\pi O_{6h \rightarrow 5g}$	$6.5 \pm 0.7$	196	$1273 \pm 136$
2002-2	H <sub>2</sub> , 10 bar He/ <sup>16</sup> O <sub>2</sub> (20%), 7.5 bar	$\pi H_{3p \rightarrow 1s}$	$8.0 \pm 0.1$	914	$7309 \pm 97$
		$\pi O_{6h \rightarrow 5g}$	$13.9 \pm 1.3$	115	$1594 \pm 155$
2002-3	H <sub>2</sub> , 10 bar	$\pi H_{4p \rightarrow 1s}$	$4.9 \pm 0.1$	1478	$7311 \pm 97$
2002-4	H <sub>2</sub> , 10 bar	$\pi H_{2p \rightarrow 1s}$	$9.4 \pm 0.1$	780	$7357 \pm 114$

Table 5.13: Measured event rates of  $\pi H_{np \rightarrow 1s}$  and  $\pi O_{6h \rightarrow 5g}$  transitions for the three beamtimes. The rates are derived by dividing the peak intensity (N. events) by the integrated proton beam current ( $Q_p$ ), which is normally 6 Cb/h. The rates are consistent with the estimate found in Sec. 4.1.7.



# Chapter 6

## Conclusions and outlook

### 6.1 Results

#### 6.1.1 The hadronic shift and width

**Hadronic shift  $\epsilon_{1s}$**  Within the experimental uncertainty, the  $\pi\text{H}_{3p \rightarrow 1s}$  transition energy shows no influence of the target density. This implies that  $(pp\pi)pee$  molecular states, once formed, deexcite through other mechanisms than radiative deexcitation. Energy calibration with pionic X-rays has been shown to work very well.

The averaged result for the hadronic shift from all three beamtimes is

$$\epsilon_{1s} = (7.120 \pm 0.008^{+0.008}_{-0.009}) \text{ eV},$$

given as  $\epsilon_{1s} \pm \Delta_{stat} \pm \Delta_{sys}$ . The systematic error includes the uncertainty of the QED transition energy  $E_{QED}$  of 0.006 eV. The accuracy in the determination of  $\epsilon_{1s}$  is increased by a factor of three compared with the ETHZ-PSI result [5].

The forthcoming measurements of the  $\pi\text{H}$  experiment will further improve the experimental value for  $\epsilon_{1s}$ . Once the mechanical issues of the current spectrometer setup are resolved, the systematic error of measurements with high target density (and correspondingly high event rates) will be decreased noticeably, probably as low as for simultaneous measurements of  $\pi\text{H}$  and  $\pi\text{O}$ . An immediate decrease of the systematic uncertainty will result from a precision measurement of the CCD pixel size and a check whether there is any misalignment of the CCD array towards the crystal-detector axis.

With the new result, the experimental determination of  $\epsilon_{1s}$  has reached a precision comparable to recent calculations of  $E_{QED}$  for the  $\pi\text{H}_{3p \rightarrow 1s}$  transition. There are no fundamental hindrances for a more precise calculation of  $E_{QED}$ , although it would require a significant mathematical effort [61].

**Hadronic width  $\Gamma_{1s}$**  A strong dependence of the measured line widths on the initial state  $np$  in  $\pi\text{H}$  ground state transitions is observed (see Fig. 5.9). This is a clear experimental manifestation of the different contributions from Coulomb deexcitation to the line broadening.

The results of an analysis that takes the Doppler broadening of the line shape from Coulomb deexcitation into account were not consistent for different initial states  $np$  or different target densities. The inconsistency shows that the information on kinetic energy distributions obtained from neutron time-of-flight measurements (Fig. 3.2) cannot be applied directly to the study of radiative transitions.

Therefore, this analysis of the line shapes can only provide an upper limit on the hadronic width:

$$\Gamma_{1s} \leq 0.850 \text{ eV.}$$

This limit was derived from the  $\pi\text{H}_{3p \rightarrow 1s}$  and  $\pi\text{H}_{4p \rightarrow 1s}$  lines because, for these transitions, contributions to the kinetic energy distribution from Coulomb deexcitation are limited. Improvements on existing cascade models are indispensable to permit an increased experimental accuracy for  $\Gamma_{1s}$ .

### 6.1.2 $\pi N$ scattering lengths

From the final result for the hadronic shift  $\epsilon_{1s}$ , the sum  $a^+ + a^-$  of the isoscalar and isovector  $\pi N$  scattering lengths can be calculated by inserting the value for  $\epsilon_{1s}$  into Eq. 2.2. With the correction factor  $\delta_\epsilon = (-7.2 \pm 2.9) \cdot 10^{-2}$  from a next-to-leading order effective field theory calculation [22], this results in

$$a^+ + a^- = (0.0932 \pm 0.0029) m_\pi^{-1}.$$

Due to the large uncertainty of  $\delta_\epsilon$ , the improved accuracy of the experimental result does not lead to a noticeable change of this constraint on the scattering lengths.

The preliminary value for hadronic broadening  $\Gamma_{1s} \leq 850 \text{ eV}$  gives an upper limit on  $a^-$  through Eq. 2.3. Since there is not yet a result for the correction factor  $\delta_\Gamma$  from a calculation within the framework of ChPT, the value from the potential model calculation  $\delta_\Gamma = (-1.3 \pm 0.5) \cdot 10^{-2}$  [21] is used here:

$$a^- \leq 0.0895 m_\pi^{-1}.$$

A plot of these results shows that the constraints from  $\epsilon_{1s}$  and  $\Gamma_{1s}$  in  $\pi\text{H}$  are no longer in agreement with the constraint from  $\epsilon_{1s}$  in  $\pi\text{D}$  (Fig. 6.1). In the light of possible molecular effects and the role of three-body-corrections

in the derivation of the  $\pi N$  scattering lengths from  $\pi D$  experiments, no statement on the strength of isospin breaking can be inferred from this discrepancy without further detailed considerations.

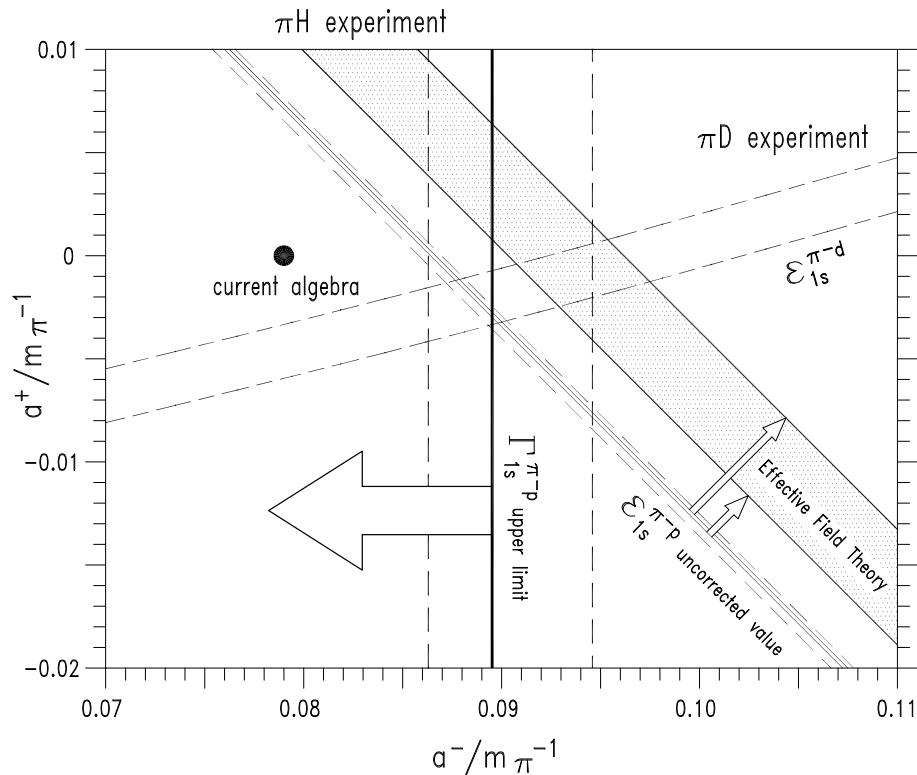


Figure 6.1: Experimental constraints on  $a^+$  and  $a^-$  from the  $\epsilon_{1s}$  and  $\Gamma_{1s}$  results, with the theoretical prediction from current algebra [10] included for orientation. The results from previous  $\pi H$  and  $\pi D$  experiments are indicated by the dashed lines (see Fig. 2.2 for references).

## 6.2 Outlook

The next stages of the  $\pi H$  experiment will concentrate on an improved accuracy for  $\Gamma_{1s}$ . Fig. 6.1 demonstrates that more precise results for the  $\pi N$  scattering lengths from  $\pi H$  data depend on better constraints from  $\Gamma_{1s}$ . Additionally, the determination of the sum  $a^+ + a^-$  from  $\epsilon_{1s}$  cannot be increased in accuracy as long as a more precise value for the low-energy constant  $f_1$  (see Sec. 2.2.3) is unattainable.

To further improve the experimental value for  $\Gamma_{1s}$ , the correction for Coulomb deexcitation has to be more precise. This requires rigorous testing of the  $\pi\text{H}$  cascade models from which kinetic energy distributions at the initial states  $np$  of the measured transitions are derived. The experimental data gathered in 2001 and 2002 provide an excellent basis for these tests.

For a dedicated study of kinetic energy distributions in exotic atoms, measurements with muonic hydrogen ( $\mu\text{H}$ ) are planned. The cascade processes are expected to be very similar (except for nuclear absorption) to  $\pi\text{H}$ . Without hadronic broadening of the ground state and a precisely known spectrometer response function, the effects of Coulomb deexcitation can be investigated in detail. The experimental approach of investigating different target densities and initial transition states  $np$ , which proved to be successful in the  $\pi\text{H}$  measurements, will also be applied to the  $\mu\text{H}$  measurements.

The low production rate for  $\mu\text{H}$  is offset by the absence of loss through nuclear absorption, so the event rates are comparable with the rates for  $\pi\text{H}$ . Theoretical cascade calculations can then be calibrated with the results of the  $\mu\text{H}$  measurement, improving the models these calculations are based upon. This, in turn, will lead to better theoretical predictions for the  $\pi\text{H}$  cascade. With a new understanding of the  $\pi\text{H}$  cascade, an increase of the experimental accuracy for  $\Gamma_{1s}$  to 1% should be attainable.

# Appendix A

## CCD alignment

This appendix details the procedure for determining the rotations and offsets for the individual CCDs in the 3x2 array. A mask with horizontal, vertical and diagonal lines was constructed and used for X-ray measurements. The mask image on the CCD detector array is shown in Fig. A.1.

The relative rotations of the CCDs are determined by performing a linear fit to the mask slits. After the CCDs are rotated by the correct amount, another fit is made to determine the crossing points of the slits at the CCD boundaries. The offsets are calculated by aligning these crossing points with each other.

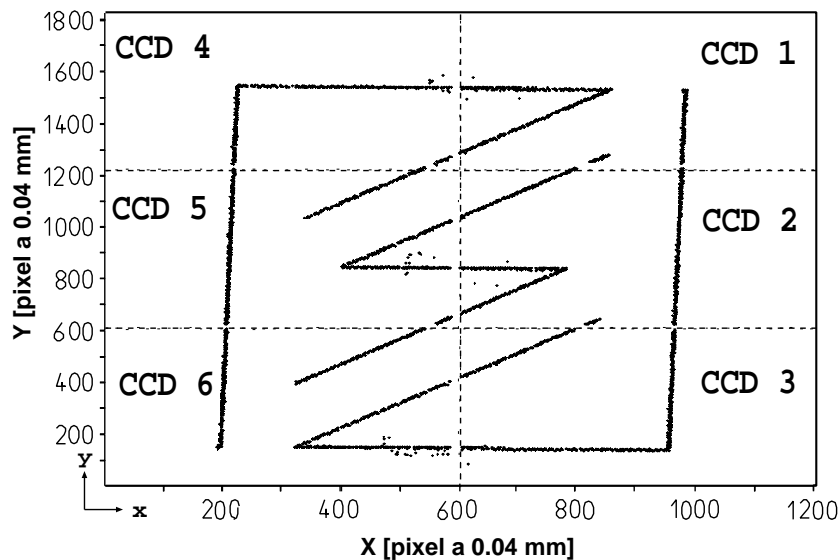


Figure A.1: The 3x2 CCD array with data from the mask measurement. Rotation and translation corrections are already applied.

The mask has a thickness of 1 mm, the slits are wire eroded with a width of 0.1 mm. The detector array, shielded by the mask, is irradiated with X-rays from a sulphur fluorescence target, which produces mainly 2.3 keV X-rays; an energy low enough to keep charge splitting effects small. The target (activated with an X-ray tube) was placed as far away as possible (3.3 m) to reduce distortion of the mask image by parallax effects. A collimator with a diameter of 5 mm was put in front of it to provide a point-like source. In total, about 600 000 events were collected.

**Extraction of individual CCD rotations** A new fitting algorithm within the data processing software performs a linear fit to the images of the mask slits. The fit is done by calculating the center of gravity (COG) for each CCD row (or column for fitting a horizontal line) and then making a linear regression through them. The error of the COGs is based upon a rectangular distribution with a width equal to the width of the slits of the mask. With  $N$  as the number of events and  $w$  as the slit width,  $\Delta_{COG} = \frac{w}{\sqrt{12} \cdot \sqrt{N}}$ . A width  $w$  of 4 pixels for the horizontal/vertical lines and 6 pixels for the diagonals is assumed.

From the inclinations (in mrad) of the mask slits relative to perfect horizontals, verticals or diagonals ( $45^\circ$ ), the rotations of individual CCDs are calculated. Results (relative to CCD 3) are given in Table A.1.

**Calculation of CCD offsets** After the rotations have been determined **and** applied, the lines are fitted again to determine the crossing points of each slit with the CCD edge. The correct values for the vertical offsets follow from the condition that **both** lines have to continue from one CCD to the other. With CCD 3 as the starting point, the only other CCD fulfilling this condition is CCD 6. The position of all other CCDs has to be calculated relative to **all** CCDs shifted so far.

CCD	Rotation [mrad]	x/y-Offset [pixel]
1	0.197(78)	-2.818(22) / 22.264(77)
2	0.522(62)	-1.049(15) / 10.901(85)
3	xxx	0 / 0
4	1.577(84)	-14.347(46) / 20.808(75)
5	2.940(109)	-14.597(43) / 12.265(64)
6	6.382(101)	-16.487(40) / 1.173(52)

Table A.1: CCD position corrections (relative to CCD 3) from the mask measurement. These values were used throughout the analysis of the  $\pi$ H experiment.

The exact derivation goes as follows (Fig. A.2): for case i), one horizontal and one diagonal line,  $A_1 + y + B_1 \cdot x = A_2$  and  $A_3 + y + B_2 \cdot x = A_4$ . From this one derives:

$$x = \frac{(A_2 - A_4) - (A_1 - A_3)}{B_1 - B_2}$$

$$\Delta x = \sqrt{\frac{(\Delta A_1)^2 + (\Delta A_2)^2 + (\Delta A_3)^2 + (\Delta A_4)^2}{(B_1 - B_2)^2} + \frac{((\Delta B_1)^2 + (\Delta B_2)^2) \cdot (A_2 - A_4 - A_1 + A_3)^2}{(B_1 - B_2)^4}}$$

For case ii), one horizontal and one vertical line,  $A_1 + x + B_1 \cdot y = A_2$  and  $A_3 + y + B_2 \cdot x = A_4$  (note that  $B_1$  is defined as  $B_1 \cdot y_i = x_i$ ). Here, the equations are:

$$x = \frac{A_1 - A_2 - B_1(A_3 - A_4)}{B_1 \cdot B_2 - 1}$$

$$(\Delta x)^2 = \frac{(\Delta A_1)^2 + (\Delta A_2)^2 + (\Delta B_1)^2((\Delta A_3)^2 + (\Delta A_4)^2)}{(B_1 \cdot B_2 - 1)^2}$$

$$+ (\Delta B_1)^2 \left( \frac{A_4 - A_3}{B_1 \cdot B_2 - 1} - \frac{B_2(A_1 - A_2 - B_1(A_3 - A_4))}{(B_1 \cdot B_2 - 1)^2} \right)^2$$

$$+ (\Delta B_2)^2 \left( \frac{B_1(A_1 - A_2 - B_1(A_3 - A_4))}{(B_1 \cdot B_2 - 1)^2} \right)^2.$$

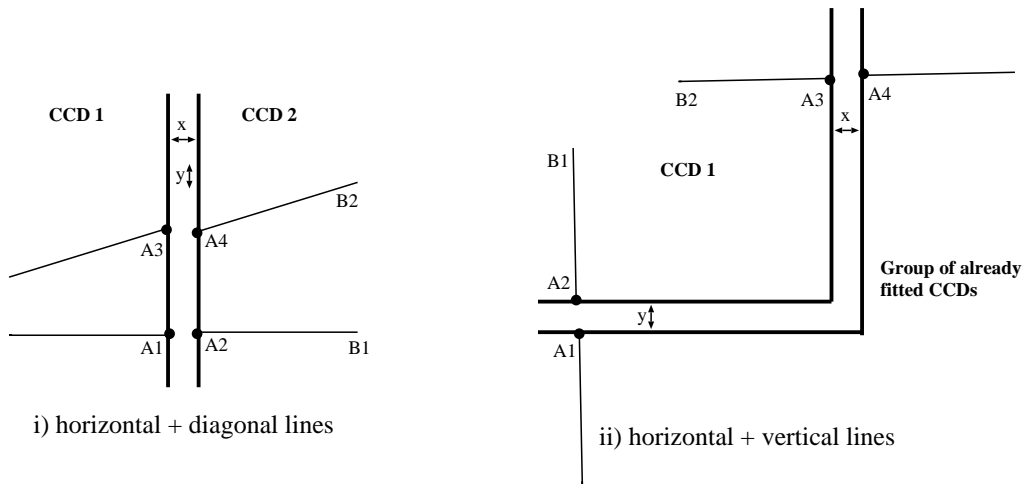


Figure A.2: Definition of the crossing points (see text).

**Results and conclusions** The results for the horizontal and vertical displacements are given in Table A.1. With a pixel size of  $40\ \mu\text{m}$ , the maximal uncertainties are about  $4\ \mu\text{m}$ . This level of precision is already near to what is achievable with optical methods, which would have required dismantling and transporting the detector. A further improvement in accuracy is not limited by statistics, but by the mechanical precision of the mask itself.

The analysis of the mask data assumes that the slits on the mask are perfectly straight - the given uncertainties are purely statistical. However, a detailed study of the vertical slit to the right (on CCDs 1,2 and 3) shows that the mechanical irregularities of the mask are big enough to be noticeable. Fig. A.3 shows the centres of gravity calculated for this slit (subtracted from the fit through these points). Both the sudden jump (left arrow) and the inclination change (right arrow) are substructures on a scale of roughly 1/10th of a pixel ( $4\ \mu\text{m}$ ). This fits well with the mechanical accuracy of  $5\ \mu\text{m}$  that is given for the mask slits.

Two possible methods for improved accuracy would be an optical measurement of the CCD array or a repetition of the procedure outlined here, but with polished edges instead of wire-eroded slits.

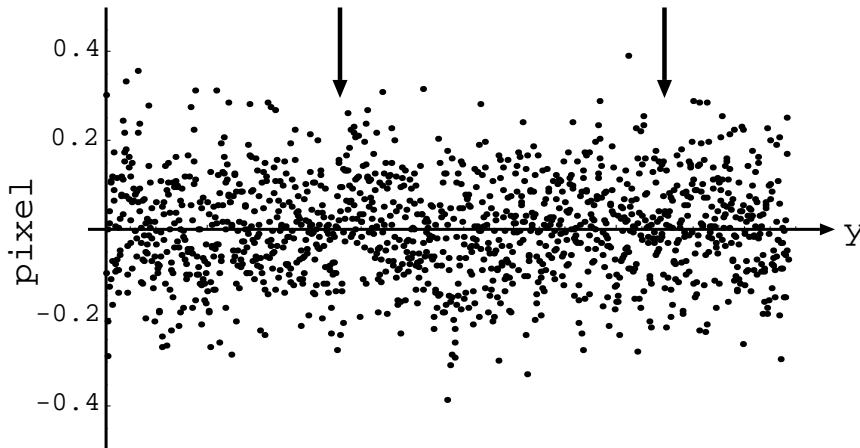


Figure A.3: Centres of gravity of the right vertical mask slit. Arrows indicate the 2 largest irregularities.



# Appendix B

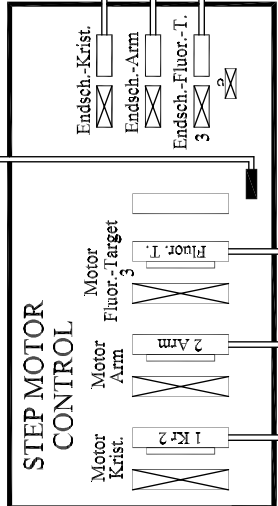
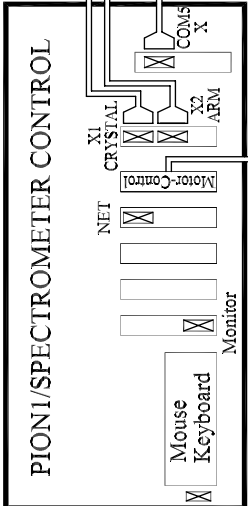
## Plan of the spectrometer wiring

The plan shown on the next side is divided into a section for the control hut **HUT** and a section for the experimental area **AREA**. In the setup during beamtimes at PSI, they are about 25 m apart from each other.

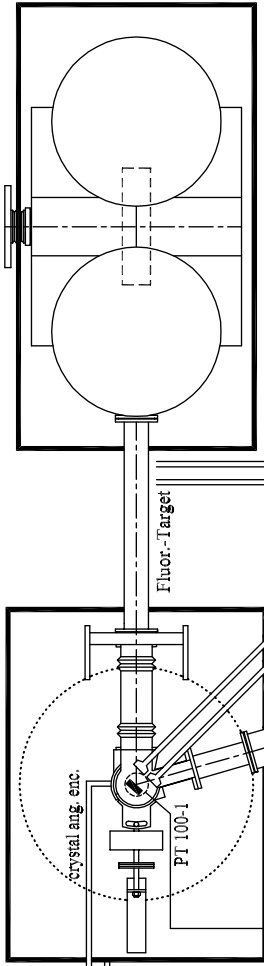
Conceptually, spectrometer control and data transfer are designed with the following aims:

- Permanent control of spectrometer settings during measurements.
- Changes of the spectrometer settings have to be possible without entering the experimental area, since this necessitates at least 10 min interruption of data taking.
- Data transfer should be independent of the PSI network. This is achieved with a local area network not shown in the plan.
- Control of the CCDs (with the **PION 3** PC) has to be completely reliable and possible from both the hut and the area. Since software solutions for control of one PC from multiple terminals tend to be unstable, slow and/or non-intuitive, a direct terminal extension is used.
- Both spectrometer and CCD control must continue to function during power outages. To this end, the power supply for both the **PION 1** PC for spectrometer control and the **PION 3** PC is backed up by a safety battery that can operate them for at least an hour.

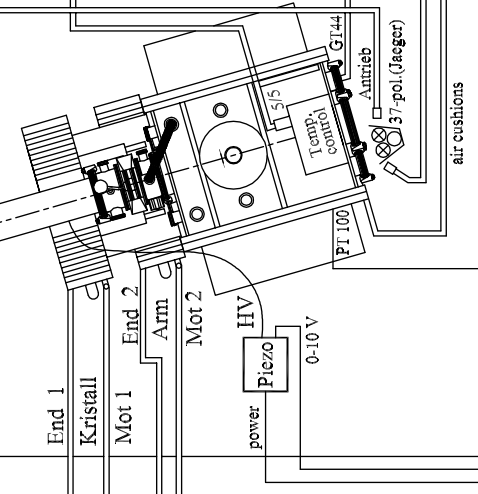
# HUT



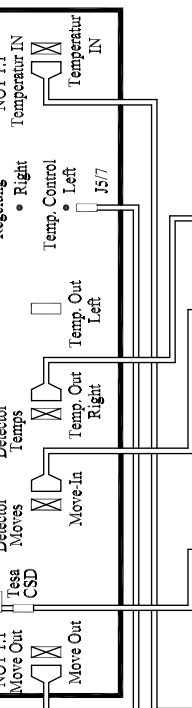
# AREA



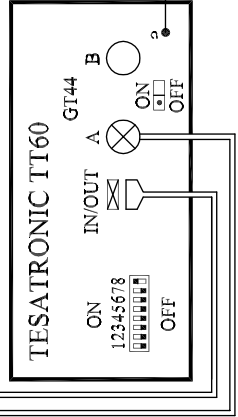
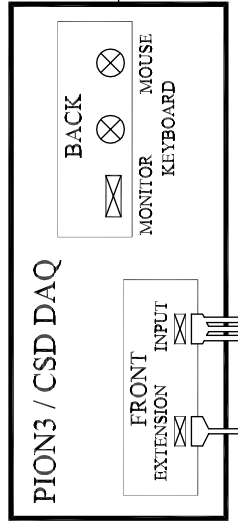
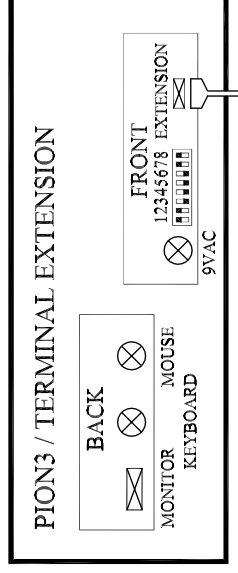
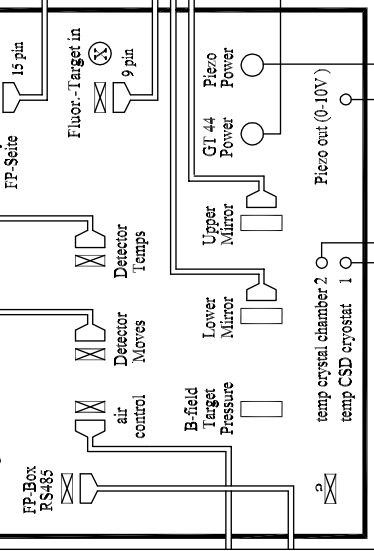
# CRYSTAL SPECTROMETER



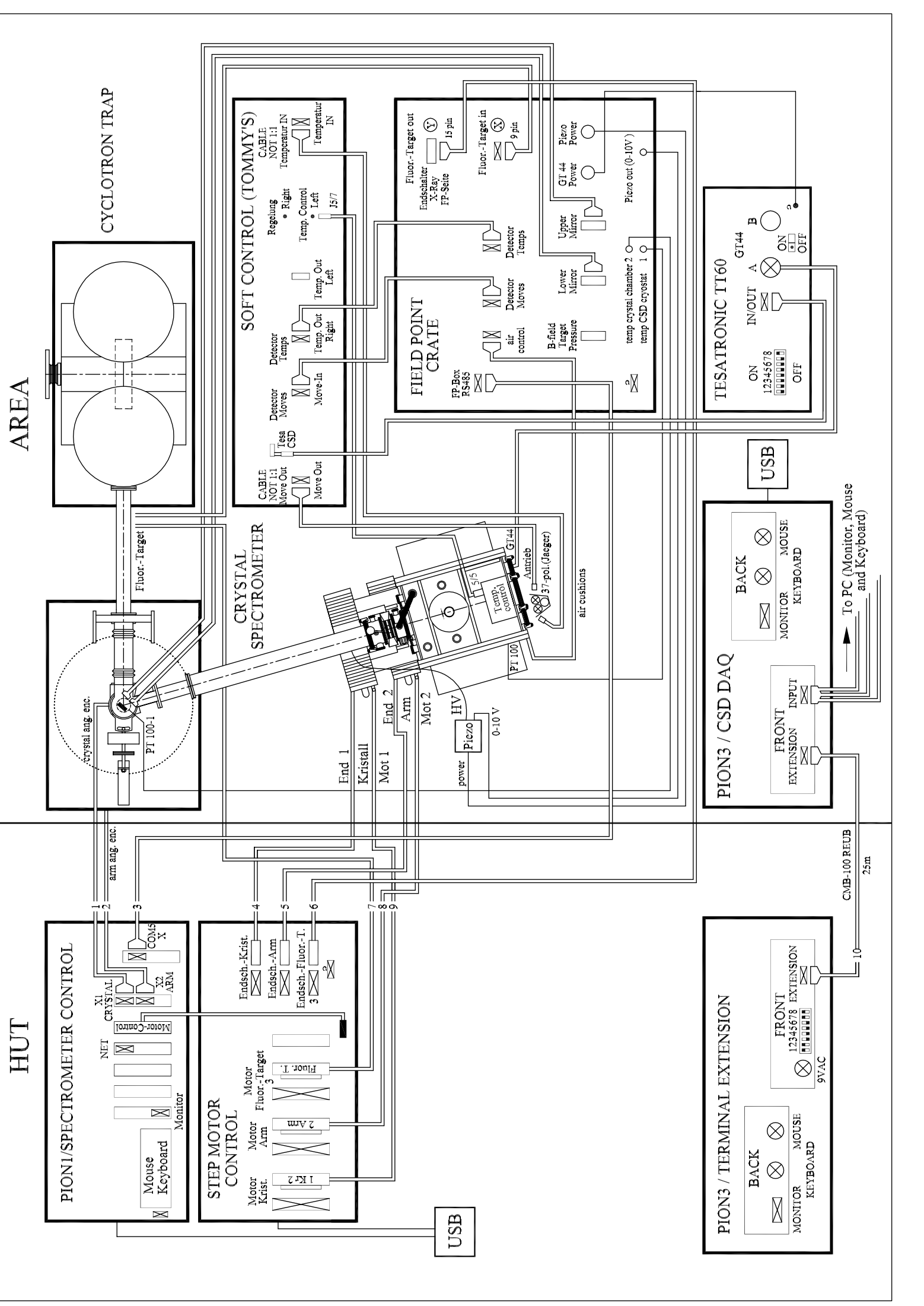
# SOFT CONTROL (TOMMY'S)



# FIELD POINT CRATE



CMB-100 REUB  
25m



# Appendix C

## Run file lists

The lists of data files for the beamtimes in 2000, 2001 and 2002 are collected on the following pages. A short explanation of the headers is given here:

- **date** is the day this run was started.
- **crystal aperture** is the label of the Bragg crystal and the rectangular aperture on it used for this measurement. Vertically, the aperture is limited by a circle ( $\varnothing 95$  mm).
- **target/source** is the target gas or (for fluorescent X-rays) the source.
- **p/mbar** and **T/K** gives the pressure and temperature of the target gas.
- **$Q_p/C$**  is the integrated proton beam current.
- **LEX #/page** indicates where this run is found in the experiment log.
- **file name** – files are numbered sequentially for every beamtime.
- **comment** – notes on spectrometer settings and other information.

## FILELISTPSI2000

## PIONICHYDROGENinitialrun

Z1 3 Si111

Runbook:LEX#7/8

date	crystal aperture	target/source	p /mbar	T /K	$Q_p$ /C	LEX #/page	filename	comment
3.12.	Z13 60	Ar	800	295	---	7/208	argon_0001-0002	focus argon(1995.6mm)=Lin.Tab.67.67
3.12.	Z13 60	CH <sub>4</sub>	1097	295	24.16	7/209	pic_0003-0011	targetscan,focus $\pi$ C(5-4)
3.12.	Z13 60	CH <sub>4</sub>	1498	295	65.75	7/209	pic_0012-0024	$\pi$ C(5-4)atfocus(y <sub>CD</sub> =1985.0mm)Lin.Tab.57.07
4.12.	Z13 60	CH <sub>4</sub>	1498	295	63.84	7/211	pic_0025-0037	$\pi$ C(5-4)atfocus-5mm=Lin.Tab.52.04
5.12.	Z13 60	CH <sub>4</sub>	1498	295	67.49	7/213	pic_0038-0050	$\pi$ C(5-4)atfocus+5mm=Lin.Tab.62.06
5.12.	Z13 60	C <sub>2</sub> H <sub>2</sub>	508	295	47.82	7/214	pic_0051-0059	$\pi$ C(5-4)atfocus-5mm=Lin.Tab.52.07
7.12.	Z13 60	H <sub>2</sub> /O <sub>2</sub> (1.9%)	1350	97.5	24.84	7/217	piOpiH_0061-0066	$\pi$ H(3-1)/ $\pi$ O(6-5)atfocus-5mm=Lin.Tab.116.8 arm36°5' targetscanmixture
7.12.	Z13 60	H <sub>2</sub> /O <sub>2</sub> (1.9%)	1350	97.5	26.88	7/217	piOpiH_0067-0071	arm3 6°15'
8.12.	Z13 60	H <sub>2</sub> /O <sub>2</sub> (1.9%)	1350	97.5	22.95	7/217	piOpiH_0072-0075	arm3 5°55'
8.12.	Z13 60	H <sub>2</sub> /O <sub>2</sub> (1.9%)	1350	97.5	22.68	7/217	piOpiH_0076-0079	arm3 6°25'
8.12.	Z13 60	H <sub>2</sub>	1450	47.5	15.9	7/220	piH_0080-0083	arm36°15' targetscanH <sub>2</sub>
8.12.	Z13 60	H <sub>2</sub>	1450	47.5	16.40	7/220	piH_0084-0086	arm36°34'15''
8.12.	Z13 60	H <sub>2</sub>	1450	47.5	10.82	7/220	piH_0087-0088	arm36°53'
9.12.	Z13 60	H <sub>2</sub>	1450	47.5	13.18	7/220	piH_0089-0091	arm35°56'
8.12.	Z13 60	H <sub>2</sub>	1450	47.5	15.47	7/220	piH_0092-0094	arm36°37'
9.12.	Z13 60	H <sub>2</sub> /O <sub>2</sub> (1.9%)	1430	97.5	31.3	7/224	piOpiH_0095-0106	target scanmixture,attarget8mmvert.slit
10.12.	Z13 60	H <sub>2</sub> /O <sub>2</sub> (1.9%)	1430	97.5	40.35	7/224	piOpiH_0107-0113	arm36°1', $\pi$ Hand $\pi$ Ocenteredinvert.slit
10.12.	Z13 60	He/O <sub>2</sub> (5.5%)	1320	102	105.18	7/225	piO_0114-0132	arm36°1', verticalslit
11.12.	Z13 60	H <sub>2</sub> /O <sub>2</sub> (1.9%)	1310	98.5	173.50	7/227	piOpiH_0133-0161	arm36°1', $\pi$ Hand $\pi$ Ocenteredinvert.slit
12.12.	Z13 60	He/O <sub>2</sub> (5.5%)	1300	102	46.3	7/228	piO_0162-0169	arm36°1', verticalslit
13.12.	Z13 60	Ar	500	285	---	7/229	argon_0170	$\pi$ H(3-1)/ $\pi$ O(6-5)atfocus-5mm=Lin.Tab.116.8
14.12.	Z13 60	H <sub>2</sub>	1490	45	12.11	7/230	piH_0171-0173	36°1' targetscanH <sub>2</sub> novert.slit ↓
14.12.	Z13 60	H <sub>2</sub>	1490	45	12.0	7/230	piH_0174-0175	36°20'
14.12.	Z13 60	H <sub>2</sub>	1490	45	12.25	7/230	piH_0176-0177	36°39'
14.12.	Z13 60	H <sub>2</sub>	1490	45	12.28	7/230	piH_0178-0181	35°42' breakd ownofE-target
16.12.	Z13 60	Ar	100	295	---	7/233	argon_0182-0184	ArK $\alpha$ ,focus"alignmentwithargon
16.12.	Z13 60	Ar	100	295	---	7/233	argon_0185	ArK $\alpha$ ,focus-5mm"
16.12.	Z13 60	Ar	100	295	---	7/233	argon_0186	ArK $\alpha$ ,focus+5mm"
17.12.	Z13 60	Ar	100	295	---	7/233	argon_0187-0190	ArK $\alpha$ ,focus-17mm"K $\alpha$ satelliteint.focus
17.12.	Z13 60	Ar	100	295	---	7/233	argon_0191	ArK $\alpha$ ,focus+15mm"
17.12.	Z13 60	Ar	100	295	---	7/233	argon_0192	ArK $\alpha$ ,focus+35mm"
17.12.	Z13 60	Ar	100	295	---	7/234	argon_0193-0228	ArK $\alpha$ ,focus-5mm" targetscan
18.12.	Z13 60	Ar	100	295	---	7/234	argon_0229	ArK $\alpha$ Positioncheck
18.12.	Z13 60	H <sub>2</sub> /O <sub>2</sub> (1.9%)	1500	98	?	8/2	piOpiH_0230	wrongangles
18.12.	Z13 60	H <sub>2</sub> /O <sub>2</sub> (1.9%)	1500	98	124	8/2	piOpiH_0231-0256	arm36°1' novert.slit

date	crystal aperture	target/source	p /mbar	T /K	$Q_p$ /C	LEX #/page	filename	comment
								<b>set up</b>
9.5.	Z20=30	Ar	52-105	294	---	8/11	argon_0001-0004	focusAr(1872mm),Lin.Tab.67.67,tube30kV/30mA
10.5.	Z20=30	Ar	105	294	---	8/13	argon_0005-0012	targetscan,aperture =30
10.5.	Z20  60	Ar	105	294	---	8/15	argon_0013	targetscanposition460->272?!
10.5.	Z20  60	Ar	105	294	---	8/15	argon_0014-0020	targetscan,aperture  60,positionreadjustedto 485
10.5.	Z20  60	Ar	108	294	---	8/17	argon_0021	afterspectrometerleaktest,Lin.Tab.65.7
10.5.	Z20  60	Ar	108	294	---	8/17	argon_0022-0026	targetscan
10.5.	Z20  60	Ar	110	294	≈1	8/18	argon_0027	ArX-raysexcitedby $\pi$ -beam?(5events)
10.5.	Z20  60	CH <sub>4</sub>	1500	294	29.34	8/18	pic_0028-0035	focus $\pi$ C(5-4)-4.6mm=Lin.Tab.55.7,target,,3cm"
11.5.	Z20  60	CH <sub>4</sub>	1500	294	26.03	8/19	pic_0036-0040	target,,4cm"cry39°7',arm40°30'
11.5.								targetErepair
12.5.	Z20  60	CH <sub>4</sub>	1500	294	9.39	8/21	pic_0041-0043	target,,5cm",AHW41wrongsetting
12.5.	Z20  60	CH <sub>4</sub>	1500	294	18.00	8/21	pic_0044-0047	target,,5cm",AHW41settingcorrect
13.5.	Z20  60	CH <sub>4</sub>	1500	294	15.82	8/22	pic_0048-0050	target,,6cm"
13.5.	Z20  60	CH <sub>4</sub>	1500	294	22.77	8/22	pic_0051-0057	target,,4.5cm",arm40°30'targetscan
13.5.	Z20  60	CH <sub>4</sub>	1500	294	4.82	8/24	pic_0058	arm40°10'
13.5.	Z20  60	CH <sub>4</sub>	1500	294	5.06	8/24	pic_0059	arm40°50'
13.5.	Z20  60	CH <sub>4</sub>	1500	294	57.13	8/24	pic_0060-0074	target,,4cm",arm40°40'focalscan,Lin.Tab50.7
14.5.	Z20  60	CH <sub>4</sub>	1500	294	---	8/24	pic_0075	powerfailurePSI
17.5.	Z20  60	Ar	100	294	---	8/30	argon_0076-0078	targetscan?
17.5.	Z20  60	Ar	100	294	---	8/30	argon_0079-0086	tiltscan
								<b><math>\pi</math>C response function</b>
17.5.	Z20  60	CH <sub>4</sub>	1500	293	80.3	8/31	pic_0087-0101	cry39°7',arm40°20',tilt0.26 focus $\pi$ C(5-4)+0.4mm=Lin.Tab.60.5
18.5.	Z20  60	CH <sub>4</sub>	1500	293	93.58	8/33	pic_0102-0119	focus $\pi$ C(5-4)-9.4mm=Lin.Tab.50.72
19.5.	Z20  60	CH <sub>4</sub>	1500	293	54.35	8/36	pic_0120-0129	focus $\pi$ C(5-4)+5.4mm=Lin.Tab.65.55
20.5.	Z20  60	CH <sub>4</sub>	1500	293	253.05	8/37	pic_0130-0170	focus $\pi$ C(5-4)-4.5mm=Lin.Tab.55.62,resp.function
22.5.	Z20  60	C <sub>2</sub> H <sub>2</sub>	750	294	78.03	8/42	pic_0171-0182	Coul.Expl.
								<b><math>\pi</math>H ( 3 - 1 )</b>
26.5.	Z20  60	H <sub>2</sub>	1500	<119		8/46	piH_0183	cry40°39'30",arm42°32',LinTab.112.3,target,,4cm"
26.5.	Z20  60	H <sub>2</sub>	1500	<103	10.53	8/46	piH_0184-0185	targetscan during cooling down target
26.5.	Z20  60	H <sub>2</sub>	1980	20.3	12.56	8/46	piH_0186-0189	targetscanat30barequiv.density
26.5.	Z20  60	H <sub>2</sub>	1980	20.3	4.80	8/46	piH_0190-0191	targetscan,target,,5.5cm"
26.5.	Z20  60	H <sub>2</sub>	1980	20.3	3.16	8/46	piH_0192	target,,6.5cm"
26.5.	Z20  60	H <sub>2</sub>	1980	20.3	4.80	8/47	piH_0193-0195	targetscan,target,,4cm"continued
26.5.	Z20  60	H <sub>2</sub>	1980	20.3	3.38	8/49	piH_0196	cry40°40'29.9",arm42°22',target,,4cm"
26.5.	Z20  60	H <sub>2</sub>	1980	20.2	166.2	8/49	piH_0197-0224	piHI ,,28bar" cry40°38'30",arm42°22',target,,4cm"
28.5.	Z20  60	He/ <sup>16,18</sup> O <sub>2</sub> (20%)	1980	86.0	223.0	8/54	piO_0225-0261	piOI

FILELISTPSI2001

PIONIC HYDROGEN production per iodI

Z20 quartz10.1

Runbook:LEX#8

<i>date</i>	<i>crystal aperture</i>	<i>target/source</i>	<i>p /mbar</i>	<i>T /K</i>	<i>Q<sub>p</sub> /C</i>	<i>LEX #/page</i>	<i>filename</i>	<i>comment</i>
31.5.	Z20  60	H <sub>2</sub>	1980	20.3	407.26	8/58	piH_0262-0329	piHII „28bar“
4.6.	Z20  60	He/ <sup>16,18</sup> O <sub>2</sub> ( 20%)	1980	80.0	210.97	8/65	piO_0330-0365	piOII
7.6.	Z20  60	H <sub>2</sub>	1980	20.2	530.8	8/70	piH_0366-0450	piHIII „28bar“
11.6.	Z20  60	He/ <sup>16,18</sup> O <sub>2</sub> ( 20%)	1980	85.0	342.2	8/77	piO_0451-0485	piOIII
14.6.	Z20  60	H <sub>2</sub>	1040	17.0	58.31	8/83	piH_0486-0494	piH „liquid“ targetscan
14.6.	Z20  60	H <sub>2</sub>	1040	17.0	610.85	8/86	piH_0495-0600	piHIV „liquid“ arm42°42'
21.6.	Z20  60	H <sub>2</sub> /O <sub>2</sub> ( 1.9%)	1155	85.0	348.39	8/102	piOH_0601-0661	piHV „3.5bar“

date	crystal aperture	target/source	p /mbar	T /K	$Q_p$ /C	LEX #/page	filename	comment
								<b>set up</b>
13.5	Z13  60	Ar	115	294	---	8/226	argon_0080-0081	set-up
13.5	Z13  60	Ar	115	294	---	8/226	argon_0082-0090	cry42°0'0",targetscan,targetcellwithoutBe
13.5.	Z13  60	CH <sub>4</sub>	1520	293	17.82.	8/227	pic_0091-0094	cry41°3'0.2",arm40°33',Lin.Tab.51.12,target,+,4cm "trapheightmeasure2"71.7mm"
14.5.	Z13  60	CH <sub>4</sub>	1520	293	10.13	8/227	pic_0095-0096	target,+,1.5cm"
14.5.	Z13  60	CH <sub>4</sub>	1520	293	18.17	8/227	pic_0097-0099	target,+,3cm"
14.5.	Z13  60	CH <sub>4</sub>	1520	293	12.11	8/229	pic_0100-0101	target,+,3cm",trapheight"69.7mm"
14.5.	Z13  60	CH <sub>4</sub>	1520	293	12.08	8/230	pic_0102-0103	target,+,3cm",trapheight"73.4mm"
14.5.	Z13  60	CH <sub>4</sub>	1520	293	11.57	8/230	pic_0104-0105	target,+,3cm",trapheight"74.1mm"
14.5.	Z13  60	CH <sub>4</sub>	1520	293	12.21	8/230	pic_0106-0107	target,+,4cm",trapheight"74.1mm"
14.5.	Z13  60	CH <sub>4</sub> /(Be)	1520	293	12.06	8/230	pic_0108-0109	target,+,4cm",trapheight"74.1mm",targetwithBe
15.5.	Z13  60	Be/(CH <sub>4</sub> )	1010	294	6.23	8/231	pibe_0110	targ,+,4cm",cry43°28'12",arm36°11',Lin.Tab.51.12
15.5.	Z13  60	Be/(CH <sub>4</sub> )	1010	294	15.54	8/231	pibe_0111-0113	targ,+,4cm",cry43°4'12",arm36°32',Lin.Tab.51.1 2
15.5.	Z13  60	Be/(CH <sub>4</sub> )	1010	294	16.09	8/231	pibe_0114-0116	targ,+,2cm",cry43°4'12",arm36°32',Lin.Tab.51.1 2
13.5	Z13  60	Ar	100	294	---	8/232	argon_0117-0121	targ,+,4cm",cry41°3'0.2",arm40°25',Lin.Tab.51. 21
16.5.	Z13  60	Be/(O <sub>2</sub> )	0(empty)	294	15.99	9/1	pibe_0122-0126	targ,+,3cm",cry43°4'12",Lin.Tab.111.7,targetscan
17.5.	Z13  60	He/Be/ <sup>16</sup> O <sub>2</sub> (20%)	1898	85	43.17	9/3	piO_0127-0133	$\pi$ O/ $\pi$ Besim.,cry43°4'12",arm36°
17.5.	Z13  60	He/Be/ <sup>16</sup> O <sub>2</sub> (20%)	1898	85	99.62	9/3	piO_0135-0167	$\pi$ O/ $\pi$ Besim.,cry43°4'12",arm36°52',Lin.Tab.111.7
19.5.	Z13  60	Zn	---	294	---	9/4	zinc_0168-0170	215frames
								<b><math>\pi</math> H ( 3 - 1 )</b>
19.5.	Z13  60	Be/ H <sub>2</sub>	1133	30.0	15.93	9/5	piH_0171-0175	$\pi$ H/ $\pi$ Besim.,targ,+,4cm",targetscan
19.5.	Z13  60	Be/ H <sub>2</sub>	1133	30.0	25.74	9/5	piH_0176-0179	axialtargetposition,arm36°52'
20.5.	Z13  60	Be/ H <sub>2</sub>	1133	30.0	38.24	9/5	piH_0180-0185	axialtargetpositionandtargetscan
20.5.	Z13  60	Be/ H <sub>2</sub>	1152	30.0	72.63	9/5	piH_0186-0227	tar,+,2.5/+2(fromfile195)cm",cry43°4'12",arm36°52'
22.5.	Z13  60	Zn	---	294	---	9/7	zinc_0228	arm36°52',cal.for $\pi$ H200frames
22.5.	Z13  60	Zn	---	294	---	9/7	zinc_0229	arm36°48',stabilitytest60frames
22.5.	Z13  60	Zn	---	294	---	9/7	zinc_0230	arm36°48',Zntargetrotated5-10°60frames
22.5.	Z13  60	Zn	---	294	---	9/7	zinc_0231	arm36°48',Zntargetrotatedback60frames
22.5.	Z13  60	He/ <sup>16</sup> O <sub>2</sub> (20%)	1810	85	---	9/9	piO_0232-0236	target,+,2.5cm",cry43°4'12", targetscan
23.5.	Z13  60	Zn	---	294	---	9/9	zinc_0237-0239	targetscan
23.5.	Z13  60	He/ <sup>16</sup> O <sub>2</sub> (20%)	1819	85	27.08	9/9	piO_0240-0244	target,+,2.5cm",cry43°4'12",arm37°5'
23.5.	Z13  60	Zn	---	294	---	9/9	zinc_0245	50frames
23.5.	Z13  60	He/ <sup>16</sup> O <sub>2</sub> (20%)	1819	85	30.23	9/9	piO_0246-0251	target,+,3cm",cry43°4'12",arm37°5'
23.5.	Z13  60	He/ <sup>16</sup> O <sub>2</sub> (20%)	1819	85	21.10	9/9	piO_0252-0255	target,+,2.5cm",cry43°4'12",arm37°5'
23.5.	Z13  60	Zn	---	294	---	9/9	zinc_0256-0257	75+20frames
23.5.	Z13  60	He/ <sup>16</sup> O <sub>2</sub> (20%)	1810	85	33.8	9/9	piO_0258-0264	target,+,2.5cm",cry43°4'12",arm37°5'
							interrupt	➔➔➔vacuumfailure ⚡⚡⚡

date	crystal aperture	target/source	p /mbar	T /K	$Q_p$ /C	LEX #/page	filename	comment
24.5.	Z13  60	Zn	---	294	---	9/9	zinc_0265	70frames
							<i>interrupt</i>	<i>changeofsafetybattery</i>
24.5.	Z13  60	Zn	---	294	---	9/9	Zinc_0266	100frames
24.5.	Z13  60	H <sub>2</sub>	1202	30.0	156.6	9/11	piH_0267-0292	target, +2.5cm <sup>2</sup> , cry43°4'12", arm36°52'
25.5.	Z13  60	Zn	---	294	---	9/11	zinc_0293-0294	120+120frames
26.5.	Z13  60	H <sub>2</sub>	1125	30.0	108.5	9/11	piH_0295-0311	
26.5.	Z13  60	Zn	---	294	---	9/13	zinc_0312	100frames
26.5.	Z13  60	H <sub>2</sub>	1133	30.0	87.62	9/13	piH_0313-0328	
27.5.	Z13  60	Zn	---	294	---	9/13	zinc_0329	100frames
27.5.	Z13  60	H <sub>2</sub>	1208	30.0	78.84	9/15	piH_0330-0343	
28.5.	Z13  60	Zn	---	294	---	9/15	zinc_0344-0345	60+60frames
29.5.	Z13  60	Zn	---	294	---	9/15	zinc_0346-0347	60+60frames
30.5.	Z13  60	Zn	---	294	---	9/19	zinc_0348	60frames
30.5.	Z13  60	H <sub>2</sub>	1101	30.0	44.43	9/15	piH_0349-0368	
31.5.	Z13  60	Zn	---	294	---	9/19	zinc_0370-0371	60+60frames
31.5.	Z13  60	H <sub>2</sub>	1209	30.0	102.05	9/21	piH_0372-0393	
1.6.	Z13  60	Zn	---	294	---	9/21	zinc_0394	100frames
1.6.	Z13  60	H <sub>2</sub>	1228	30.0	64.73	9/21	piH_0395-0406	
2.6.	Z13  60	Zn	---	294	---	9/23	zinc_0407	30frames
2.6.	Z13  60	Zn	---	294	---	9/23	zinc_0408	30frames-misalignmentofZntarget(cancelled)
2.6.	Z13  60	H <sub>2</sub>	1227	30.0	127.36	9/23	piH_0409-0430	
3.6.	Z13  60	Zn	---	294	---	9/23	zinc_0431	100frames
3.6.	Z13  60	Zn	---	294	---	9/23	zinc_0432-0433	60+40frames-Zntargetrotatedby1°
3.6.	Z13  60	Zn	---	294	---	9/23	zinc_0434	40+120frames--Zntargetrotatedback
4.6.	Z13  60	H <sub>2</sub>	1242	30.0	83.54	9/25	piH_0435-0447	
4.6.	Z13  60	Zn	---	294	---	9/25	zinc_0448	90frames
4.6.	Z13  60	He/ <sup>16</sup> O <sub>2</sub> (20%)	?	85	115.34	9/25	piO_0449-0467	
5.6.	Z13  60	Zn	---	294	---	9/27	zinc_0468-0469	120+60frames
							$\pi H (4 - 1)$	
5.6.	Z13  60	Ga	---	294	---	9/26	ga_0470-0475	targetscanwitharm
6.6.	Z13  60	Ga	---	294	---	9/26	ga_0476-0481	targetscanwithcrystal
6.6.	Z13  60	Ga	---	294	---	9/28	ga_0482-0484	cry39°46', arm43°13', 5+60+60frames, LinTab=69.79
6.6.	Z13  60	H <sub>2</sub>	1198	30.0	18.10	9/29	piH_0485-0488	cry39°46'12.1", arm43°13', LinTab=69.79
6.6.	Z13  60	H <sub>2</sub>	1198	30.0	9.39	9/29	piH_0489-0490	cry39°31', targetscanwithcrystal
6.6.	Z13  60	H <sub>2</sub>	1216	30.0	697.75	9/29	piH_0491-0600	cry39°46'12.1", arm43°13', LinTab=69.79
12.6.	Z13  60	Ga	---	294	---	9/35	ga_0601-0602	cry39°46'12.1", arm43°13', 60+60fr., LinTab=69.80
12.6.	Z13  60	Ga	---	294	---	9/35	ga_0603-0604	cry39°46'12.1", arm43°13', 60+60fr., LinTab=69.80
13.6.	Z13  60	H <sub>2</sub>	1232	30.0	351.45	9/39	piH_0605-0659	cry39°46'12.1", arm43°13', LinTab=69.79



FILELISTPSI2002

PIONIC HYDROGEN production per

iodII

Z13 Si111

Runbook:LEX#8/9

<i>date</i>	<i>crystal aperture</i>	<i>target/source</i>	<i>p /mbar</i>	<i>T /K</i>	<i>Q<sub>p</sub> /C</i>	<i>LEX #/page</i>	<i>filename</i>	<i>comment</i>
15.6.	Z13 60	Ga	---	294	---	9/41	ga_0660-0661	cry39°46'12.1",arm43°13',60+60fr.,LinTab=69.80
16.6.	Z13 60	H <sub>2</sub>	1232	30.0	337.49	9/43	piH_0662-0715	cry39°46'12.1",arm43°13',LinTab=69.79
								V2operatedtochangesafetyair
18.6.	Z13 60	Ga	---	294	---	9/45	ga_0716-0717	cry39°46'12.1",arm43°13',90+90fr.,LinTab=69.80
18.6.	Z13 60	H <sub>2</sub>	1232	30.0	73.37	9/47	piH_0718-0729	cry39°46'12.1",arm43°13',LinTab=69.79
19.6.	Z13 60	Ga	---	294	---	9/47	ga_0730	cry39°46'12.1",arm43°13',90fr.,LinTab=69.80
21.6.	Z13 60	Ge	---	294	---	9/50	ge_0731-0733	cry53°3',arm52°20'90fr.,LinTab=88.7
								$\pi$ H ( 2 - 1 )
21.6.	Z13 60	H <sub>2</sub>	1272	30.0	21.65	9/51	piH_0734-0740	targetscan,LinTab=123.3
22.6.	Z13 60	H <sub>2</sub>	1280	30.0	209.19	9/51	piH_0741-0776	target+2.5,cry54°,arm51°,LinTab123.31
23.6.		<sup>55</sup> Fe source				9/55	fe_0777	checkforghostpeaks30frames
22.6.	Z13 60	background				9/55	bg_0778	backgroundwithoutbeam120frames
24.6.	Z13 60	H <sub>2</sub>	1291	30.0	2.94	9/53	piH_0779	30frames
24.6.	Z13 60	background				9/53	bg_0780	backgroundwithoutbeam
25.6.	Z13 60	H <sub>2</sub>	1290	30.0	590.55	9/53	piH_0781-0896	
1.7.	Z13 60	Ge	---	294	---	9/62	ge_0897	cry53°3',arm52°20',LinTab123.31
1.7.	Z13 60	Ge	---	294	---	9/62	ge_0898	cry53°3',arm52°20',LinTab88.7

# Bibliography

- [1] S. Deser et al., Phys. Rev. **96** (1954) 774.
- [2] J. Bailey et al., Phys. Lett. **33B** (1970) 369.
- [3] A. Forster et al., Phys. Rev. C **28** (1983) 2374.
- [4] E. Bovet et al., Phys. Lett. **153B** (1985) 231.
- [5] H.-Ch. Schröder et al., Phys. Lett. B **469** (1999) 25.
- [6] J. Gasser and H. Leutwyler, Phys. Rept. **87** (1982) 77.
- [7] B. Adeva et al., proposal CERN/SPSLC 95-1 (1995), CERN experiment PS212 (DIRAC)
- [8] <http://www.lnf.infn.it/esperimenti/dear/>
- [9] N. Fettes, Prog. Part. Nucl. Phys. **44** (2000) 363.
- [10] S. Weinberg, Phys. Rev. Lett. **17** (1966) 616;  
Y. Tomozowa, Nuovo Cim. **46A** (1966) 707.
- [11] M. L. Goldberger, H. Miyazawa, R. Oehme, Phys. Rev. **99** (1955) 986.
- [12] T. E. O. Ericson et al., Physica Scripta **T87** (2000) 71.
- [13] N. Fettes and U.-G. Meißner, Nucl. Phys. A **640** (2000) 311.
- [14] E. Matsinos, Phys. Rev. C **56** (1997) 3014.
- [15] G. Höhler,  $\pi N$  Newsletter **15** (1999) 123.
- [16] N. Fettes, U.-G. Meißner, S. Steininger, Nucl. Phys. A **640** (1998) 199.
- [17] R. Koch, Nucl. Phys. A **448** (1986) 707.
- [18] P. Piirola, E. Pietarinen and M. E. Saonio,  $\pi N$  Newsletter **16** (2002) 121.

- [19] G. Rasche and W. S. Woolcock, NP **A381** (1982) 405.
- [20] J. Spuller et al., Phys. Lett. **67B** (1977) 479.
- [21] D. Sigg et al., Nucl. Phys. A **609** (1996) 269.
- [22] J. Gasser et al., Eur. Phys. J. C **26** (2002) 13.
- [23] V. E. Lyubovitskij and A. Rusetsky, Phys. Lett. **B494** (2000) 9.
- [24] D. Eiras and J. Soto, Phys. Lett. B **419** (2000) 101.
- [25] V. E. Lyubovitskij, private communication.
- [26] A. Rusetsky, private communication.
- [27] S. R. Beane et al., Phys. Rev. C **57** (1998) 424.
- [28] D. Chatellard et al., Nucl. Phys. A **625** (1997) 310.
- [29] P. Hauser et al., Phys. Rev. C **58** (1998) R1869.
- [30] J. Wallenius, private communication.
- [31] V. Bernard, “New Developments in Threshold Pion Photoproduction and Electroproduction” and R. Beck, “Experiments on Threshold Pion Photoproduction  $\gamma p \rightarrow p\pi^0$ ”; both in Chiral Dynamics: Theory and Experiment, Proceedings, Mainz, Germany 1997, edited by A. M. Bernstein, D. Drechsel and T. Walcher, Springer-Verlag, Berlin Heidelberg (1998).
- [32] J. S. Cohen and N. T. Padial, Phys. Rev. A **41** (1990) 3460.
- [33] Proceedings of the Fifth Course of the International School of Physics of Exotic Atoms, edited by L. M. Simons, D. Horváth and G. Torelli, May 14-20, 1989, Erice, Italy, Plenum Press, New York (1990).
- [34] H. A. Bethe and E. E. Salpeter, Handbuch der Physik, **Band XXXV**, Springer-Verlag, Berlin (1957).
- [35] J. H. Doede et al., Phys. Rev. **129** (1963) 2808.
- [36] M. Leon and H. A. Bethe, Phys. Rev. **127** (1962) 636.
- [37] T. B. Day, G. A. Snow and J. Sucher, Phys. Rev. **118** (1960) 864.
- [38] L. Bracci and G. Fiorentini, Nuovo Cim. **43A** (1978) 9.
- [39] M. Daum et al.,  $\pi N$  Newsletter **15** (1999) 262.

- [40] D. Taqqu, in *Muon Catalyzed Fusion*, AIP Conf. Proc. **181** (1989) 217.
- [41] Proc. of the Int. Symposium on Exotic Atoms, Molecules and Muon Catalyzed Fusion (EXAT98), Hyperfine INteractions **118/119** (1999), and references therein.
- [42] R. Pohl et al., Hyperfine Interactions **138** (2001) 35.
- [43] S. Jonsell, J. Wallenius and P. Froelich, Phys. Rev. A **59** (1999) 3440.
- [44] T. S. Jensen, PhD thesis, ETH Zürich (2002).
- [45] L. M. Simons, Physica Scripta **T22** (1988) 90; Hyperfine Interactions **81** (1993) 253.
- [46] A. Gruber, Diploma thesis, IMEP Vienna (2003).
- [47] M. Sanchez del Rio and R. J. Dejus, SPIE proceedings (1998) 3448.
- [48] E. Wagner, Phys. ZS **17** (1916) 407.
- [49] H. H. Johann, Zeitschrift für Physik **69** (1931) 185.
- [50] G. Zschornack , G. Müller and G. Musiol, NIM **200** (1982) 481.
- [51] J. Eggs, K. Ulmer, Zeitschrift für angewandte Physik, 20. Band, 2. Heft (1965) 118.
- [52] F. Cembali et al., J. Appl. Cryst. **25** (1992) 424.
- [53] Firma Carl Zeiss, D-73446 Oberkochen.
- [54] R. Caciuffo et al., Phys. Reports **152(1)** (1987) 1.
- [55] S. Lenz, PhD thesis, University of Cologne (1996).
- [56] D. Gotta et al., Nucl. Phys. A **660** (1999) 283.
- [57] N. Nelms et al., NIM A **484** (2002) 419.
- [58] T. Siems, PhD thesis, University of Cologne (1997).
- [59] G. Basile et al., Phys. Rev. Lett **72** (1994) 3133.
- [60] R. W. G. Wyckoff, Crystal Structures **Vol. 1**, Interscience Publ., New York (1963).
- [61] S. Boucard and P. Indelicato, private communication.

- [62] Nick Nelms, private communication.
- [63] L. Simons et al., Proc. of the 15<sup>th</sup> International Workshop on ECR Ion Sources, ECRIS'02, <http://www.phys.jyu.fi/ecris02>;  
D. F. Anagnostopoulos et al., 11<sup>th</sup> International Conference on the Physics of Highly Charged Ions (HCI02), to be published in NIM B.
- [64] G. Douysset et al., Phys. Rev. E **61** (2000) 3015.
- [65] T. Siems et al., Phys. Rev. Lett. **84** (2000) 4573.
- [66] R. Mann et al., J. Phys. B **11** (1978) 3045.

# Vielen Dank an...

Meinen Doktorvater Prof. Dr. H. Ströher für die Ermöglichung dieser Doktorarbeit am Forschungszentrum Jülich.

Prof. Dr. H. Paetz genannt Schieck für die Übernahme des Korreferats.

Prof. Dr. E. Müller-Hartmann für die Übernahme des Prüfungsvorsitzes.

Meinen Betreuer Dr. D. Gotta für drei schnell verflogene Jahre, in denen ich dank seiner Fähigkeiten sehr viel gelernt und die dank seines Charakters auch bei harten Prüfungen durch die experimentiellen Unwägbarkeiten schlicht und einfach schön waren.

Dr. L. Simons für gern in Anspruch genommene Gastlichkeit im Südschwarzwald, Teilhabe an seinem Erfahrungsschatz und aufopferungsvollen Dienst an der Apparatur.

Herrn P. Wieder für unentbehrliche Hilfe bei Erstellung der Zeichnungen.

Alle anderen Mitarbeiter des IKP II für das hervorragende Arbeitsklima. Ein spezieller Dank an Dr. V. Kleber für wertvolle Korrekturen in letzter Minute.

All other members of the  $\pi$ H collaboration – Thanks for the fruitful discussions during the days and nights of beamtime!

# Erklärung

Ich versichere, dass ich die von mir vorgelegte Dissertation selbstständig angefertigt, die benutzten Quellen und Hilfsmittel vollständig angegeben und die Stellen der Arbeit - einschließlich Tabellen, Karten und Abbildungen - die anderen Werken im Wortlaut oder dem Sinn nach entnommen sind, in jedem Einzelfall als Entlehnung kenntlich gemacht habe; dass diese Dissertation noch keiner anderen Fakultät oder Universität zur Prüfung vorgelegen hat; dass sie - abgesehen von unten angegebenen Teilpublikationen - noch nicht veröffentlicht worden ist sowie, dass ich eine solche Veröffentlichung vor Abschluss des Promotionsverfahrens nicht vornehmen werde. Die Bestimmungen dieser Promotionsordnung sind mir bekannt. Die von mir vorgelegte Dissertation ist von Herrn Prof. Dr. H. Ströher betreut worden.

## Konferenzbeiträge

- HADRON'01, 14<sup>th</sup> Summer School, "Understanding the Structure of Hadrons", Prague, July 9-13, 2001, Czech. J. Phys. **52** (2002) B169
- International School of Nuclear Physics, 24<sup>th</sup> Course, September 2002, Erice, Sicily, Italy, im Druck





# Lebenslauf

## *Persönliche Daten:*

Name: Maik Christian Hennebach  
Wohnort: Brunkensteinstr. 9, 50935 Köln  
Geburtsdatum: 18. September 1972  
Geburtsort: Hamburg  
Familienstand: ledig

## *Schulausbildung:*

1979 - 1983 Grundschule Konradstrasse in Gelsenkirchen-Buer  
1983 - 1986 Max-Planck-Gymnasium in Gelsenkirchen-Buer  
1986 - 1992 Marienschule (Gymnasium) in Leverkusen-Opladen  
1992 Abitur

## *Zivildienst:*

1992 - 1993 Individuelle Betreuung von  
Schwerstbehinderten beim DRK Köln.

## *Studium:*

1993 - 2000 Studium der Physik an der Universität zu Köln  
1998 - 1999 Diplomarbeit am FZ Jülich, Institut für Kernphysik  
Titel: „Untersuchungen zum Einsatz von  
Čerenkovzählern mit Totalreflektion  
für die Teilchenidentifikation an ANKE “  
Januar 2000 Abschluss des Diploms  
März 2000 Beginn der Doktorarbeit am FZ Jülich,  
Institut für Kernphysik mit dem Ziel der  
Promotion an der Universität zu Köln